**UNIVERSITÀ DEGLI STUDI DI MILANO-BICOCCA**

**DIPARTIMENTO DI SCIENZE DELLA'AMBIENTE E DELLA TERRA**

**SCUOLA DI DOTTORATO**

Ph.D. in Chemical, Geological and Environmental Sciences

Curriculum in Chemical Sciences, XXXIV Cycle

# Theoretical study of semiconductor heterojunctions for photo-and electro-catalysis

**Luis Antonio CIPRIANO MARCOS**

**No. 848320**

Supervisor: **Prof. Sergio Tosoni**

Co-supervisor: **Prof. Gianfranco Pacchioni**

Coordinator: **Prof. Davide Ballabio**

A.A 2021/2022

*Existe un sinfín de diferentes átomos en la naturaleza, decía Demócrito. Algunos son redondos y lisos, otros son irregulares y torcidos. Precisamente por tener formas diferentes, podían usarse para componer diferentes cuerpos. Pero aunque sean muchísimos y muy diferentes entre sí, son todos eternos, inalterables e indivisibles pues la palabra «átomo» significa «indivisible».*

*Demócrito, artículo 5.*

## Abstract

The present thesis is focused on the computational treatment of transition metal oxides and classical semiconductors. The interest in these materials is due to their electronic, optical, and magnetic properties, and their wide range of applications in catalysis, electronic devices, and photo-and electro-catalysis. One of the fundamental properties of these materials is the band gap, which determines the optical, electrical, and chemical properties. From a theoretical perspective, the most widely employed methodology to describe the band gap of these materials is the Density Functional Theory (DFT). The estimation of the band gap by DFT with the GGA approach or hybrid functionals is justified for materials that are not highly correlated such as $TiO_2$, ZnO, $V_2O_5$, III-V semiconductors, etc. However, when one deals with highly correlated materials, it is necessary to introduce methods that include many-body effects (electron hopping), such as the GW, and the dynamical mean-field theory (DMFT).

In order to solve the problem of the description of highly correlated materials, we started this thesis with the study of transition metal oxides with Mott Hubbard character by using the Charge Transition Level approach (CTLs). From this research, it was found that CTLs approach provides a better description of the band gap of highly correlated materials than those obtained with hybrid functionals and high level of theory methods such as GW and DMFT, where the computed values are compared with experimental measurements. Next, the description and rationalization of the role of quantum confinement on III-V semiconductors through the consideration of (110) surfaces with different thicknesses was studied. The results from quantum confinement indicate that there are two groups of semiconductors, the first one corresponds to semiconductors that are less affected such as the Al-V group, and the second one to semiconductors that are strongly affected such as the In-V group.

Then we moved to the computational treatment of composite materials for photocatalytic applications such as the heterojunctions. In a dedicated chapter, some methodological aspects that need to be considered in the design of binary and ternary heterojunctions were provided. In particular, the description of type-II heterojunctions is given since these kinds of interfaces are the most interesting for photocatalysis applications.

In this last chapter of the thesis two cases of co-catalysts are described, both based on single atoms catalysts (SACs) for the hydrogen evolution reaction (HER). First, the effect of different gold nanoparticles size (Single atoms, Nanoclusters, and Nanoparticles) supported on nitrogen-doped graphene is discussed. Second, the formation of two intermediates (MH and HMH) in transition metal oxides adsorbed on different nitrogen-doped graphene supports and molybdenum disulfide ($MoS_2$) is described.



## Keywords

Photocatalysis, correlated materials, CTL approach, heterojunctions, single atom catalyst, hydrogen evolution reaction, hybrid functionals, density functional theory

# Acknowledgments

Foremost I would like to thank to my supervisor Prof. Sergio Tosoni for his valuable time, tolerance and guidance. I also would like to thank Prof. Gianfranco Pacchioni, he has been an extraordinary mentor and his passion for research always inspiring me. Both of them always given me support in everything and I learned too much from them.

I would like to thank Prof. Lorenzo Maschio and Prof. Giuseppe Mallia for their valuable time to review this thesis. I also want to thank Prof. Stefan T. Browley for his valuable time to be part of the members for the assessment committee.

To Dr. Giovanni Di Liberto for his valuable time and guidance during my Ph.D. It was interesting work with him because I learned many things.

To my colleagues for the great time that we spent together in Italy (Bicocca, traveling around, funny talks, etc.): Dr. F. Maleki, Dr. T. Das, and Dr. H.V. Thang.

To the University of Milano-Bicocca for the financial support during my Ph.D.

Furthermore, I would like to thank my family, especialmente a mi padre y madre, CCA y CML, por su invaluable motivación y soporte - CCM y VCM a ustedes también -. At last, I thank to my dear uncle (†) and friends in Mexico and Italy for their invaluable motivation and the time that we spent together.

**Contents**


Chapter I: Introduction ..... 1

1.1 Catalysis and photocatalysis ..... 1

1.2 Heterojunctions ..... 2

1.2.1 Methodological aspects to be consider in the design of heterojunctions with DFT ..... 4

1.2.1.1 The band gap problem ..... 4

1.2.1.2 Band offsets ..... 5

1.3 Co-catalyst ..... 6

Chapter II: Methodological aspects ..... 7

2.1 Theoretical description of oxide semiconductors ..... 7

2.2 Dielectric-dependent hybrid functionals ..... 9

2.3 Charge transition levels ..... 10

2.4 Used codes ..... 13

Chapter III: Fundamental material properties ..... 14

3.1 Band gap description of magnetic insulators from a charge transition levels approach ..... 15

3.1.1 Introduction ..... 15

3.1.2 Computational details ..... 16

3.1.2.1 Basis sets, supercells, tolerances ..... 17

3.1.3 Results ..... 19

3.1.3.1 Test case of the CTL approach: $Cu_2O$ ..... 19

3.3.3.2 MnO ..... 21

3.3.3.3 FeO ..... 23

3.3.3.4 CoO ..... 24

3.3.3.5 NiO ..... 26

3.3.3.6 CuO ..... 28

3.1.4 Discussion and summary ..... 30

3.2 Role of quantum confinement in group III-V semiconductor 2D nanostructures ..... 33

3.2.1 Introduction ..... 33

3.2.2 Computational details ..... 35

3.2.3 Results..... 36

3.2.3.1 Bulk..... 36

3.2.3.2 Surface..... 39

3.2.4 Summary..... 44

Chapter IV: Heterojunctions..... 46

4.1 An example of type-II heterojunction: Structure and band alignment of InP photocatalysts passivated by $TiO_2$ thin films..... 47

4.1.1 Introduction..... 47

4.1.2 Computational details..... 49

4.1.3 Nature of different InP and $TiO_2$ surfaces..... 49

4.1.4 Nature of different InP/$TiO_2$ heterojunction models..... 50

4.1.5 Charge transfer and band alignment..... 52

4.1.6 Effect of the $TiO_2$ film thickness in the InP/$TiO_2$ interface..... 54

4.1.7 kinetics effects..... 56

4.1.8 Summary..... 58

4.2 Rational design of binary and ternary semiconductor heterojunctions for photocatalysis..... 59

4.2.1 Introduction..... 59

4.2.2 Computational details..... 60

4.2.3 Examples of Heterojunctions..... 60

4.2.3.1 Type-II heterojunctions: joining different semiconductors..... 60

4.2.3.1.1 $TiO_2$/$CsPbX_3$..... 60

4.2.3.1.2 $TiO_2$/$BiVO_4$..... 62

4.2.3.1.3 $TiO_2$/$SrTiO_3$..... 63

4.2.3.1.4 $WO_3$/$BiVO_4$..... 64

4.2.3.2 Type-II heterojunctions: joining different facets of the same semiconductor..... 65

4.2.3.2.1 $BiOIO_3$(010)/$BiOIO_3$(100)..... 65

4.2.3.2.2 $TiO_2$(001)/$TiO_2$(101)..... 66

4.2.3.3 Ternary heterojunctions..... 68

4.2.3.3.1 $TiO_2$/$TiO_2$/ZnS..... 68

4.2.3.3.2 $C_3N_4$/$SrTiO_3$/$TiO_2$..... 69

4.2.4 Summary....72
Chapter V: Co-Catalyst....73
5.1 Gold nanoclusters supported on nitrogen-doped graphene as a photocatalyst for hydrogen conversion....74
5.1.1 Introduction....74
5.1.2 Computational details....75
5.1.3 Results and discussion....76
5.1.3.1 Photoelectrocatalytic HER mechanism....76
5.1.3.2 DFT modeling of the HER activity....77
5.1.3.2.1 Characterization of the catalysts....78
5.1.3.2.2 HER activity of the catalyst....81
5.1.4 Summary....85
5.2 Single atom catalysts for hydrogen evolution reaction: the role of dihydride or dihydrogen complexes....86
5.2.1 Introduction....86
5.2.2 Computational details....89
5.2.3 Modelling of HER on metal surfaces....89
5.2.4 Modelling of HER on single atom catalysts (SAC)....92
5.2.4.1 Experimental benchmark....94
5.2.4.2 Formation of two-hydrogen complexes on SACs....98
5.2.4.3 Comparison of kinetics based on one or two intermediates....102
5.2.4.4 Beyond Nørskov' model....104
5.2.5 Summary....106
Conclusions....107
References....110
List of Publications....127

# Chapter I: Introduction

## 1.1 Catalysis and photocatalysis

In the last decades, one of the most important aspects considered by scientists around the globe is the development of new materials with specific chemical-physical properties that can cover the environmental requirements of our time. The development and improvement of new materials paves the way of many sub-areas of materials science, chemistry, physics and engineering to discover and create new opportunities for Scientists and PhD students who want to introduce new ideas, concepts, and theories about the different kind of materials that can be use and are friendly with our planet. The catalysis and photocatalysis are clear examples of sub-areas of materials science and chemistry that can help to do this. The goal in materials science and chemistry is the development of new materials that make them more efficient in the processes where they are applying.[1]

The energy demand and all the comforts that the society is enjoying seems to be one of the main sources of pollution. This issue is mainly regarded to the way in which many countries around the globe are generating energy: through the use of petroleum derivatives.[2] One of the alternatives to solve this issue are the so-called green energies (e.g. solar, eolic, geothermic, etc), and with that the development of new materials that can help to take benefits of these natural sources. The development and design of new materials can also help to improve the power generation processes and another actual issues, as is the power storage capacity.[1]

In the daily activities many processes depend on chemical reactions and the use of catalytic materials make these processes easier, an example is the food production by the use of fertilizers. An essential compound in the synthesis of fertilizers is ammonia which usually is produced by a metal catalyst in the Haber-Bosch process.[3] Another example is the conversion of toxic gases and pollutants generated from the internal combustion engine into less-toxic pollutants by a catalytic converter.[4]

Since the discovery of $TiO_2$ electrode for the water splitting process by Fujishima and Honda,[5] nowadays it is well know that the photocatalytic activity of semiconductors

for photocatalysis applications mainly depend on three steps: i) light absorption;ii) separation and migration of the photogenerated species (electrons and holes); iii) redox reactions on the surface, see Figure 1.

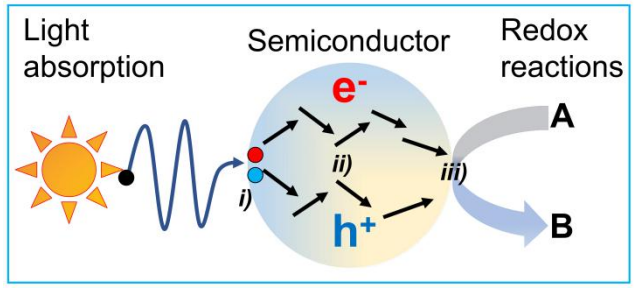


**Figure 1.** schematic representation of the photocatalytic activity on semiconductors. i) light absorption;ii) separation and migration of the photogenerated species (electrons and holes); iii) redox reactions on the surface.

In catalysis and photocatalysis some of the existing semiconductors do not absorb light in the visible range, in this respect narrow band gap materials are desired. A variety of investigations have been done with the goal of increase the photocatalytic efficiency on semiconductors and 2D materials taken in consideration the sequential steps mentioned above.[6] However, the generation of the electron-hole pair implies also their recombination process. To address the recombination process of the photogenerated species in semiconductor and with that increase the photoactivity a variety of strategies have been used, some of them are: via doping, nanostructuring (co-catalyst), formation of a semiconductor/metal oxide heterojunction, or a combination of these approaches.[1,7,8] Of course, all of them taken in consideration the next requirements; (1) a good visible light absorption, (2) a favorable position of the edges of the valence and conduction bands with respect to target redox species, (3) an efficient charge carriers separation upon excitation, (4) a high mobility and low recombination rate of the charge carriers, and last but not least (5) a good chemical stability.[7–9]

### 1.2 Heterojunctions

A clear example of materials that can improve the chemical-physical properties of new materials in catalysis and photocatalysis are heterojunctions, which are composite materials where two or more units are in contact due to the formation of a junction region. Considering the Anderson diffusion model for semiconductor materials, one can identify three types of heterojunctions depending on the alignment of the valence band (VB) and conduction band (CB) edges of the interface,[10] in Figure 2 is shown a scheme of the three types of heterojunctions:

a) straddling gap (Type-I)

It is formed by the union of two semiconductors with very different energy gaps and is characterized in that the conduction band of component B is above that of component A. The valence band of component B is below component A (the bands of component A are among those of component B, Figure 2(a). The holes and electrons are transferred and accumulated in the component of smaller energy gap.

b) staggered gap (Type-II)

It is formed by the union of two semiconductors with a very similar energy gap and is characterized in that the photo-excited electrons are transferred from the conduction band of component A to the conduction band of component B. While the holes can travel in the direction opposite to the electrons, that is, from the valence band of component B to the valence band of component A. This type of interface allows to reduce the energy gap, to generate an efficient separation of the charge (to decrease the recombination rate) and improve the catalytic activity in materials, Figure 2(b). This type of heterojunction is common when you have p and n semiconductors.

c) broken gap (Type-III)

It is formed by two semiconductors with a similar or very different energy gap and is characterized by generating a high conduction charge transfer. The valence band of component B is above the conduction band of component A, Figure 2(c).

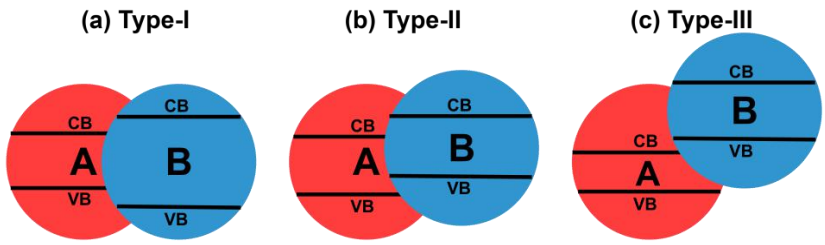


**Figure 2.** Heterojunctions types. (a) type I, straddling gap; (b) type II, staggered gap; (c) type III, broken gap.

In the last decades, heterojunctions have been studied extensively and advances in synthesis methods to form them have been demonstrated. However, still many questions about what its happening at the atomistic scale exist, in this way, computational approaches are well suited to investigate the functioning of heterojunctions and with that provide valuable atomistic insights.

An accurate and efficient method used to describe materials at atomistic scale is density functional theory (DFT).[9,11]

### 1.2.1 Methodological aspects to be consider in the design of heterojunctions with DFT

To address semiconductor heterojunctions with DFT calculations one has to deal with various methodological issues. Some of them are of very general nature, such as *i)* the problem of the determination of the band gap within the DFT formalism,[12] and *ii)* the necessity of properly aligning energy levels of the involved species in the interface with respect to target redox species. Other methodological problems are intrinsically related to the creation of the interface, and involve the role of surface termination, the problem of strain that can result by the use of the same supercell to describe two materials with different lattice constants, etc.[13] Sometimes the role of quantum confinement when nanostructured materials are considered needs to be addressed.[14]

#### 1.2.1.1 The band gap problem

The problem of describing the Kohn-Sham (KS) band gap in semiconductor materials has been widely discussed in the past. There is general consensus that hybrid functionals, where a portion of exact exchange is added to the DFT exchange functional, offer a better description of this important property.[15–18] However, several kinds of hybrid functionals have been proposed over the years. They usually differ by the choice of the GGA functional[19] approximating the semi-local part, and by the amount of exact exchange added to the DFT functional. Usually this is fixed and is not material dependent. An alternative to the hybrid functionals is represented by the dielectric-dependent (DD) functionals where the amount of exact exchange is obtained self-consistently from the dielectric constant of the material.[20–22] However, in a recent study, Tilak Das and coworkers compared the performances of various popular hybrid functionals, including standard (PBE0, B3LYP, HSE06, etc.) and dielectric-dependent (DD) functionals.[17] The conclusion is that there is no general improvement in the use of DD functionals compared to PBE0, HSE06 and B3LYP, although some systems are better described at the DD level. Thus, standard hybrid functionals as PBE0 or HSE06 are recommended for non-magnetic bulk 3D metal oxides, while layered materials benefits from the use of DD, range-separated functionals.

Another specific problem related to the study of heterojunctions where two or more materials are interfaced, is that a single functional must be used for the whole system, thus limiting the use of material dependent functionals such as the DD ones. An important requirement is thus that the functional used provides a balanced description of both components.

#### 1.2.1.2 Band offsets

To describe the band alignment in a semiconductor heterojunction one can follow three different strategies. The first one consists in using an alternating sequence of slabs A/B/A/B/A/B… repeated along the non-periodic direction of the supercell, "alternating slabs junction" approach;[23–25] in this model an interface between A and B is defined and optimized, but the slabs are not terminated by a surface exposed to vacuum. This approach has the advantage that there is no need to model the surface of a material, provided that no important surface effects are present.

A similar approach makes use of a sequence of surface terminated slabs separated by a vacuum region (__), A/B/__/A/B/__/A/B/__. Which is call "surface terminated junction" approach, here the effect of the two surfaces are present, one for A and one for B, and as in the previous model, the A/B interface is explicitly taken into account.[26]

The third and last approach is the simplest one and is based on the calculation of the properties of the separated, non-interacting, A and B components of the junction, "independent units". These can be calculated using bulk unit cells,[27,28] or finite slab models reasonably converged with respect to the thickness.[27–29]

Once the model has been defined, the next step consists in calculating the band edges and offsets (VBO and CBO) of the two materials, choosing a proper reference to align them. This can be done following the "electrostatic potential line-up" method where the plane-averaged electrostatic potential (*V*) of the heterostructure and the separated components are calculated.[23] Then, the valence band maximum, VBM, and the conduction band minimum, CBM, of the composing units are aligned using as a common reference the macroscopic average of *V* or *V* stationary points.[23,30–34] An alternative approach, which has a similar accuracy, is to use the core levels (e.g. the energy of the 1s orbitals).[35–37]

### 1.3 Co-catalyst

Nanostructuring is the other way to improve the photoactivity in materials and a clear example of nanostructuring is the use of co-catalyst, which constitutes of a pair of cooperative catalysts that improve each other's catalytic activity.

Here we give attention to a particular case of co-catalyst which is the Single Atom Catalyst (SACs) with the intention to describe the hydrogen evolution reaction (HER). SACs consist of isolated metal single atoms (SAs) dispersed onto the support surfaces and possess unique chemical and physical properties often different from those of the conventional supported metal nanoparticles (NP) catalysts. Among the various co-catalysts proposed in literature it is possible to find the platinum-group elements (PGE) such as Pt, Pd, Rh Ru, and Ir.[38–43] A particular case that does not form part of the PGE but present an excellent photocatalytic hydrogen evolution is gold.[44,45] However, due to the low abundance of the PGE and high prices, a searching for novel inexpensive materials than can reproduce the performance of the PGE and gold has started in the last decades. Materials based on earth-abundant elements, such as the first-row transition metals (e.g., Fe, Co, Ni, or Cu), have been recognized as good co-catalysts for the hydrogen evolution.[46–49]

Then, the use of proper co-catalysts loaded on the light harvesting semiconductor could promote or accelerate the photocatalytic courses for the hydrogen evolution reaction. Co-catalyst can serve as the reaction sites and catalyze the reactions, promote the charge separation and transport driven by junctions/interfaces formed between the co-catalyst and the light harvesting semiconductor.[50] In this area also the DFT can help to elucidate the best SACs than can be used for the HER. Figure 3 schematically shows the areas where SACs are applied. In this thesis, two sub-chapter are dedicated to the study of SACs supported in 2D structures and in particular nitrogen-doped graphene for the HER.

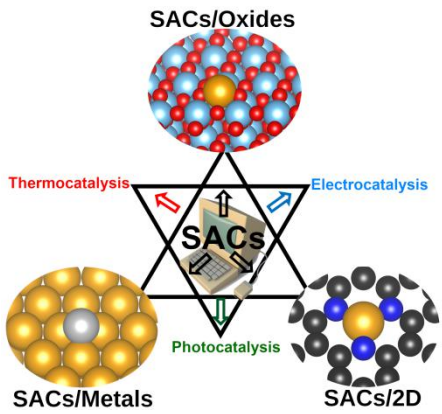


**Figure 3.** Schematic representation of Single Atom Catalyst (SACs) applications.

# Chapter II: Methodological aspects

## 2.1 Theoretical description of oxide semiconductors

Density functional theory (DFT) is one of the commonly used method to study the electronic structure of oxide semiconductors.[12] One of the fundamental properties of a semiconductor is the band gap, which determines the optical, electrical and chemical properties. Band gap calculation is usually based on the analysis of the position of the Kohn-Sham (KS) energy levels,[51] despite the fact that DFT is a ground state theory and that Kohn-Sham orbital energies provide, in principle, just a crude approximation of the band gap. The measurement of the band gap implies to excite one electron from the valence band (VB) to the conduction band (CB, optical transition) or to remove or add electrons to the system as in photoelectron spectroscopies, causing important electronic and geometrical relaxations that follow the ionization process. In the first case the measures are affected by the formation of excitons, in the second it is often difficult to distinguish initial from final state effects.[52] Nevertheless, Kohn-Sham band gaps are widely and universally used due to their simplicity and rapid calculation.

A well-known problem is related to the choice of the exchange-correlation functional in density functional theory (DFT) calculations. The limitations of the generalized gradient approximation (GGA) are known; in particular the self-interaction problem, which results in the underestimation of the band gaps in semiconductor.[53] Unfortunately, this underestimate is not systematic, and varies substantially case by case. Furthermore, delocalized solutions for excited electrons and holes are favoured over localized solutions, often leading to un-physical results. In order to partly solve these issues, various strategies have been implemented, such as the use of the Hubbard correction, U, that can be incorporate to the local and semilocal density functionals (LDA+U and GGA+U).[54,55] The role of the U term is to treat the strong on-site Coulomb interaction of localized electrons by adding a Hubbard-like term. This provides a simplified description of strongly correlated electronic states (d and f orbitals), while the rest of the valence electrons is treated by the usual DFT approximations.

The other approach to address the self-interaction error is the use of hybrid functionals. Which, were introduced in quantum chemistry in order to improve the prediction of thermochemical properties, e.g. atomization energies, of molecular systems.[56,57] They are constructed by adding a portion of the exact exchange energy $E_x$ to GGA type functionals, whose exchange and correlation contributions are denoted as $E_x^{GGA}$ and $E_c^{GGA}$, respectively. The general form of the exchange-correlation energy for one-parameter hybrid functionals is defined by following equation:

$$E_{xc} = \alpha E_x + (1-\alpha) E_x^{GGA} + E_c^{GGA} \qquad \text{Eq. (1)}$$

Where the fraction of exact exchange is denoted as α, in the case of one-parameter hybrids, may vary from 0 (pure GGA functional) to 1 (Kohn–Sham exact exchange potential).[58] Several hybrid functionals have been designed, which differ by the specific choice of the GGA functional approximating the semi-local part, and the value of α.[59] Among others, the PBE0[60] and B3LYP[56,57] functionals deserve special mention. The B3LYP functional does not follow equation (1), but is based on a different three-parameter formula fitted to reproduce a set of experimental data (20% of exact exchange, or α = 0.20). Instead, PBE0 builds on the original Becke's one-parameter hybrid with α = 0.25. The first applications of hybrid functionals to solids appeared at the end of the 90s', showing a significant improvement over GGA in the band gaps description of semiconductors, as well as of other properties.[53,61] Since then, hybrid functionals specifically designed for solid systems have also been developed. In particular, range-separated hybrids were proposed so that the Coulomb kernel in the exchange energy is separated in short-and long-range contributions. A range-separated hybrid where the long-range part of the Coulomb interaction is neglected (short-range hybrids) is the Heyd–Scuseria–Ernzerhof (HSE)[62,63] functional for which the short-range exchange fraction is set to 0.25. Screened exchange functionals have been successfully applied to the calculation of the properties of solids.[15,64,65]

Hybrid functionals are extremely useful in the description of electron localization. Different from semilocal functionals, where the self-interaction error over-delocalizes electrons and holes, introducing a portion of exact exchange in hybrid functionals partially corrects the self-interaction error, giving a qualitatively correct representation of localized electrons and holes, an important aspect in photocatalysis. A direct proof of this comes, among others, from the direct comparison of measured and computed EPR properties.[66]

A variant of the hybrid functionals are the dielectric-dependent hybrid functionals, whose considered the effect of the dielectric constant of the materials.

### 2.2 Dielectric-dependent hybrid functionals

As with LDA+U and GGA+U, the choice of the correct value for the exact exchange fraction α in hybrid functionals remains an issue. The value of α has dramatic consequences on the band structure and, in particular, on the band gap. For example, PBE0 overestimates by more than 50% the gap of silicon.[67] Clearly, a fixed value of α (e.g. 0.20 for B3LYP or 0.25 for PBE0) does not guarantee a comparable accuracy in the description of the electronic properties of a broad set of materials. An alternative approach is to consider the exact exchange fraction as a term which depends on the bonding characteristics and, therefore, on the electronic and dielectric properties of the material. Then, the exact exchange fraction is related to the strength of the electronic screening in a solid. Quasiparticle corrections to DFT eigenvalues are inversely proportional to the static dielectric constant of a material.[68,69] In this respect, the exact exchange fraction is given by the inverse of the static dielectric constant.[70,71] For dielectric-dependent hybrids, the exchange-correlation potential takes a functional form similar to PBE0 (see equation (1) above), but with an exchange fraction which is system dependent:[70,71]

$$\alpha = \frac{1}{\varepsilon_\infty} \qquad \text{Eq. (2)}$$

Clearly, α depends on the approximations made in computing the dielectric constant, $\varepsilon_\infty$ , or on the experimental errors in case this is taken from experiment. For a deeper discussion of dielectric dependent (DD) hybrid functionals the reader is referred to a recent reviews on this topic.[20–22,72]

There are various ways to perform a DD hybrid functional calculation. One can take the experimental dielectric constant of a material and derive the corresponding α value - equation (2); in this case, the method has some empirical flavour due to the use of an external parameter. The other approach is to compute the dielectric constant starting from an initial α value, generate a new DD α, and iterate the procedure until self-consistency is obtained. This leads to a method where the dielectric constant is derived theoretically and the method can be considered as parameter-free, fully ab initio. Ideally, the computed and measured dielectric constants should be similar, as well as the α values and the description of the electronic structure.

From a purely theoretical point of view, the self-consistent determination of the dielectric constant is preferable as it does not require to rely on experimental data. An alternative model to the dielectric dependent approach to fix the amount of non-local exchange and provide good band gaps is to design functionals that satisfy the Koopmsn's condition, such as those based on a set of parameters suggested by Moussa et al.,[73] and later by Deák et al,.[74]

### 2.3 Charge transition levels

Despite all the problems mentioned above, KS-DFT is still widely used to estimate the band gap of highly correlated solids, such as transition metal oxides and in particular, monoxides of the elements located is the right side of the first transition metal row (Mn, Fe, Co, Ni, Cu) and among other oxides ($CuWO_4$, $Fe_2O_3$, $VO_2$, etc.,). These oxides are magnetic insulators, i.e. they exhibit insulating character, high spin configurations, and often antiferromagnetic ordering, i.e. nearby metal cations display opposite spin. Their electronic structure is characterized by a predominant contribution of metal's *d*-orbitals both to the valence and the conduction bands. Differently from the charge-transfer oxide insulators, where electronic excitations correspond to an actual transfer from O *2p* orbitals to metal's *d*-orbitals, electronic excitations in these materials are rather described as an electron hopping from one metal center to the next. Their description in terms of band model raises fundamental questions, and for this reason they are classified as magnetic insulators or even as Mott-Hubbard insulators in the intermediate regime.[75] In this class of materials narrow bands are formed due to the very localized nature of the 3*d* orbitals of late transition metals or the *f* orbitals of rare-earth elements. This is also the reason why these are often referred to as highly correlated solids. The treatment of complex oxides requires to go beyond the analysis of KS levels,[76] and more accurate but also computationally demanding approaches have been proposed, such as the GW[77] or the Dynamical Mean-Field Theory (DMFT) methods.[78]

In a sub-chapter of this thesis, attention is given to; MnO, FeO, CoO, NiO, and CuO oxides, which are materials characterized by the presence of atomic like cation 3*d* orbitals occupied by a number of electrons that goes from 5 (Mn) to 9 (Cu). This leads to the presence of occupied and unoccupied metal 3*d* states and a permanent magnetic moment, all these systems are antiferromagnetic at the ground state. A very simplified model to describe conductivity in these systems has been proposed by Hubbard in 1963.[79]

In the Hubbard model the electron mobility is due to the excitation of one electron from a metal cation to an adjacent neighboring cation (hopping) according to the following equation (where the oxidation state of the cation is that of the TM monoxides):

$$M^{2+}(3d^n) + M^{2+}(3d^n) \rightarrow M^{3+}(3d^{n-1}) + M^{+}(3d^{n+1}) \qquad \text{Eq. (3)}$$

According to this oversimplified view, the band gap ($E_g$) of the system, is approximated as $E_g$ = U = I – A, where I and A are the ionization potential [$M^{2+}(3d^n) \rightarrow M^{3+}(3d^{n-1}) + e^-$] and the electron affinity [$M^{2+}(3d^n) + e^- \rightarrow M^{+}(3d^{n+1})$] of a $M^{2+}(3d^n)$ ion. Thus, the band gap can be approximated as the difference between two total atomic energies, that of the metal cation with one electron removed (I) and with one electron added (A). Of course, solid-state effects largely contribute to modify the band gap from what predicted based on this model. These have been included in the classical Zaanen, Sawatzky and Allen (ZSA) theory.[80] The ZSA model of insulating TM compounds is based on a comparison of the on-site correlation energy, $U_{dd}$, and the charge transfer energy, $\Delta$. When $U_{dd} < \Delta$ the energy gap $E_g$ is determined by $U_{dd}$ ($E_g \approx U_{dd}$) corresponding to the transition $3d^n + 3d^n \rightarrow 3d^{n-1} + 3d^{n+1}$ giving rise to a Mott-Hubbard insulator. When $U_{dd} > \Delta$ the charge transfer energy $\Delta$, corresponding to the transition $3d^n \rightarrow 3d^{n+1}L$ (where L indicates a hole on a ligand), determines the gap ($E_g \approx \Delta$) and the system is classified as a charge transfer insulator. In the ZSA model the relative weight of the two terms is empirically defined, while here it is the result of the full ab initio determination of the final wave functions.

It is possible to estimate the position of energy levels introduced by an isolated defect in the gap of a semiconductor by considering the charge transition levels (CTLs) approach.[81–84] Where the total energies of different electronic states are considered instead of one-electron KS energies. Usually the transition level $\epsilon$(q/q') is defined as the Fermi level, referred to the top of the VB, for which the formation energies of defects in the charge states *q = q' + 1* and *q'* are equal. Here the CTLs can be derived on the basis of Janak's theorem.[85] This method is rather accurate when used in connection with hybrid functionals,[86–91] and allows to circumvent the problem of the calculation of the total energy of charged supercells, which is not possible with the CRYSTAL[92] code because of the interaction with the balancing background of charge. The charge transition levels approach imply the creation of charged species, whose stability is largely influenced by their reciprocal distance. It is thus mandatory to check the convergence of the CTLs gap with respect to the supercell size.

The energy gap of TM oxides has been estimated as the difference between the ionization potential (I) and the electron affinity (A) of the system. The procedure starts from the ground state electronic structure of the neutral oxide, by removing or adding one electron, respectively, forming the corresponding +1 and -1 charged states, respectively. Optical transition levels ($\epsilon^{opt}$) are estimated while keeping the atoms fixed in their fundamental state's positions, while thermodynamic transition levels ($\epsilon^{therm}$) are calculated on the fully relaxed charged system.[93]

The formation energy $\epsilon^{opt}$(q/q') of these charges states has been obtained following the approach described in details by Gallino et al,.[91] where the Janak's theorem is used starting from this expression:

$$\epsilon^{opt}(q/q') = \frac{E_{D,q'} - E_{D,q}}{q - q'} - E_v = \frac{\int_0^1 e_{h+1}(N-n)dn}{q - q'} - E_v \qquad \text{Eq. (4)}$$

$E_{D,q'}$ and $E_{D,q}$ are the total energies of the defective systems with charge q' and q = q'+1, respectively, while $e_{h+1}$(N) is the KS eigenvalue of the lowest unoccupied (h+1) state of the *q* charged state (*N* electrons). $E_v$ is the Valence Band Maximum of the neutral system. After taking into account the mean value theorem for the integrals, it is possible to compute the formation energy $\epsilon^{opt}$(q/q') of the charged states following eq. (5) reported below, where the calculation of two eigenvalues is required instead of all the eigenvalues of n between 0 and 1:

$$\epsilon^{opt}(q/q') = \frac{e_{h+1}(N) + e_{h+1}(N+1)}{2} - E_v \qquad \text{Eq. (5)}$$

Here, $e_{h+1}$(N) and $e_{h+1}$(N+1), are the KS eigenvalues of the lowest unoccupied state (LUMO) in the charge state *q* and the highest occupied state (HOMO) in the charge state *q'*, respectively.

The ionization potential, I, can thus be obtained as:

$$\epsilon^{opt}(+1/0) = \frac{LUMO(+1) + HOMO(0)}{2} - E_v = -I \qquad \text{Eq. (6)}$$

while the electron affinity, A, can be written in terms of the corresponding transition levels:

$$\epsilon^{opt}(0/-1) = \frac{LUMO(0) + HOMO(-1)}{2} - E_v = -A \qquad \text{Eq. (7)}$$

Then, the optical energy gap, $E_g$ *(opt)* is calculated as the difference of ionization potential and electron affinity, which in turn is the difference between $\epsilon^{opt}$(0/-1) and $\epsilon^{opt}$(+1/0) determined with respect to the top of valence band in the host material:

$$E_g(opt) = I - A = -\epsilon^{opt}(+1/0) + \epsilon^{opt}(0/-1) \qquad \text{Eq. (8)}$$

Notice that this definition of optical gap does not include exitonic effects, and that for this reason this quantity is sometimes referred to as the fundamental gap. Optical transition levels ($\epsilon^{opt}$), as stated above, do not include relaxation effects and can be directly compared with the position of the band edges estimated from optical excitation. The direct comparison between experimental excitation energies and calculated band gaps will be based on the optical (fundamental) gaps, i.e. keeping frozen the nuclei configurations. This assumption is based on the shorter time lapse associated to photons absorption/emission (femtoseconds) compared atomic relaxation (picoseconds). On the other hand, it can be interesting to estimate also the effects related to the geometrical relaxation upon trapping of charged species.[91,94] This information may allow us to rationalize the accuracy of DFT-KS gaps, since this effect is generally neglected when looking at KS energy levels of the neutral system. Moreover, the estimate of relaxation energies provides additional information about the non-radiative decay of photoexcited electrons and holes.

### 2.4 Used codes

The systems discussed in this thesis have been studied using the CRYSTAL code[92] where the Bloch functions of the periodic systems are expanded as linear combination of atom centred Gaussian functions (https://www.crystal.unito.it/index.php); and the VASP code[95–97] based on augmented plane waves where the one electron wave-functions are derived from a pseudo orbital by means of a linear transformation (PAW method, https://www.vasp.at/). The use of two computer codes was motivated by the different efficiency in calculating the band structure with hybrid functionals; on conventional CPUs the atom-centered CRYSTAL code does not undergo relevant loss of efficiency when doing hybrid functional calculations. However, the increased computing power in the new generation of architectures makes feasible hybrid functional calculations also with plane-wave codes, as VASP. Further computational details can be found in the chapters described below.

# Chapter III: Fundamental material properties

When one wants to deal with the description of fundamental properties of material several aspects need to be considered. Here we describe in particular two cases. The first one is related to the theoretical description of the electronic structure of magnetic insulators, and in particular of transition metal oxides (TMOs) like MnO, FeO, CoO, NiO and CuO, which poses several problems due to their highly correlated nature. To do this we present a different approach (Charge Transition Levels, CTLs) based on the assumption that the band gap in some TMOs can have partial Mott-Hubbard character, and can be defined as the energy associated to the process: $M^{m+}(3d^n) + M^{m+}(3d^n) \rightarrow M^{(m+1)+}(3d^{n-1}) + M^{(m-1)+}(3d^{n+1})$. The band gap is thus associated to the removal (ionization potential, I) and addition (electron affinity, A) of one electron to an ion of the lattice.

In the second part is treated the description and rationalization of the role of quantum confinement in the group III-V semiconductor thin films by studying (110) surfaces of each semiconductor.

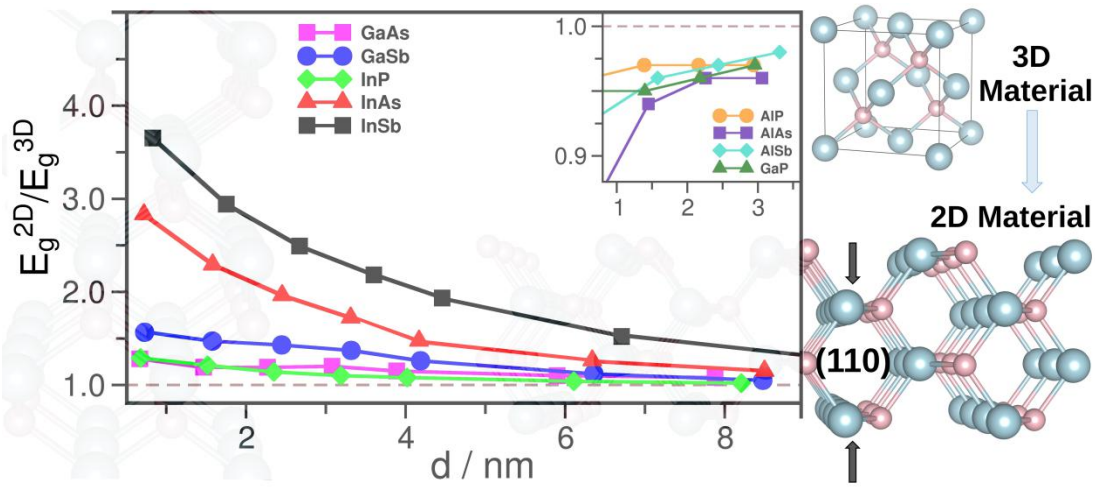

## 3.1 Band gap description of magnetic insulators from a charge transition levels approach

The goal of this sub-chapter was the extension of CTLs from the domain of point defects to a bulk property such as the band gap. The results show that the calculation based on CTLs provides band gaps in better agreement with experiments than the KS approach, with direct insight into the nature of the gap in these complex systems. In the following sections are described some computational details, the results, a general discussion and the summary.

### 3.1.1 Introduction

One of the fundamental properties of a material is the band gap, which determines the optical, electrical and chemical properties. In DFT, the calculation of the band gap is usually based on the analysis of the position of the Kohn-Sham (KS) energy levels,[51] despite the fact that DFT provide just a crude approximation of the band gap. KS-DFT in the Local Density (LDA) or Generalized Gradient (GGA) approximation is known to produce band gaps that are too small due to the self-interaction error.[98] As was mentioned in the method section, more accurate description of the KS band gap can be obtained by using the hybrid functionals[56,57,62,99] or the DFT+*U* approach.[54,55] However, also hybrid functionals and the DFT+*U* method are not free from limitations. In hybrid functionals the exchange energy is constructed including a portion $\alpha$ of exact Fock exchange, where $\alpha$ depends on the formulation used. The same applies to the determination of the U value in LDA+*U* or GGA+*U* approaches. The dependence of the results on the choice of the $\alpha$ or U parameters represents a severe limitation in the predicting value of DFT calculations of the band gap of insulating and semiconducting materials.

As was already mentioned, KS-DFT is still widely used to estimate the band gap of highly correlated solids (i.e MnO, FeO, CoO, NiO, and CuO). These oxides are antiferromagnetic at the ground state and are characterized by the presence of atomic like cation 3*d* orbitals occupied by a number of electrons that goes from 5 (Mn) to 9 (Cu).

---

The content of this sub-chapter is published in the Journal of Chemical Theory and Computation: L. A. Cipriano, G. Di Liberto, S. Tosoni, and G. Pacchioni, “Band gap in Magnetic Insulators from a Charge Transition Level Approach”, *J. Chem. Theory Comput*., 16, 6, (2020) 3786-3798. https://doi.org/10.1021/acs.jctc.0c00134

To overcome the limitations of the GGA and LDA functionals in the TM monoxides, advanced approaches such as Dynamic Mean-Field Theory,[100–102] Random Phase Approximation,[103,104] and GW[76,105–109] have been applied to fill the gap between the KS band gaps and the experimental ones. However, in this chapter is suggested the CTL scheme, which is an alternative approach to the calculation of the band gap in these systems within the frame of DFT. A first example of this approach has been recently reported for the study of $CuWO_4$, also a magnetic insulator.[110] The idea is the following. In order to go beyond the approximations inherent to KS-DFT, the band gap has been computed starting from the consideration that they are all characterized by rather localized 3*d* orbitals and using a hybrid functional which provide a good description of the ground state properties, to be more specific the PBE0 dielectric-dependent functional have been applied ($PBE0_{DD}$) for this study. Next, the charge transition levels (CTL)[81–84] scheme, normally adopted to compute electronic transitions for defects in insulators was used to estimate the band gap of the material. This procedure, based on adding or removing one electron to the system, and not on one-electron levels of the ground state, is thus an alternative and better-grounded approach and can be used to provide a validation of KS-DFT band gaps.[110] More details about the CTL approach can be found in the methodology chapter.

The use of dielectric-dependent hybrid functionals has shown an improvement in the description of several materials, including inorganic[20,21] and organic compounds;[111] recently, it has also been successfully applied to the same class of solids of interest in this paper, i.e. MnO, FeO, CoO and NiO.[72] It should be mentioned, however, that while dielectric-dependent functionals improve the description of selected solids, this is not necessarily a universal way to cure the problems of hybrid functionals.

### 3.1.2 Computational details

Spin-polarized hybrid functional calculations have been done using the PBE0 formulation[60,99] with the fraction of exact Fock exchange calculated within the Coupled-Perturbed Kohn Sham (CPKS)[112–114] method as implemented in CRYSTAL17 code.[92] Here, calculation based on PBE0 functional, where α was self-consistently determined is refer as $PBE0_{DD}$. The self-consistent dielectric dependent procedure to determine the optimal α on $PBE0_{DD}$ has been done at the experimental geometry.[17]

For sake of comparison, repeated KS calculations with the screened hybrid functional HSE06[62,63] at the geometry optimized with PBE0 have been done.

In order to comparate the effect of the exact Fock exchange on HSE06 functional, the geometry and the self-consistently determined α from $PBE0_{DD}$ were considered: below refer as $HSE06_{DD}$. The choice to rely on α as determined with $PBE0_{DD}$ is due to the fact that the dielectric constant calculation with HSE is not implemented in the CRYSTAL code, results with HSE06 and $HSE06_{DD}$ are reported in the discussion section. Next, the charge transition levels (CTL) scheme which is based on the calculation of energy levels of charged states and goes beyond the approximations inherent to the Kohn-Sham (KS) approach was used to estimate the band gap of the TMOs. Almost all the TM oxides considered here have $Fm\overline{3}m$ [225] point group[115] with the exception of $Cu_2O$ which has a $Pn\overline{3}m$ [224] point group.[116]

Here, the direct or indirect nature of the energy gap for the TM oxides is indicated by *i* or *d*, $E_g^i$ or $E_g^d$, respectively. From CTLs, the direct bang gaps have been computed taking the eigenvalues at the Γ point (HOMO and LUMO), while the indirect band gaps were computed taking the eigenvalues with the highest and lowest energies at other k-points. More details about CTL approach is described in the method chapter.

### 3.1.2.1 Basis sets, supercells, tolerances

Calculations were done considering all electron Alhrichs-type basis sets (Pob-TZVP[117]) for Mn, Fe, Co, Ni, Cu and O atoms. With NiO, the results have been checked versus Pople basis set type and quality, Table 1.

**Table 1.** Effect of the basis set in the KS-DFT indirect ($E_g^i$, in eV) and direct ($E_g^d$, in eV) band gaps, magnetic moment ($\mu_B$/atom), and dielectric constant for NiO.

| NiO | Geom | $E_g^i$ / eV | $E_g^d$ / eV | M / μB/atom | Dielectric constant | Basis set |
|---|---|---|---|---|---|---|
| PBE0(α=0.25) | Opt | 5.30 | 6.44 | 1.71 | 4.75 | |
| PBE0(α=0.25) | Exp | 5.30 | 6.42 | 1.71 | 4.75 | Ahlrichs |
| $PBE0_{DD}$ (α=1/sc-$\varepsilon_\infty$) | Opt | 4.47 | 5.62 | 1.66 | 5.49 | |
| $PBE0_{exp}$ (α=1/$\varepsilon_\infty^{exp}$) | Exp | 4.26 | 5.52 | 1.66 | 5.61 | |
| PBE0 (α=0.25) | Opt | 5.65 | 6.45 | 1.73 | 3.78 | |
| PBE0 (α=0.25) | Exp | 5.79 | 6.61 | 1.74 | 3.68 | Pople |
| $PBE0_{DD}$ (α=1/sc-$\varepsilon_\infty$) | Opt | 5.95 | 6.80 | 1.75 | 3. 59 | |
| $PBE0_{exp}$ (α=1/$\varepsilon_\infty^{exp}$) | Exp | 4.68 | 5.53 | 1.68 | 4.55 | |
| Experiment | | | | 1.90[a,b] | 5.76[c] | |
| XAS+XES | | 4.0[d] | | | | |
| PES+BIS | | 4.3[e] | | | | |
| Optical absorption | | | 3.7[f];3.87[g] | | | |

See reference as: a[118], b[119] c[120], d[100], e[121], f[122] and g[123].

Based on this comparison, the Alhrichs-type basis sets have been chosen because they provide a good accuracy; for instance, on the lattice parameters of the cubic unit cells.[115]

The cutoff value for coulomb and exchange integrals in self-consistent field calculations was $10^{-7}$ for coulomb overlap tolerance, coulomb penetration tolerance, exchange overlap tolerance, exchange pseudo overlap in direct space, and $10^{-14}$ for exchange pseudo overlap in reciprocal space. The SCF calculation was considered converged when the difference in energy between two subsequent cycles was lower than $10^{-8}$ atomic units (a.u.). The sampling of the reciprocal space was adapted to the size of the supercell: a shrinking factor of 8 in the Pack-Monkhorst scheme was adopted for the 2×1×1unit cells, these cells have two TM oxides (TM = Mn, Fe, Co, Ni, and Cu) and two O atoms along the [111] direction and allowed us to compute the AFM and FM solutions in the TM monoxides, and subsequently reduced to 2 when working on larger supercells.

The simulated cells have been fully optimized, both atomic coordinates and lattice parameters, and simulations were considered converged with threshold values of 0.0003 a.u. and 0.0045 a.u. for root-mean-square (rms) and the maximum absolute value of the gradient, respectively, and of 0.0012 a.u. and 0.0018 a.u. for rms and maximum displacements, respectively. The ferromagnetic (FM) and a few possible antiferromagnetic (AFM) configurations were considered for each oxide. Only the most stable magnetic structure was used here. When evaluating charge transition levels it is more difficult to reach convergence, especially with large supercells. In these cases, the tolerance on the total energy was changed to $10^{-7}$ a.u. The truncation criteria for the two-electron integrals were unchanged.

The density of states (DOS) curves for the 2×1×1 unit cells were determined with shrinking factor 10 for reciprocal space Pack-Monkhorst net and also for reciprocal space Gilat net, see Figure 4 for the DOS of each oxide.

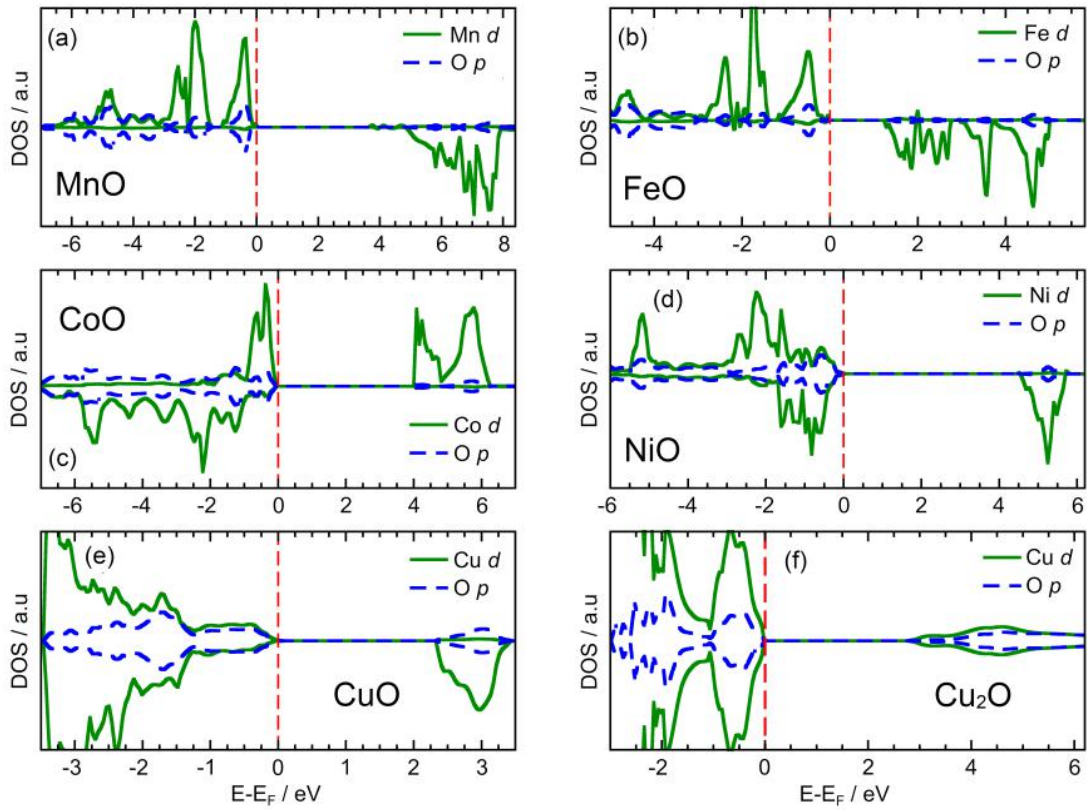


**Figure 4.** Density of States for: (a) MnO, (b) FeO, (c) CoO, (d) NiO, (e) CuO, and (f) $Cu_2O$ at $PBE0_{DD}$ level, for FeO was considering the experimental dielectric constant. Green line and blue dotted line represent the d states for the cation (Mn, Fe, Co, Ni, Cu) and p states for O, respectively. The red dotted line represents the Fermi level. [93]

### 3.1.3 Results

#### 3.1.3.1 Test case of the CTL approach: $Cu_2O$

The first case is that of $Cu_2O$, a non-magnetic oxide. Nevertheless, it has a narrow Cu 3*d* band and can be used to verify if the procedure adopted for the calculation of the band gap using the CTLs is sufficiently accurate. The first set of calculations was the determination of the optimized ground state properties using the standard PBE0 functional, and the corresponding dielectric dependent version, $PBE0_{DD}$. For this system a self-consistent dielectric dependent $\alpha = 0.245$ was found, corresponding to a dielectric constant equal to 4.09, Table 2. This value is practically the same dielectric constant found in PBE0 for the optimized geometry. Therefore, the two approaches provide very similar direct KS band gaps, $E_g^d$ (PBE0) = 2.84 eV, and $E_g^d$ ($PBE0_{DD}$) = 2.79 eV, Table 2.

The dielectric constant computed for the full optimized $Cu_2O$ structure at the PBE0 level was ~37% smaller than the experimental one, 6.46.[124] Similar values are also obtained by determining the optimal $\alpha$ ($PBE0_{DD}$), as reported in Table 2.

Experimentally, optical absorption studies report values of the direct band gap between 2.17 and 2.62 eV,[125] thus the PBE0 and $PBE0_{DD}$ values, about 2.8 eV, are close to the upper limit of the experimental measurements. As was already mentioned, optical absorption experiments usually provide a lower bound to the real band gap due to the presence of excitons. After determining the optimal exact-exchange percent on the $PBE0_{DD}$ functional, the CTLs at the level of $PBE0_{DD}$ have been checked versus supercell size using cells containing 6, 12, 24, 48, 72 and 108 atoms, Table 3.

**Table 2.** KS-DFT direct band gap ($E_g^d$, in eV), and dielectric constant for $Cu_2O$.

| $Cu_2O$ | $E_g^d$ / eV | $\varepsilon_\infty$ |
|---|---|---|
| PBE0 (α=0.25) | 2.84 | 4.06 |
| $PBE0_{DD}$ (α=1/sc-$\varepsilon_\infty$) | 2.79 | 4.09 |
| Exp. | 2.17-2.62[a] | 6.46[b] |

See references as: a = optical absorption[125], and b[124].

**Table 3.** Direct ($E_g^d$, in eV) and indirect ($E_g^i$, in eV) band gap of $Cu_2O$ for supercells of increasing size computed according to the CTLs method.

| Cell size | 1×1×1 | 2×1×1 | 2×2×1 | 2×2×2 | 3×2×2 | 3×3×2 |
|---|---|---|---|---|---|---|
| n. of atoms | 6 | 12 | 24 | 48 | 72 | 108 |
| $E_g^d$ / eV | 0.14 | 1.52 | 2.02 | 2.63 | 2.47 | 2.55 |
| $E_g^i$ / eV | 0.05 | 2.52 | 2.70 | 2.99 | 3.19 | 3.10 |

The nature of the transition has been considered and in $CuO_2$ the ionization involves a $Cu^+(3d^{10})$ ion which formally becomes $Cu^{2+}(3d^9)$. On the other hand, the addition of one electron to the supercell results in a delocalized electron that occupies the Cu 4sp band. Not suprisingly, the 6-atoms unit cell is too small and cannot be used to obtain reasonable values of the gap (calculated neglecting structural relaxation), Table 3. Even the 12-atoms cell is not sufficient, while the results tend to become stable ($E_g$ variations within 0.2 eV) with larger supercells, Figure 5. Considering the largest cell, 3×3×2 (108 atoms), it gives a direct band gap of 2.55 eV, in excellent agreement with the experimental estimates (2.17-2.62 eV, see also Figure 5).

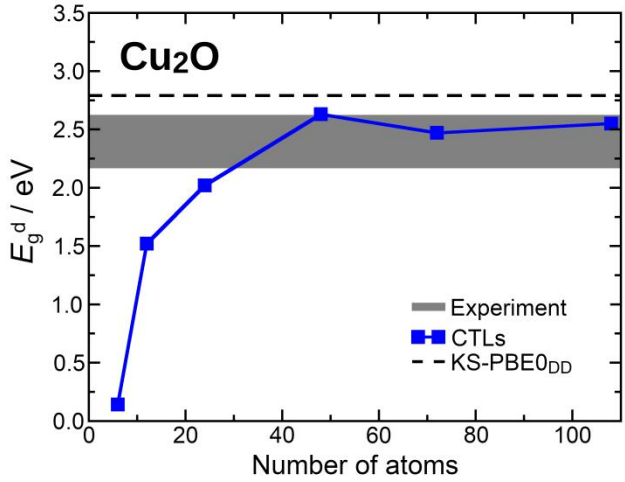


**Figure 5.** Direct band gaps of $Cu_2O$ computed with the CTLs approach as a function of the supercell-size. The black dotted line represents the direct KS-$PBE0_{DD}$ band gap; the grey interval represents the range of experimental values. [93]

The charged cells have been relaxed in order to evaluate the impact of structural relaxation, finding for the largest supercells small relaxation effects, around 0.11 eV. The gap values computed with the CTLs approach are quite similar to those obtained at the $PBE0_{DD}$ KS-level, see Tables 2 and 3, and Figure 5. In particular, the direct band gap obtained with CTLs (2.55 eV) is within the experimental range (2.17-2.62 eV), and it is slightly closer to experiment than the KS one (2.79 eV). On one side this validates the procedure followed; on the other side it provides a justification for the use of the KS method to estimate the band gap of $Cu_2O$. Having demonstrated that the procedure works for the simple case of the non magnetic $Cu_2O$ oxide, more complex TM oxides were analyzed; MnO, FeO, CoO, NiO and CuO respectively.

### 3.3.3.2 MnO

In the ground state, due to the octahedral crystal field, the $Mn^{2+}$ ion has a $(t_{2g})^3(e_g)^2$ configuration, with five unpaired electrons per Mn ion. A spin population of 4.82 $\mu_B$ per Mn ion was computed, very close to the nominal value, indicating a high level of ionicity of this oxide. Using the spin population as a measure it was identified that the covalent contribution is less than 4%. At the PBE0 level we found that the AFM state is 0.16 eV more stable than the FM one and for the reason the AFM configuration was used in the following studies. At this level of theory, MnO exhibits an indirect band gap of 3.93 eV and a direct gap of 4.62 eV. The dielectric constant is $\varepsilon_\infty = 4.26$.

The next step consisted in the calculation of MnO using the dielectric dependent version of the PBE0 functional. Determining $\varepsilon_\infty$ in a self-consistent way leads to $\varepsilon_\infty$ = 4.34 corresponding to an α value of 0.23; this is quite close to the exchange-correlation value in PBE0 (α = 0.25). It is not surprising that the $PBE0_{DD}$ indirect band gap, $E_g^i$ = 3.70 eV, is slightly smaller than at the PBE0 one. The direct gap, $E_g^d$ = 4.40 eV, is also similar to PBE0, and the magnetization is the same. The computed dielectric constant, 4.25-4.34, is sufficiently close to the experimental one, 4.95.[126] Experimentally, band gap values in the range 3.6-4.1 eV have been reported for MnO, with gaps derived from optical absorption measurements smaller than those from photoemission.

The next step was the determination of the band gap of MnO using the procedure based on the CTLs using supercells of increasing dimensions, Table 4 and Figure 6. First is discussed the nature of the electronic state obtained by adding or removing one electron to/from the supercell. When the positive charged supercell was computed with $PBE0_{DD}$, the spin population of a Mn ion goes from 4.81 $\mu_B$/atom, ground state, to 3.91 $\mu_B$/atom, with a reduction of 0.9 unpaired electrons. The hole is fully localized on a single Mn ion which formally changes its state from $Mn^{2+}(3d^5)$ to $Mn^{3+}(3d^4)$. The addition of an excess electron at the same level of calculation, however, results in different situations depending on the supercell used. With the largest supercell was found a reduced Mn ion with a spin population of 4.29 $\mu_B$/atom, and a localization of about 0.5 excess electrons, which formally goes from $Mn^{2+}(3d^5)$ to $Mn^{+}(3d^6)$. However, the 4×3×3 supercell (as well as any smaller one) gives a completely delocalized solution for the excess electron.

**Table 4.** Indirect ($E_g^i$, in eV) and direct ($E_g^d$, in eV) band gap of MnO for supercells of increasing size computed according to the CTLs method.

| Cell size | 2×2×2 | 4×3×2 | 4×3×3 | 4×4×4 |
|---|---|---|---|---|
| n. of atoms | 16 | 48 | 72 | 128 |
| $E_g^i$ / eV | 2.27 | 3.12 | 3.21 | 3.52 |
| $E_g^d$ / eV | 2.58 | 3.45 | 3.53 | 3.64 |

The smallest supercell for which it was possible to achieve convergence of single-point calculations for the charged systems was the 2×2×2 one. The results become stable starting from the 4×3×2 supercell (48 atoms), Figure 6. The indirect band gap increases regularly by increasing the supercell size, and it becomes $E_g^i$ = 3.52 eV with the 4×4×4 supercell (128 atoms). These values are only a bit smaller than the KS indirect band gap computed at the PBE0, 3.91 eV, or at the $PBE0_{DD}$, 3.70 eV, levels.

Of course, this could be partly fortuitous as the results are not yet fully converged with respect to the supercell size, Table 4 and Figure 6. Unfortunately, going to even larger supercells becomes too demanding in terms of computational resources required. Nevertheless, considering the number in Table 4, the similarity between CTLs indirect band gaps, and KS-DFT one is clear. This provides a validation of the band gap for a magnetic insulator computed at the KS-DFT level. Indeed, the indirect nature of the band gap, which results from KS calculations but also from GW approaches,[105] is confirmed by the present CTLs methodology. Differently from the indirect gap, the direct gap estimate significantly improves, moving from 4.4-4.6 eV (KS-DFT) to 3.5-3.6 eV (CTLs), to be compared with the experimental range (3.6-3.8 eV). As for the previous cases, relaxation effects on large charged cells are small, around 0.15 eV.

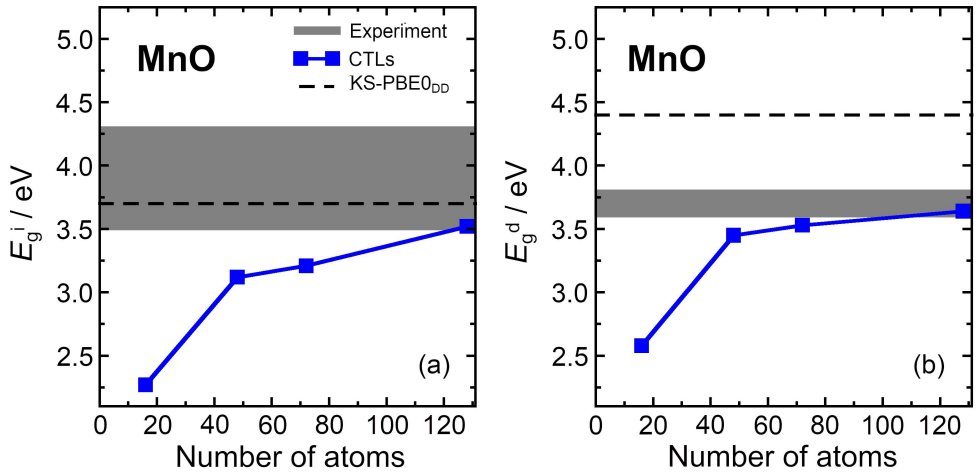


**Figure 6.** (a) Indirect and (b) direct band gaps of MnO computed with the CTLs approach as a function of the supercell-size. The black dotted lines represent the indirect and direct KS-PBE0$_{DD}$ band gap; the grey interval represents the range of experimental values. [93]

### 3.3.3.3 FeO

With FeO, only partial results are reported here due to severe convergence problems. Several attempts and efforts have been done in the tentative to overcome these problems, mostly related to the calculation of the dielectric constant of the material and of the charged supercells required to obtain the band gap with the CTLs approach. Therefore, only KS-DFT results are reported. The AFM state is 0.24 eV lower than the FM one. At the PBE0 level and with full optimization of the unit cell, the gaps are $E_g^i$ = 2.04 eV and $E_g^d$ = 2.11 eV, and the magnetization is 3.73 $\mu_B$/atom. Due to problems in the calculation of the dielectric constant we cannot report PBE0$_{DD}$ results.

Then, we also determined the ground state properties using the average experimental dielectric constant, 10.17 (computed from Ref. 127,128), finding much smaller gaps values (around 0.8 eV) and a similar magnetization.
These data can be compared with literature at the same level of theory (PBE0), but with plane wave codes. A significant difference is found with the recent paper of Liu et al.[72] where $E_g^i$ = 3.02 eV and $E_g^d$ = 3.42 eV are reported. In another PBE0 study by Tran et al.[129] the indirect and direct band gaps are 1.20 and 1.60 eV, respectively. The large differences found in the KS-DFT band gap for FeO show that this system is particularly delicate and is very challenging for DFT-based electronic structure approaches. Alfredsson et al.[130] studied FeO using hybrid functionals and the CRYSTAL code, they found that about 30%-60% of Fock exchange is needed to correctly reproduce the electronic structure of this material. We also noticed that Skone et al.[21] computed the dielectric constants and band gaps for MnO, CoO, and NiO applying the self-consistent dielectric depend method with PBE0 functional in combination with the CRYSTAL code, but they did not report the values for FeO, probably due to the same kind of problems discussed here.

#### 3.3.3.4 CoO

In CoO, the $Co^{2+}$ ion has a $(t_{2g})^5(e_g)^2$ configuration, and three unpaired electrons. A magnetization value of 2.76 $\mu_B$ per Co ion was computed here, close to the nominal value. The covalent contribution is thus 8%, a bit higher than in MnO. At the PBE0 level the AFM state is 0.14 eV lower in energy than the FM one, and for that reason the AFM was used for the $PBEO_{DD}$ and the CTLs. On a fully optimized structure at PBE0 level, CoO exhibits an indirect KS band gap $E_g^i$ = 4.71 eV and a direct gap $E_g^d$ = 4.87 eV. The dielectric constant is $\varepsilon_\infty$ = 4.54. Using the $PBE0_{DD}$ functional a dielectric constant of $\varepsilon_\infty$ = 4.92 is found, which correspond to $\alpha$ = 0.203. Then, the indirect KS band gap becomes $E_g^i$ = 3.93 eV and the direct one $E_g^d$ = 4.03 eV. The change in magnetization with respect to PBE0, 0.03 $\mu_B$/atom, is negligible. The computed KS values span in the range 3.93-4.87 eV, and they are considerably larger than the experimentally reported band gaps which are in the range 2.5-2.7 eV.

In Table 5 are reported the band gaps computed according to the CTLs procedure starting, also in this case, from the $PBE0_{DD}$ ground state. When the positive charged supercell was considered, it was found a Co ion where the magnetization is reduced from 2.72 $\mu_B$/atom, ground state, to 1.90 $\mu_B$/atom, with a reduction of 0.82 unpaired electrons. Thus, the hole is localized on a single Co ion which changes configuration from $Co^{2+}(3d^7)$ to $Co^{3+}(3d^6)$.

The addition of an excess electron leads to one Co ion with magnetization 2.01 $\mu_B$/atom. In this case, the excess electron is fully localized, and the process corresponds to $Co^{2+}(3d^7) + e^- \rightarrow Co^{+}(3d^8)$.

**Table 5.** Indirect ($E_g^i$, in eV) and direct ($E_g^d$, in eV) band gap of CoO for supercells of increasing size computed according to the CTLs method.

| Cell size | 2×1×1 | 4×3×2 | 4×3×3 | 4×4×4 |
|---|---|---|---|---|
| n. of atoms | 4 | 48 | 72 | 128 |
| $E_g^i$ / eV | 0.08 | 2.84 | 3.13 | 2.66 |
| $E_g^d$ / eV | 0.30 | 2.96 | 3.20 | 2.71 |

The smallest supercell for which it was possible to achieve convergence for single point calculations on the charged systems is the 2×1×1 one. However, the corresponding band gaps are still away off any convergence. The results become stable and comparable starting from the 4×3×2 supercell (48 atoms), see Figure 7, even if some oscillations are present. $E_g^i$ becomes 2.66 eV in the 4×4×4 supercell, to be compared with 3.9-4.7 eV (KS-DFT), and is in very good agreement with the experimental estimates, 2.5-2.7 eV. Similarly, the direct band gap, $E_g^d$ = 2.71 eV, is consistent with the experiment, while the KS-DFT one is in the range 4.0-4.9 eV. Even if some oscillations in the bang gap with CTLs are present, this shows that for CoO, going from the KS-DFT approach to the CTLs one there is a clear improvement of the results, leading to a band gap in much better agreement with the experiment, as we clearly observe in Figure 7. For this system, upon a full relaxation of the charged cell a significant structural relaxation following the polaron formation was found, around 0.61 eV.

In conclusion, for CoO the CTLs approach gives indirect and direct band gaps (2.6-2.7 eV) in much better agreement with the experiment (2.5-2.7 eV) than all the KS-DFT calculations considered in this work. It is worth noting this is a particularly challenging system since also other forms of hybrid functionals, such as the range separated HSE06,[72] which overestimate the KS band gap of CoO with $E_g^i$ = 3.50 eV and $E_g^d$ = 4.29 eV, in line with our values computed with PBE0 and $PBEO_{DD}$ functionals.

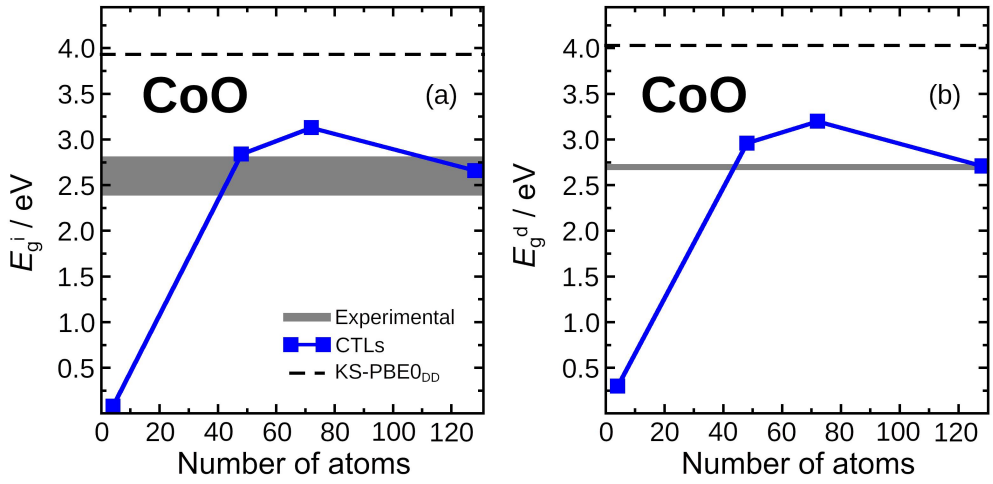


**Figure 7.** (a) Indirect and (b) direct band gaps of CoO computed with the CTLs approach as a function of the supercell-size. The black dotted lines represent the indirect and direct KS-PBE0$_{DD}$ band gap; the grey interval represents the range of experimental values. [93]

### 3.3.3.5 NiO

The $Ni^{2+}$ ion has a $(t_{2g})^6(e_g)^2$ configuration, and a triplet state. The magnetic moment is 1.71 $\mu_B$ per Ni ion, with a deviation of 14.5% from the nominal ionicity. Thus, the covalent character increases as one move from MnO towards the end of the series. As for the other oxides, the ground state is AFM, and in PBE0 is separated by 0.27 eV from the FM solution.

The nature of the gap in NiO has been widely debated and it is generally accepted that it has mixed charge transfer and Mott-Hubbard character, as described in the Zaanen-Sawatzky-Allen model.[80] At the PBE0 level, and optimizing both atomic positions and lattice constants, NiO exhibits an indirect band gap of 5.30 eV and a direct gap of 6.44 eV, and a dielectric constant $\varepsilon_\infty = 4.75$.

At the PBE0$_{DD}$ level we obtain a self-consistent value of $\varepsilon_\infty = 5.49$ corresponding to $\alpha = 0.182$. $E_g^i$ becomes 4.47 eV and $E_g^d$ = 5.62 eV. A small change of 0.05 $\mu_B$/atom was observed in magnetization. At the PBE0$_{exp}$ level (where $\alpha = 0.174$ is obtained as the inverse of the experimental dielectric constant, 5.76),[120] the gap values are about 0.1-0.2 eV smaller than in PBE0$_{DD}$.

Experimentally, band gap values in the range 3.7-4.3 eV have been reported with optical absorption measurements giving smaller gaps than those derived from photoemission or x-ray absorption.[115] With PBE0 functional errors of about 22% are found for the estimation of the indirect band gap, the use of dielectric dependent functionals provides a much better estimates of this quantity (errors of around 7%).

The direct band gap is instead always significantly overestimated by 1.8 eV ($PBE0_{DD}$) and 2.6 eV (PBE0), with errors around 33-41%.

Moving to the results of the CTLs, Table 6. In the positively charged 4×4×4 supercell there is a Ni ion with a magnetic moment of 0.74 $\mu_B$/atom, i.e. 0.92 $\mu_B$/atom lower than in the ground state. This shows that the hole forms in the 3*d* shell, and the Ni ion formally goes from $Ni^{2+}(3d^8)$ to $Ni^{3+}(3d^7)$. Of course, the Ni *3d* levels are hybridized with the O 2p ones, as shown by the DOS curves, and the state is not a purely Ni *3d* state, see Figure 4(d). The addition of an excess electron, however, always results in a completely delocalized solution, with the added electron redistributed over all the Ni atoms of the supercell. Attempts to favor the formation of a polaron associated to the localized charge in the solid failed.

**Table 6.** Indirect ($E_g^i$, in eV) and direct ($E_g^d$, in eV) band gap of NiO for supercells of increasing size computed according to the CTLs method.

| Cell size | 2×1×1 | 2×2×2 | 4×3×2 | 4×3×3 | 4×4×4 |
|---|---|---|---|---|---|
| n. of atoms | 4 | 16 | 48 | 72 | 128 |
| $E_g^i$ / eV | 2.87 | 3.41 | 3.67 | 3.65 | 3.79 |
| $E_g^d$ / eV | 3.16 | 4.24 | 4.18 | 4.12 | 4.17 |

The band gap data start to become reliable from the 2×2×2 supercell (16 atoms), Table 6 and Figure 8. The indirect band gap, $E_g^i$, increases with the cell size until reaching 3.6-3.8 eV when the cell contains more than 50 atoms. For instance, an indirect band gap of 3.79 eV is obtained with the largest supercell. In a similar way, rather stable values are obtained for $E_g^d$, with 4.17 eV being the best estimate (largest cell), Table 10.

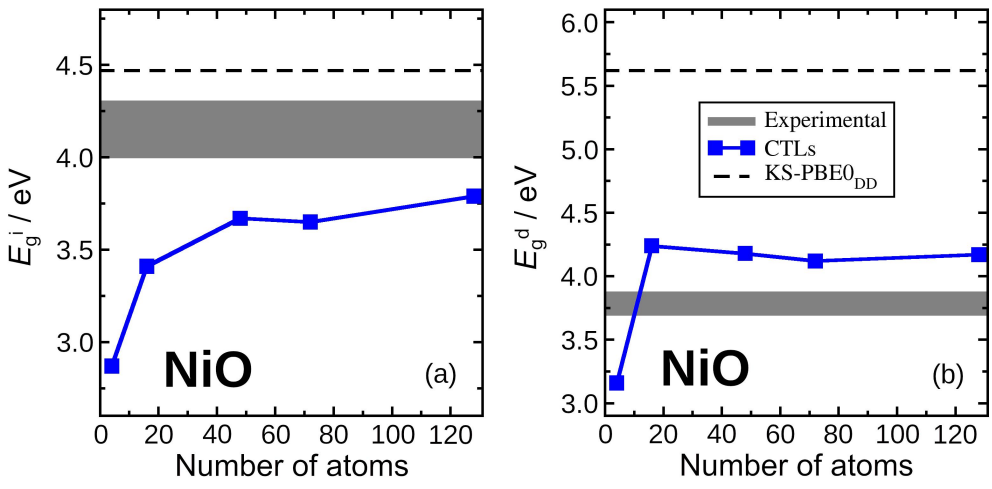


**Figure 8.** (a) Indirect and (b) direct band gaps of NiO computed with the CTLs approach as a function of the supercell-size. The black dotted lines represent the indirect and direct KS-$PBE0_{DD}$ band gap; the grey interval represents the range of experimental values. [93]

The indirect gap computed with CTLs, $E_g^i$ = 3.79 eV, is thus smaller than that computed at the PBE0$_{DD}$ level, 4.47 eV, and not too far from the experiment which reports an indirect band gap between 4 and 4.3 eV.[100,121] The direct band gap computed with CTLs, $E_g^d$ = 4.17 eV, is much smaller than that computed at the KS-PBE0$_{DD}$ level, 5.62 eV, and much closer to the experimental measures of the direct band gap, 3.7-3.9 eV.[122,123] In this respect, the gap computed with the CTLs procedure shows an overall better agreement with experiment compared to the KS approach. As for CoO, we observed a significant energy contribution (around 0.64 eV) arising from relaxation of the charged cells and consequent localization of electrons and holes.

**3.3.3.6 CuO**

CuO is the last TM oxide considered. Here Cu is $Cu^{2+}(3d^9)$. In an octahedral field this would result in a $(t_{2g})^6(e_g)^3$ configuration which is Jahn-Teller distorted so that the unit cell is no longer cubic but becomes monoclinic (C2/c structure). In an ionic picture each Cu should have one unpaired electron. A magnetization of 0.72 $\mu_B$ was computed per Cu ion which means that the material has a substantial covalent contribution, 28%, the largest value found so far. In order to compare the relative stabilities of the AFM and FM solutions a double cell was used. In CuO there are four different AFM configurations: AFM1 (↑↑↓↓), AFM2 (↑↓↑↓), AFM3 (↓↑↑↓), and AFM4 (↑↓↓↑), all quite close in energy, but the last one, AFM4, is the most stable and is 0.10 eV lower in energy than the FM configuration.

At the PBE0 level CuO exhibits an indirect KS band gap of 3.48 eV, a direct gap of 4.37 eV, and a dielectric constant of $\varepsilon_\infty$ = 5.05. Differently from the previous systems, non-negligible changes on the band gap are observed if the calculations are done using the experimental geometry. The band gap is reduced by about 0.3 eV, showing that this property is more sensitive to structural changes than the magnetization or the dielectric constant. This is due to the deviation of the PBE0 lattice parameters compared to experiment: *a*, *b*, *c* and β changed from 4.653 Å, 3.410 Å, 5.108 Å and 90.48° (exp.)[131] to 4.839 Å, 3.199 Å, 5.018 Å and 102.73° (PBE0).
For the PBE0$_{DD}$ calculations we obtain $\varepsilon_\infty$ = 5.74, not far from the experimental value, 6.46.[124] This corresponds to an $\alpha$ value of 0.174, which provides a PBE0$_{DD}$ $E_g^i$ = 2.29 eV, and $E_g^d$ = 3.18 eV. A small reduction of 0.06 $\mu_B$/atom occurs in the magnetization with respect to PBE0. These values can now be compared with the experimentally reported band gaps which are in a range 1.4-1.7 eV.

The results with the CTLs method are reported in Table 7 and Figure 9. Removing or adding one electron to the neutral cell (treated with $PBE0_{DD}$) results in both hole and excess electron largely delocalized on the Cu 3*d* states. This is different from the previous cases and can be attributed to the higher degree of covalency in the material.

**Table 7.** Indirect ($E_g^i$, in eV) and direct ($E_g^d$, in eV) band gap of CuO for supercells of increasing size computed according to the CTLs method.

| Cell size | 1×1×1 | 2×2×1 | 2×2×2 | 2×3×2 | 3×3×2 |
|---|---|---|---|---|---|
| n. of atoms | 8 | 32 | 64 | 96 | 144 |
| $E_g^i$ / eV | 0.77 | 2.13 | 2.01 | 2.39 | 2.15 |
| $E_g^d$ / eV | 1.65 | 2.45 | 2.41 | 2.60 | 2.55 |

The small 2×2×1 supercell containing 32 atoms provides direct and indirect gaps, 2.13 and 2.45 eV, respectively, which are quite close to those obtained with the largest supercell, Table 7 and Figure 9. The indirect band gap, $E_g^i$, becomes 2.15 eV in the 3×3×2 supercell; the value seems to be reasonably converged (within roughly 0.2 eV). Notice that this value is quite close to the KS indirect band gap computed at the $PBE0_{DD}$ level, $E_g^i$ = 2.29 eV. The best estimate of the indirect band gaps with the CTLs (2.15 eV) is larger than the experimental values, 1.4-1.7 eV, but in better agreement than the KS band gap at the PBE0 or $PBE0_{DD}$ levels, 3.48 eV and 2.29 eV, respectively. Similarly, the best estimate of the direct band gap with CTLs, (2.55 eV) is significantly closer to the experimental range (1.4-1.6 eV), than KS band gaps at the PBE0 or $PBE0_{DD}$ levels, 4.08 eV and 3.18 eV, respectively. Once more, CTLs provides better values than the KS-DFT approach. As for previous cases (MnO and $Cu_2O$), relaxation effects on large charged cells are small, around 0.09 eV.

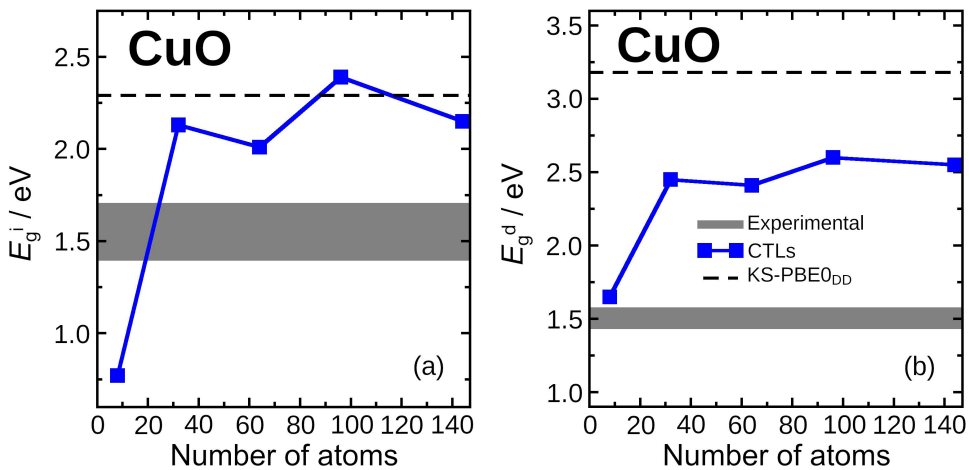


**Figure 9.** (a) Indirect and (b) direct band gaps of CuO computed with the CTLs approach as a function of the supercell-size. The black dotted lines represent the indirect and direct KS-$PBE0_{DD}$ band gap; the grey interval represents the range of experimental values. [93]

### 3.1.4 Discussion and summary

In this sub-chapter we have addressed the complex nature of transition metal oxides with magnetic character and their band gap. MnO, CoO, NiO, CuO have been studied with both hybrid functional calculations and with an alternative procedure based on the charge transition levels. $Cu_2O$ has also been considered as a test case of non-magnetic oxide. The method is based on the use of charge transition levels (CTLs) and the band gap is estimated from energy levels of the material with one electron added and one electron removed. FeO has been studied only at the hybrid functional level since insurmountable convergence problems have been encountered in the calculation of the CTLs for this oxide. The idea behind the CTL approach to the calculation of band gaps is that some oxides have very localized 3*d* states and can be described with the Hubbard model. The approach, however, is fully ab initio, and the nature of the final wave function for the generated electron and hole is determined self-consistently and can be localized or delocalized.

The work had two objectives. First, a completely different way to compute the band gap of a highly correlated material is proposed, based on the calculation of energy levels of charged states; in this respect, the study provides a test of the validity of the KS approach for the calculation of the band gap of this class of highly correlated solids (all display indirect band gap with exception of $Cu_2O$). Second, the analysis of the electron and spin densities of the system with one electron added and one electron removed allows one to better define the nature of the fundamental electronic transition. The results show that this is related to the excitation from a more or less localized filled 3*d* level of a TM ion to the empty 3*d* states of neighboring TM ions, depending on the Mott-Hubbard vs. charge-transfer nature of the material.

The method proposed is parameter free. If one uses a dielectric dependent hybrid functional as a starting point, the amount of Fock exchange to be used, α, can be deduced from the dielectric constant of the material, $\alpha = 1/\varepsilon$, eliminating the necessity to tune the α value against experimental values or the problems caused by a fixed value of this parameter. However, the approach is general and any hybrid functional can be used as a starting point for the calculation of the band gap with CTLs.

With this fully ab initio approach, which takes into account effects induced by extra electrons/holes in the system, we computed direct and indirect band gaps for the series of oxides mentioned above. Figure 10 reports the band gaps as a function of the covalent fraction of the oxides considered.

As already pointed out above, when moving to the right of the periodic table we find a systematic increase in covalent character.

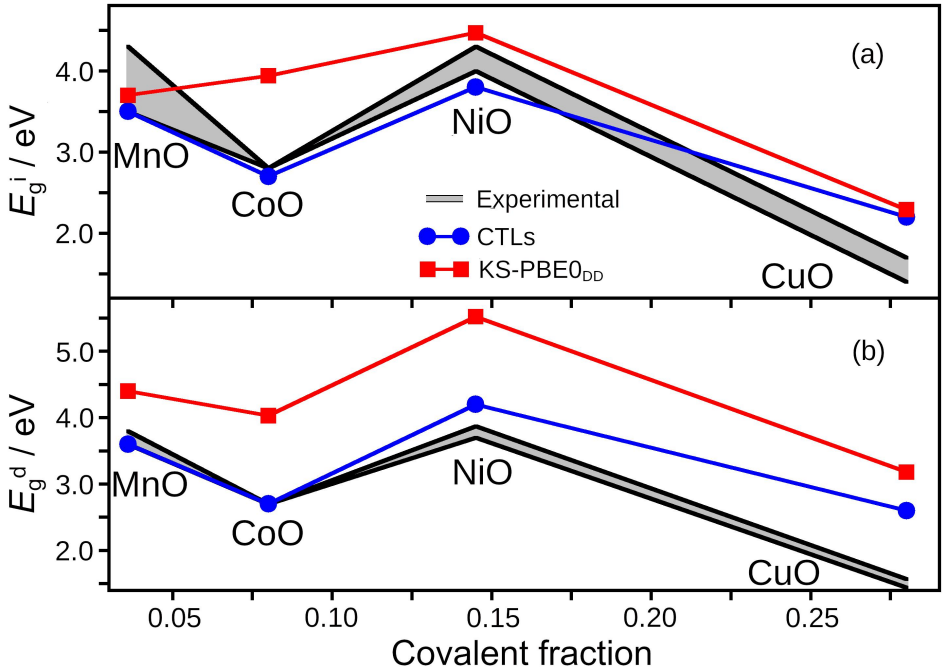


**Figure 10.** Trend of band gaps as a function of the covalent fraction of the oxides. Panel (a) is for indirect band gaps ($E_g^i$); panel (b) reports direct band gaps ($E_g^d$). Grey intervals indicate the range of experimental values. Blue dots are for band gaps calculated via CTLs, while red squares are for KS band gaps. [93]

In general, the indirect band gaps computed with the CTLs are slightly better than those obtained with a hybrid functional, Figure 10(a). This shows that the use of KS-DFT in combination with hybrid functionals for the study of highly correlated oxides provides sufficiently accurate results, despite the intrinsic limitations present in the KS estimate of band gaps. On the other hand, we have found a clear improvement in the direct band gap estimate, Figure 10(b). In all cases considered the band gap obtained with CTLs is found to be in better agreement with the experiment than the KS results. In some cases, e.g. CoO and NiO, the improvement is substantial. Upon full relaxation of charged supercells, we found that for some oxides relaxation is small, while for other oxides, as NiO and CoO, we find substantial deviations due to polaron formation.

We now compare the CTLs results to calculations performed with the state-of-the-art screened hybrid functional for solids, HSE06.[16] We first observed that our calculations with HSE06 are generally close to those reported in ref. [72]. We see that in some cases such as FeO and MnO (direct gap), HSE06 performs better than PBE0 in reproducing the band gap, while a general tendency towards the overestimation can be observed. $HSE06_{DD}$ mitigates this tendency, but CoO and NiO, for instance, remain a critical case.

It should be noted, in this respect, that the results obtained with CTLs result are more robust over the whole series of magnetic insulators.

When we compare the results of the CTLs with other methods such as the GW approach, Table 8, we find a general good performance of CTLs. In particular, the gap computed with CTLs shows a comparable or even better performance compared to $G_0W_0$@HSE03, $G_0W_0$@HSE06, $GW^{RPA}$ or $GW^{LF}$ + $V_d$ calculations reported in the literature,[72,76,105,106] Table 8.

**Table 8.** Indirect ($E_g^i$, in eV) and direct ($E_g^d$, in eV) band gaps, from different theoretical approaches and experimental measurements.

| Method | MnO | | FeO | | CoO | | NiO | | CuO | | $Cu_2O$ |
|---|---|---|---|---|---|---|---|---|---|---|---|
| | $E_g^i$ | $E_g^d$ | $E_g^i$ | $E_g^d$ | $E_g^i$ | $E_g^d$ | $E_g^i$ | $E_g^d$ | $E_g^i$ | $E_g^d$ | $E_g^d$ |
| This work | | | | | | | | | | | |
| CTL | 3.52 | 3.64 | - | - | 2.66 | 2.71 | 3.79 | 4.17 | 2.15 | 2.55 | 2.55 |
| HSE06 | 3.19 | 3.87 | 2.16 | 2.43 | 3.99 | 4.02 | 4.83 | 5.72 | 2.78 | 3.63 | 2.30 |
| $HSE06_{DD}$ | 3.06 | 3.71 | - | - | 3.30 | 3.35 | 4.07 | 5.11 | 1.80 | 2.66 | 2.26 |
| Previous works | | | | | | | | | | | |
| HSE06[a] | 2.92 | 3.56 | 2.21 | 2.66 | 3.50 | 4.29 | 4.56 | 5.06 | - | - | - |
| HSE06[b] | 4.77 | - | 2.41 | - | 2.82 | - | 4.09 | - | - | - | - |
| HSE06[c] | - | - | - | - | - | - | - | - | 2.74 | 3.26 | 2.02 |
| $G_0W_0$@HSE03[d] | 3.4 | 4.0 | 2.2 | 2.3 | 3.4 | 4.5 | 4.7 | 5.2 | - | - | - |
| $G_0W_0$@HSE06[e] | - | - | - | - | - | - | - | - | 3.6 | 3.5 | - |
| $GW^{RPA}$ [f] | 3.81 | - | 1.65 | - | 3.23 | - | 4.28 | - | 2.49 | - | 1.59 |
| $GW^{LF}$ + $V_d$ [f] | 3.36 | - | 2.14 | - | 2.80 | - | 3.48 | - | 1.19 | - | 2.03 |
| Experiment | | | | | | | | | | | |
| PES+BIS | 3.9±0.4[g] | | | | 2.5±0.3[h] | | 4.3[i] | | 1.4-1.7[j] | | |
| XAS+XES | 4.1[k] | | | | 2.6[k] | | 4.0[k] | | | | |
| OA | | 3.6~3.8[l] | | 2.40[m] | | 2.7[n] | | 3.7[n]; 3.87[p] | | 1.44[o]; 1.57[q] | 2.17-2.62[r] |

See reference as: a[72], b[16], c[132], d,[105] e,[106] f,[76] g,[133] h,[134] i,[121] j,[135] k,[100] l,[136] m,[137] n,[122] o,[138] p,[123] q,[139] and r.[125]

Of course, the approach is not free from limitations. The most severe is that the results need to be checked versus cell size in order to obtain converged values. In this respect, the use of semilocal or short-range hybrid functionals could mitigate the problem. However, hybrid functionals represent a noticeable step forward with respect to the semilocal ones when one deals with localized states in a CTL approach.[87] In conclusion, the work done with CTLs provides an alternative approach for the determination of the band gap of magnetic insulators that goes beyond the KS approximation. Furthermore, the method allows an accurate description of the nature of the transition responsible for the excitation which is not always easy to obtain from the analysis of the DOS curves based on the KS levels.

## 3.2 Role of quantum confinement in group III-V semiconductor 2D nanostructures

This sub-chapter is focused on structural and electronic properties of bulk and (110) surfaces of the III-V semiconductors, for which the impact of system size to the band gap and band edges position were evaluated and rationalized. The sub-chapter is organized as follows. First, an introduction and the computational details of the simulation are reported. Next, a discussion arising from bulk materials and 2D slab models is given. In the last part a summary is given and a possible extension of the results to 3D confinement case are proposed (0D dimensionality).

### 3.2.1 Introduction

The importance of group III-V semiconductors cannot be underestimated due to their crucial technological applications, for instance as light-emitting diodes, infrared detectors, sensors, photocatalysts, etc.[140–146] Some of them have high electron mobility, comparable or even higher than Si, the standard material in microelectronics (e.g. GaAs has three times higher electron mobility than Si).[147] In addition, they are semi-insulating materials allowing their use as substrates in integrated circuits.[148] Group III-V semiconductors are also promising as photocatalysts because of their absorption edge in the visible light spectral region, due to a low band gap. When applied in photocatalysis, they are usually covered by oxides thin films, such as $TiO_2$. This process has a twofold purpose, *i*) the oxide protects the semiconductor from passivation; *ii*) recombination of photogenerated charge carriers is hindered, since electrons can migrate by tunnelling towards the oxide, and then to an active redox center,[149–156] similarly to what happens in oxide-oxide heterojunctions with a type II-alignment of the band edges.[31,37,157–160]

One of the most important and interesting properties of semiconductor nanostructures, including group III-V semiconductors, is related to quantum size effects.[161–163] The electronic properties (band gap and relative position of the band edges) of nano-objects such as quantum dots of group III-V materials exhibit strong size-dependence and a pronounced deviation from their bulk counterpart.[164–167]

---

The content of this sub-chapter is published in the Nanoscale Journal: L. A. Cipriano, G. Di Liberto, S. Tosoni, and G. Pacchioni, “Quantum Confinement in Group III-V Semiconductor 2D Nanostructures”, *Nanoscale*, 12 (2020) 17494-17501. https://doi.org/10.1039/D0NR03577G

This, however, does not hold true for all materials: some semiconductors are strongly affected, while others are almost insensitive. For instance, experimental evidences indicate that AlP, AlAs, AlSb are by far less affected by quantum confinement than InP, InAs, InSb.[168] Ga-based semiconductors are in an intermediate range. On one side this is a positive aspect, since it provides the possibility to rationally design dots with desired properties, on the other side it opens a fundamental question about the origin of this different behaviour.

In some cases the impact of quantum confinement is quite substantial, and the band gap of nanostructures can be more than twice the bulk one.[164,165,167,169–171] The deviation of the band gap from the bulk value ($\Delta E_g$) goes as $1/d^2$, where $d$ is the non-periodic dimension of the nanostructure.[168,172] For a perfect, ideal system, equations related to a particle in the box have been proposed,[173] where $\Delta E_g$ depends on both the size ($d$) and the effective mass of electrons ($m_e$*) and holes ($m_h$*) according to:[14,173]

$$\Delta E_g = \frac{h^2}{8kd^2}\left(\frac{1}{m_e^*}+\frac{1}{m_h^*}\right) \qquad \text{Eq. (9)}$$

One can have confinement in three dimensions, as in nanoparticles (0D system), or confinement in two-dimensions, as in quantum wires (1D system). Finally, the system can be confined in one-dimension as in quantum wells or 2D systems. The non-periodic dimension $d$ in Eq. (9) is defined as the diameter in quantum dots or nanoparticles, or as the thickness of 1D nanorods or 2D wells (slabs).[14] In this latter case, the confinement dimension is the non-crystallographic direction, i.e. that perpendicular to the selected plane.

In general, the coefficient $k$ depends on the dimensionality of the model. In the case of a three-dimensional confinement, as in an ideal spherical dot, the coefficient $k$ is equal to one.[173] For ideal quantum wires and quantum wells, $k$ is 1.71 and 2.00, respectively.[166,168,172] These values can be used to validate theoretical models describing the electronic properties of systems undergoing quantum size effects, as perfect spherical nanoparticles, quantum wires, or quantum 2D slabs, as shown by H. Yu, et al.[14]

As mentioned above, the rationalization of the electronic properties of group III-V semiconductors quantum dots is challenging, since the impact of quantum size effects can be very different, being negligible in some cases, and dominant in others.

From a theoretical point of view, this requires to adopt models that explicitly include quantum size effects in the simulation. Quantum dots, for instance, require to treat thousands of atoms with first principles approaches.

The goal of this chapter is twofold: first, the impact of quantum confinement in group III-V 2D semiconductor nanostructures was investigated and rationalized, providing new insight about the phenomenon. Second, a solid recipe for the study of this class of materials, based on simplified and computationally feasible models is provided. To achieve these purposes nine semiconductors have been studied (AlP, AlAs, AlSb, GaP, GaAs, GaSb, InP, InAs and InSb), by means of Density Functional Theory calculations where the exchange and correlation functional is described at the HSE06 level, a hybrid functional that has been shown to accurately reproduce bulk properties.[16,174–177] The focus is on two-dimensional slabs, and on the evolution of their properties with the slab thickness.

### 3.2.2 Computational details

Calculations have been performed at the level of Density Functional Theory, as implemented in CRYSTAL17 code.[92] The HSE06 screened-hybrid exchange and correlation functional has been chosen;[62,178] due to it represents a suitable choice for the treatment of semiconductor materials.[16,17] The gaussian-type orbitals basis set of each atom have been taken from Ref 174, and already used by Pernot et al. for this type of materials.[179]

The threshold criterion for energy convergence of each SCF cycle has been fixed to $10^{-7}$ atomic units (au). The truncation criteria for the coulomb and exchange integrals were set to $10^{-7}$, $10^{-7}$, $10^{-7}$, $10^{-7}$, and $10^{-14}$ au. The sampling of the reciprocal space was done in the Pack-Mokhorst scheme and was adapted to the cell size: we adopted a shrinking factor equal to 6 (16 points in the reciprocal space) for bulk calculations, and equal to 4 (9 points) for slab calculations. Geometry optimization include relaxation of both lattice parameters and ionic positions for bulk and slab calculations. The slab models were generated from the optimized bulk geometry. Band structures were determined at the fully optimized bulk cells by sampling 47 points in the reciprocal space. We choose to report the following path: Γ×X×W×L×Γ×K.[176,177]

### 3.2.3 Results

#### 3.2.3.1 Bulk

Group III-V materials investigated in this chapter have a cubic crystal structure, as in zinc blend.[180] They are all semiconductors with band gaps going from 0.24 eV to 2.51 eV.[147] Hybrid functionals[53,174,175,181] or high-level methods, such as GW,[177,182] are required to accurately reproduce both structural and electronic properties of these materials. Starting from the experimental crystal structures of AlP, AlAs, AlSb, GaP, GaAs, GaSb, InP, InAs, InSb we fully optimized the bulk geometries at the HSE06 level, given the good performance of this functional for the treatment of solids,[62,175] and particularly for this class of materials.[174] In Table 9, we report the computed lattice constant ($a$) and band gap ($E_g$) of each system.

First, we notice that the lattice constants are very close to the experimental values, with deviations below 1.5%. The computed band gaps are in agreement with previous theoretical reports.[174,176,177,183] Moreover, the overall accuracy estimated by the Mean Absolute Error (MAE) is 0.15 eV, in line with previous studies reported (0.12 eV) in the literature with HSE06.[174] As mentioned above, some systems, e.g. InAs and InSb, require particular care due to the very low band gap. If standard DFT approaches are used instead of hybrid functionals or high-level theories such as GW, these systems are incorrectly predicted to have metallic conductivity.[15,53,65,174,175,181,182,184,185]

It is worth mentioning that in the case of InP, InAs, and InSb, if Spin Orbit Coupling (SOC) effects are neglected, as in this work, this results in an overestimation of the band gap by about 0.1-0.2 eV.[176] In particular, it was shown that at HSE06 level, SOC leads to a reduction of the band gap towards the experimental values by 0.04 eV, 0.12 eV, and 0.26 eV for InP, InAs, and InSb, respectively.[176] In general, the band gaps of Al-based III-V semiconductors are the highest, being in the range 2.2-2.5 eV, in line with experiments.[147] In-based III-V semiconductors have an opposite behaviour, displaying overall the lowest band gaps. Ga-based materials do not show a specific behaviour in this respect, since GaP has a high gap, comparable to that of Al-based systems, GaAs has an intermediate gap,[147] and GaSb is a small-gap semiconductor, with band gap around 0.8 eV, Table 9.

**Table 9.** Calculated band gap ($E_g$, in eV) compared with experimental ones, and lattice constant (*a,* in Å) of AlP, AlAs, AlSb, GaP, GaAs, GaSb, InP, InAs, InSb.

| | $E_g$ / eV | | a / Å | |
|---|---|---|---|---|
| semiconductor | HSE06 | Exp | HSE06 | Exp |
| AlP | 2.52 | 2.51[a] | 5.4671 | 5.4510[b] |
| AlAs | 2.38 | 2.35[c] | 5.6741 | 5.6200[b] |
| AlSb | 2.19 | 2.39[a] | 6.1365 | 6.1347[b] |
| GaP | 2.46 | 2.35[d] | 5.4913 | 5.4505[b] |
| GaAs | 1.29 | 1.52[e] | 5.7070 | 5.6537[b] |
| GaSb | 0.80 | 0.81[f] | 6.1404 | 6.1180[b] |
| InP | 1.68 | 1.42[g] | 5.9128 | 5.8687[b] |
| InAs | 0.68 | 0.36[h] | 6.1247 | 6.0360[b] |
| InSb | 0.37 | 0.24[i] | 6.5316 | 6.4782[b] |

See references as: a[186,187], b[188], c[186,189], d[190], e[191], f[192], g[193], h[194], and i[195].

The effective masses of electrons ($m_e$*) and holes ($m_h$*) were evaluated from the band structure, Figure 11. Effective masses of each semiconductor have been calculated at the Γ point where the bands are parabolic and symmetric as is reported in literature and according to Eq. 10.[147,148,177,196–199]

$$\frac{1}{m^*} = \frac{1}{\hbar^2}\left|\frac{\partial^2 E}{\partial k^2}\right|_{\Gamma} \qquad \text{Eq. (10)}$$

$m_e$* and $m_h$* have been evaluated by looking at the curvatures of the bands corresponding to the Conduction Band Minimum (*CBM*), and Valence Band Maximum (*VBM*), respectively, Table 10. The curvature of the bands was fitted with a third-degree polynomial and a quadratic regression of this polynomial was performed. The calculated values are in line with literature ones; in particular, the hole effective mass is always higher than the electron's one. Furthermore, as for the band gaps, Al-based semiconductors have the highest electron effective mass, while In-based ones have the lowest one. Ga-based semiconductors span from high $m_e$* for GaP, comparable to that of AlAs and AlSb, to low $m_e$* as in the case of GaAs, and GaSb.

**Table 10.** Electron and hole effective masses at Γ point. Vales are reported in $m_0$ units, where $m_0$ is the free electron mass.

| | This work | | Previous Theoretical | | Experimental | |
|---|---|---|---|---|---|---|
| | $m_e^*$ | $m_h^*$ | $m_e^*$ | $m_h^*$ | $m_e^*$ | $m_h^*$ |
| AlP | 0.433 | 0.501 | 0.220[a]; 0.209[b] | 0.595[b] | --- | --- |
| AlAs | 0.151 | 0.439 | 0.150[a]; 0.149[b] | 0.510[b] | 0.150[a,c] | 0.472[a] |
| AlSb | 0.128 | 0.327 | 0.140[a]; 0.118$_b$ | 0.365[b] | 0.120[c] | 0.375[a] |
| GaP | 0.139 | 0.384 | 0.130[a]; 0.163[b] | 0.411[b] | 0.130[a,c] | 0.326[a] |
| GaAs | 0.059 | 0.346 | 0.067[d]; 0.076[b] | 0.314[d]; 0.355[b] | 0.067[a] | 0.350[a] |
| GaSb | 0.039 | 0.274 | 0.042[d]; 0.041[b] | 0.235[d]; 0.265[b] | 0.039[a] | 0.250[a] |
| InP | 0.098 | 0.423 | 0.085[d]; 0.094[b] | 0.479[d]; 0.450[b] | 0.080[a] | 0.531[a] |
| InAs | 0.039 | 0.376 | 0.027[d]; 0.029[b] | 0.343[d]; 0.373[b] | 0.026[a] | 0.333[a] |
| InSb | 0.025 | 0.312 | 0.017[d]; 0.018[b] | 0.245[d]; 0.263[b] | 0.014[a] | 0.263[a] |

See references as: a[147], b[198], c[148], and d[177]. The theoretical values in b are at the modified Becke-Johnson (MBJ) semilocal exchange level, while the values reported in d are at HSE06 level.

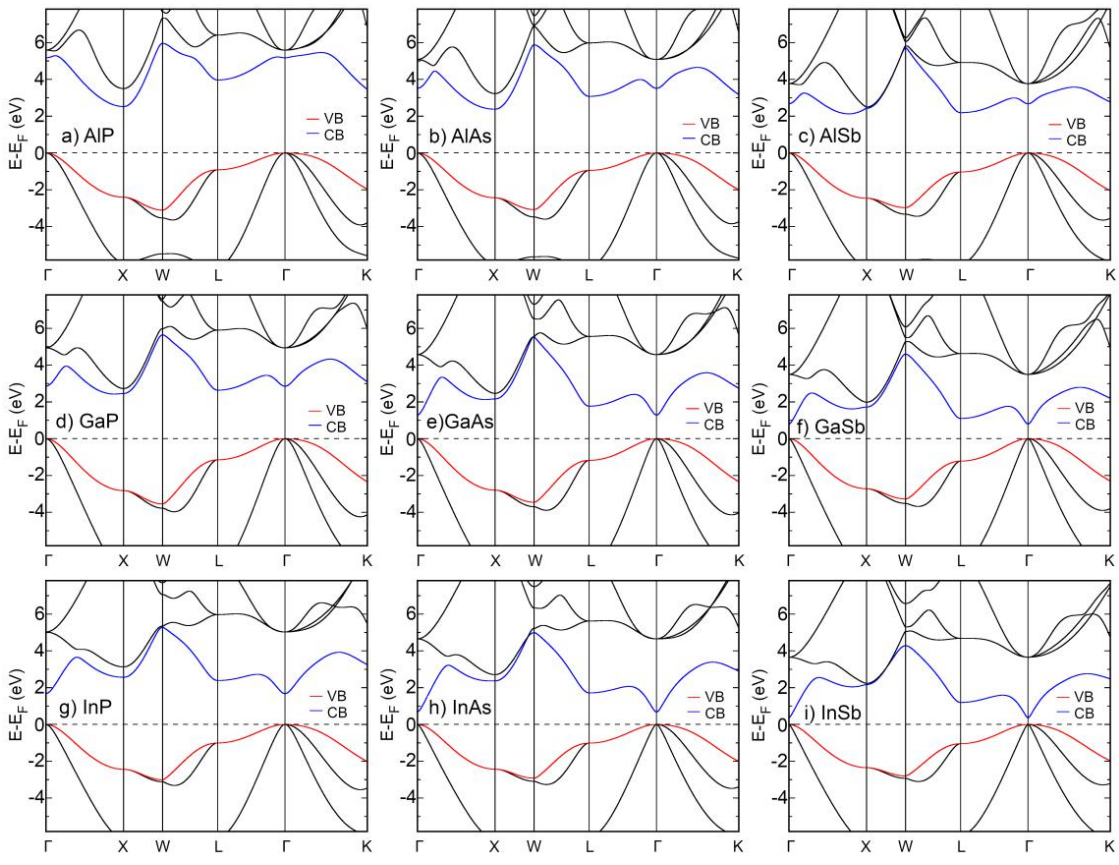


**Figure 11.** Band structure of group III-V semiconductors. a) AlP, b) AlAs, c) AlSb, d) GaP, e) GaAs, f) GaSb, g) InP, h) InAs, and i) InSb. Red lines represent the valence band (VB) and blue lines the conduction band (CB). The Fermi energy of each system has been set to 0 eV (dotted line). [200]

### 3.2.3.2 Surface

The most representative surfaces of cubic structures as the zinc blend for the III-V semiconductors are the (100) and (110) ones. The first one is polar and usually undergoes reconstruction.[201–210] The (110) surface is stable without reconstruction, and is widely studied.[201,204,208,211–220] Thus, the slabs terminated by the (110) surface were considered here. Each slab was designed from the optimized bulk structures, with an increasing thickness going from 0.5 nm to 10 nm, approximately - the exact values depend on the material. This corresponds to 2D films containing from 4 up to 40 atomic layers. In all cases was observed that the top layers of the optimized structures display some corrugation, where the electron-withdrawing atom (group V atom) moves slightly outward, and the group III atom moves inward from its atomic layer, see Figure 12.

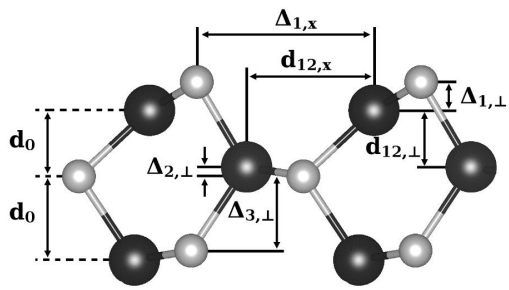


**Figure 12.** Surface termination of the relaxed (110) surfaces in the group III-V semiconductors. Black dots represent the III-group elements and grey dots the V-group elements. [200]

The results have been benchmarked against previous theoretical simulations,[214–218] suggesting that this effect comes from the need to compensate for the lower coordination of the surface atoms.[214,218] The extent of corrugation was checked with system size, and the surface corrugation remains constant for films thicker than 1.5 nm. This suggests that when comparing slabs of increasing thickness, the effect of corrugation is localized on the surface layers and will not affect quantities, as the band gap, reported below.

Figure 13, shows the trend of the band gap of the 2D semiconductors as a function of the slab thickness. In particular, is reported the band gap of the slabs ($E_g^{slab}$) normalized with respect to the bulk one ($E_g^{bulk}$), to better appreciate the deviation from the bulk behaviour. As expected, the band gap approaches the bulk's one by increasing the thickness of the 2D material from a few layers to a few dozens of layers. However, in some cases, see e.g. InP, InAs, InSb, GaAs, GaSb, the band gap becomes significantly larger than the bulk one for small thickness.

This is particularly clear for InAs and InSb, where the band gap for the 2D material is up to three times higher than for the 3D counterpart. For these systems, only when the thickness becomes larger than 6-8 nm the band gap approaches the bulk one. In contrast, AlP, AlAs, AlSb and GaP are much less affected and do not exhibit strong changes in band gap as the dimensionality of the slabs is reduced from 3D to 2D. A few atomic layers are enough to reproduce the bulk gap, see Figure 13. For this reason, the simulations of the III-V semiconductors were restricted to slabs of ~3.0 nm, as the properties are fully converged at this thickness. More details for each semiconductor can be found in the second section of the SI for the original paper, i.e., lattice parameters, band gap, surface energy and band edges of the (110) slabs of various thickness.[200]

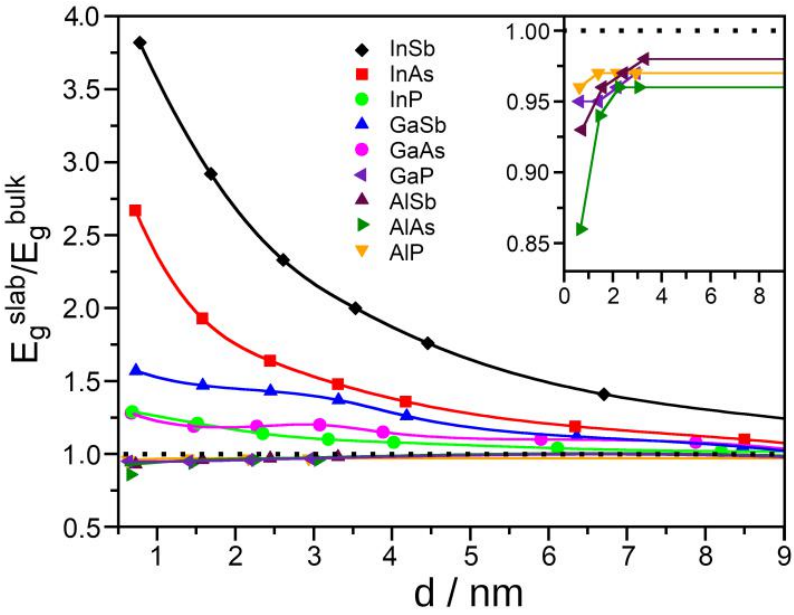


**Figure 13.** Computed band gap ($E_g^{slab}$) with respect to the bulk ($E_g^{bulk}$) for 2D slabs of III-V semiconductors as a function of the slab thickness. The inset reports a magnified region to appreciate the trend of systems that are nearly insensitive to the slab thickness. The horizontal dotted line is set at $E_g^{slab}/E_g^{bulk} = 1$. [200]

For materials where the band gap strongly changes from 3D to 2D, the question is the origin of this behaviour, which could be related to shifts in the valence band, in the conduction band, or both. To answer this question, in Figure 14 is plotted the position of *VBM* and *CBM* of the III-V semiconductors as a function of the slab thickness, see also Table 11. All values are referred to the vacuum level, set at 0 eV. In all cases, *VBM* and *CBM* converge to the corresponding bulk values by increasing the slab thickness, and the final values are reasonably close to the experimental data, Table 11, where MAE(*VBM*) = 0.25 eV, and MAE(*CBM*) = 0.22 eV.

This is an important result as it allows one to use the *VBM* and *CBM* positions to estimate the Ionization Potential (IP), IP = - *VBM*, and the Electron Affinity (EA) as EA = - *CBM*, for III-V 2D semiconductors and in general for III-V nanostructures.

**Table 11.** Calculated "bulk" Valence Band Maximum (*VBM,* in eV) and Conduction Band Minimum (*CBM*, in eV) of III-V semiconductors. Values (in eV) are taken from the thickest slab models considered in this work. The experimental values are taken from Ref. 147.

| | This work | | Experimental | |
|---|---|---|---|---|
| semiconductor | *VBM* / eV | *CBM* / eV | *VBM* / eV | *CBM* / eV |
| AlP | 6.21 | 3.75 | 6.18 | 3.66 |
| AlAs | 5.48 | 3.20 | 5.77 | 3.42 |
| AlSb | 4.59 | 2.45 | 4.85 | 2.46 |
| GaP | 5.59 | 3.22 | 5.71 | 3.36 |
| GaAs | 4.86 | 3.47 | 5.24 | 3.72 |
| GaSb | 4.10 | 3.26 | 4.47 | 3.66 |
| InP | 5.43 | 3.72 | 5.38 | 3.96 |
| InAs | 5.38 | 4.63 | 5.03 | 4.61 |
| InSb | 4.08 | 3.63 | 4.44 | 4.20 |

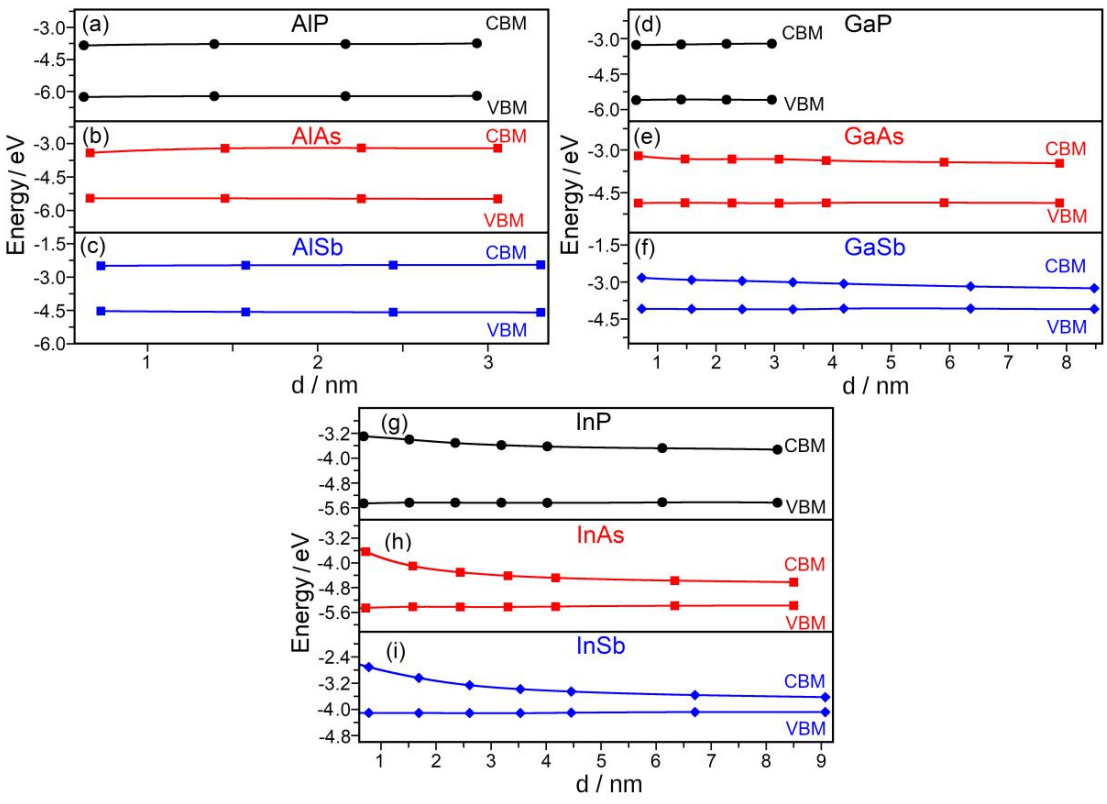


**Figure 14.** *VBM* and *CBM* as a function of the thickness in III-V semiconductors 2D slabs. (a) AlP, (b) AlAs, (c) AlSb, (d) GaP, (e) GaAs, (f) GaSb, (g) InP, (h) InAs, and (i) InSb. [200]

The first observation from Figure 14 is that the *VBM* of the III-V semiconductors is rather insensitive to nanostructuring hence to quantum confinement. On the other hand, the *CBM* changes significantly by reducing the thickness of the slabs, going from a 3D to a 2D regime.

This can be explained in light of the mobility of electrons and holes in the material. From Table 10 one can see that the hole effective mass is always considerably higher than the electron's one, suggesting that quantum size effects are not relevant for holes while they are important for electrons, Eq. 9.[147,148,177,198] As $m_e$* is smaller, higher is the impact on CBM, hence on the band gap. For instance, InSb has the lowest $m_e$*, followed by InAs, and indeed the *CBM* varies significantly by reducing the size of the slab. AlP, AlAs, AlSb have the highest electron effective mass (roughly 5-10 higher than that of InAs and InSb), and their *CBM* is almost constant, Figure 14. Then, according to Eq. 9, the behaviour of both band gap and *CBM* can be rationalized in term of electron's effective mass.

If the qualitative rationalization of the trend is clear, one can go a step further and try to provide a quantitative measure of the quantum confinement effect. To illustrate this, the In-based family of III-V semiconductors was considered, as these are showing the strongest dependence on reduction of the dimensionality. Defining $\Delta E_g$ as the deviation of the band gap in a given 2D system from the corresponding bulk reference, i.e. $\Delta E_g = E_g^{slab} - E_g^{bulk}$. Figure 15(a) shows the slab thickness corresponding to a given percentage deviation (from 5% to 20%) for some of the most confinement-sensitive materials (InSb, InAs, InP); Figure 15(b) shows $\Delta E_g$ against the slab thickness. As expected, InSb is more affected than InAs, that in turn is more sensitive than InP. In the case of InSb and InAs, the quantum confinement is very strong, and one needs films ~10 nm thick to converge the band gap within 5-10%, Figure 15(a). Then, the obtained data was fitted according to the equation of an ideal quantum well (Eq. 9), and was found an excellent agreement, as shown in Figure 15(b). The calculated average coefficient ($k_{avg}$) of Eq. (10) is 2.06, to be compared with the theoretical value 2.00 (Eq. 10). This result indirectly validates the idea of using slabs for the modelling of quantum wells.[14] This is an important result. In fact, since the 2D models of nanostructures follow precisely the equation for a quantum well, one can indirectly estimate the impact of quantum confinement for other nanostructures, such as quantum dots, without the need to explicitly calculate their electronic structures. In fact, from Eq. 9, it follows that given the systems effective mass and size *d*, the deviation from the bulk band gap ($\Delta E_g$) of a quantum dot is twice that of a quantum well. Stated differently, the slope of the curve for the quantum dot is twice that of a quantum well.

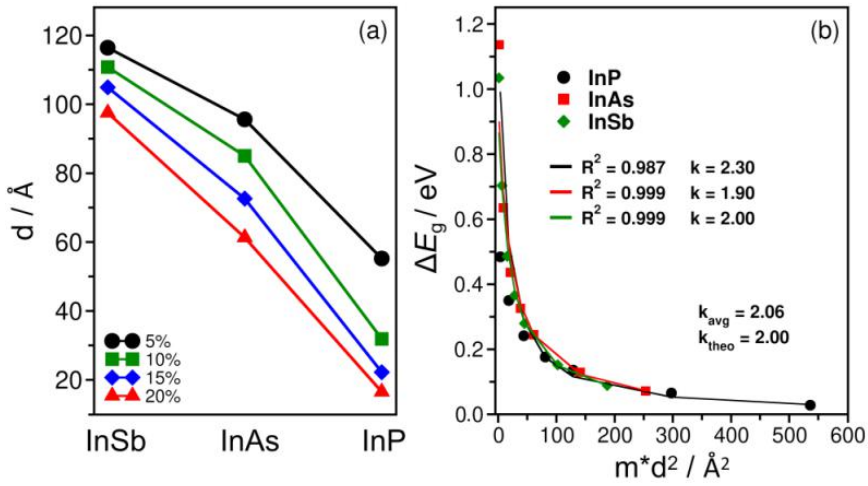


**Figure 15.** (a) Deviation (%) of band gap ($\Delta E_g$) from the bulk value for InSb, InAs, and InP 2D nanostructures: 5% (black), 10% (green), 15% (blue), and 20% (red), respectively. (b) band gap changes with respect to the bulk versus system size of InP (circles), InAs (squares), InSb (diamonds). On the x-axis is reported the square of system size times the effective mass (calculated from that of electron and hole) according with Eq. 9. Solid lines come from fitting curves as hyperboles. [200]

The concepts illustrated above have been used to predict the behaviour of the band gap in III-V semiconductor 2D slabs and 0D quantum dots. Figure 16 shows the trend of $\Delta E_g$ of the quantum wells simulated here (2D slabs) obtained upon electronic minimization at DFT/HSE06 ground state geometry, and of the corresponding quantum dots, compared with available experimental data. As was mentioned above, quantum dots values have been obtained recurring to Eq (9), where $k$ = 1 for 3D confinement (0D system), and $k$ = 2 for 1D confinement (2D system). Thus, the deviation from the bulk's gap for a 0D nanoparticle will be twice that observed for 2D wells, i.e. $E_g$ (0D) ≈ $\Delta E_g$ (2D) × 2.

Experimental data of InP, InAs, and InSb were taken from Refs [171] and [221–223]. These values have been already used in previous theoretical works. To name a few, the atomistic tight-binding[224,225] (TB) and the popular k·p approaches[226–228] were used to study InSb,[229] and the effective mass approximation (EMA)[173,230,231] for InP, and InAs.[232] Our model leads to robust quantitative predictions, Figure 16, comparable with the existing ones with different methods. It is important to stress that using this procedure relies only on 2D slabs calculations, which are computationally much less demanding than nanoparticles.

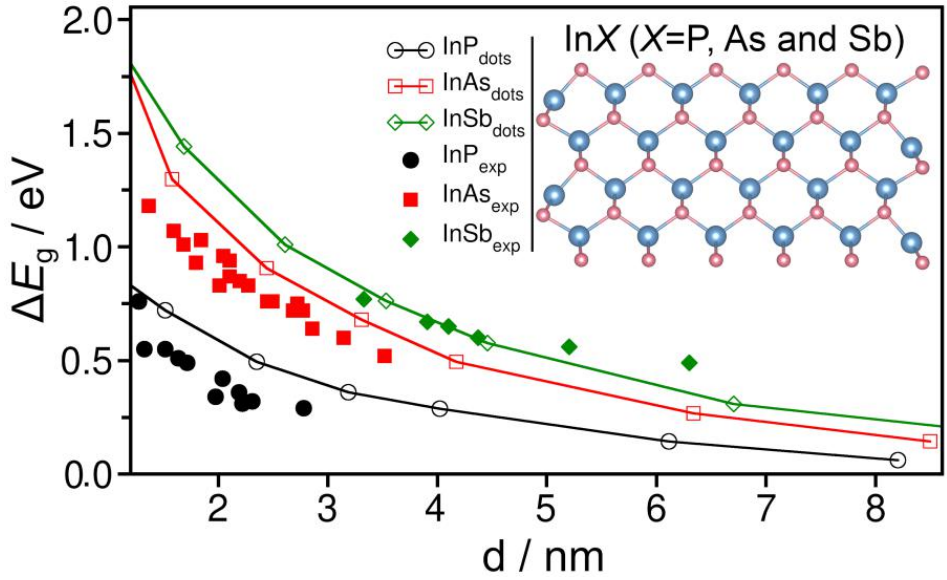


**Figure 16.** Deviation of the band gap in a given system from the corresponding bulk reference, $\Delta E_g$, as a function the size of the model. Solid lines with empty symbols are for 0D dots values calculated from slabs' ones (See main text). Solid circles, squares and diamonds are taken from experimental data.[171,221–223] Blue are for Indium and pink one for V-group elements. [200]

### 3.2.4 Summary

In this sub-chapter the properties of 2D nanostructures of group III-V semiconductors (AlP, AlAs, AlSb, GaP, GaAs, GaSb, InP, InAs, InSb) were investigated to evaluated the role of quantum confinement on the electronic structure, and particularly on the band gap. First, the structural and electronic properties of bulk structures at the DFT/HSE06 level were simulated, which allows one to reproduce accurately the lattice parameters, the band gaps, and the electron and hole effective masses of the bulk materials. Then, the study of 2D slabs have been done considering various thickness, going from ultrathin films, consisting of 4 atomic layers, up to slabs of 40 atomic layers, which fully reproduce the bulk properties. The study of the properties as a function of the film thickness provides a measure of the impact of quantum confinement, where InSb and InAs show that largest variation of the band gap by reducing the dimensionality, and are more sensitive to quantum size effects. On the other side, AlP, AlAs, AlSb and GaP are almost insensitive to nanostructuring. In particular, the conduction band edge is affected by the reduced dimensionality while the valence band is almost insensitive.

The observed trends, and the different response of InSb and InAs compared to the other III-V semiconductors, can be rationalized based on the different electron and hole effective masses, where the first term is dominant. This is corroborated by the fact that if one considers InP, InAs and InSb the computed properties can be predicted by an existing model for quantum wells and quantum dots, where the band gap deviation is proportional to the sum of the reciprocal of the electron and holes effective masses. This rationalization allowed to correctly reproduce the behaviour of InSb and InAs quantum dots without computing explicitly the electronic structure of these nanostructures, but using the results obtained on the 2D slabs. The agreement of the predicted data for 0D quantum dots with experiments is surprisingly good. This suggests that for nanostructures where quantum confinement effects play a role, it is possible to accurately reproduce the electronic properties, as band gap and band edges by simulating simple 2D slab models, rather than nanoparticles, which often are computationally significantly more demanding, or perhaps to predict the behaviour of 1D nanowires.

# Chapter IV: Heterojunctions

Electronic structure calculations provide a useful complement to experimental characterization tools in the atomic-scale design of semiconductor heterojunctions for photocatalysis. The band alignment of the heterojunction is of fundamental importance to achieve an efficient charge carriers separation, so as to reduce electron/hole recombination and improve photoactivity.

First, we describe an example of the type-II heterojunction following experimental observations and the idea that composite materials made by a low band gap semiconductor covered by a thin oxide layer are increasingly used in solar cells and photocatalysis.

In the second part some general considerations are discussed for the design and preparation of new interfaces with desired properties based of the important role of accurate electronic structure calculations.

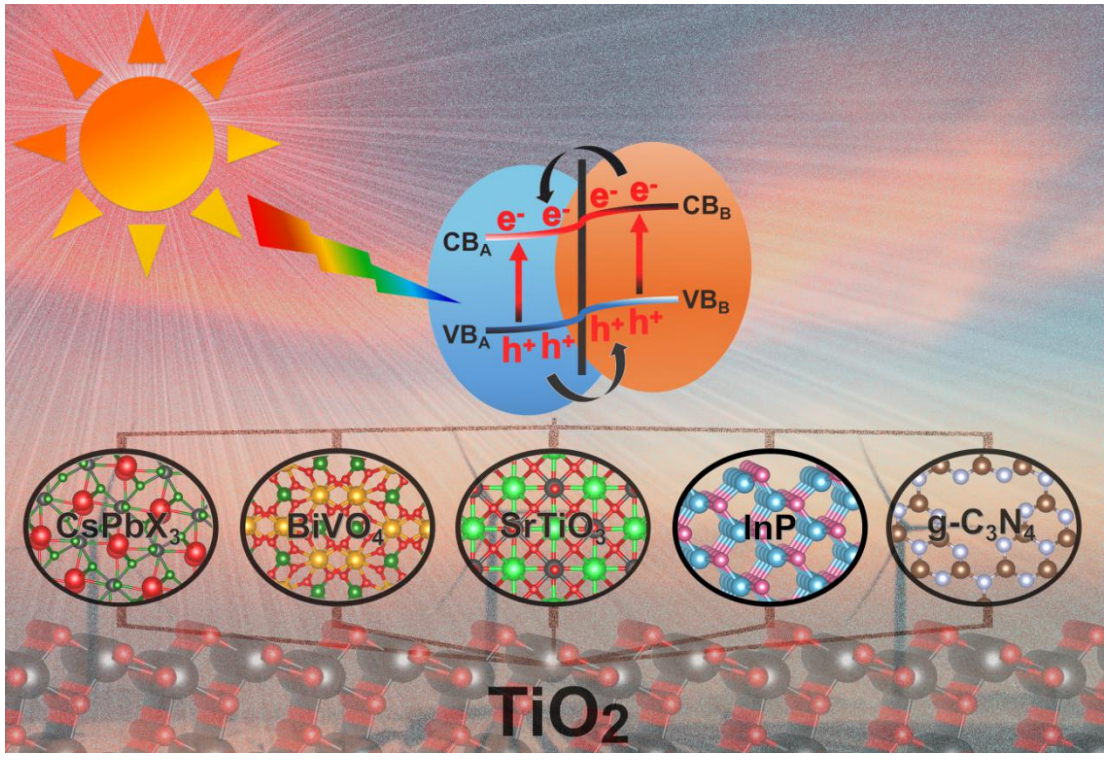

## 4.1 An example of type-II heterojunction: Structure and band alignment of InP photocatalysts passivated by $TiO_2$ thin films

This sub-chapter describes the nature of InP/$TiO_2$ heterojunction by means of Density Functional Theory calculations, showing that due to strong interface chemical bonds, the formation of a InP/$TiO_2$ junction is a favorable process.

The sub-chapter is organized as follows. First, an introduction about the uses of the InP/$TiO_2$ heterojunction is described and the computational details are provided. Third, the nature of different InP/$TiO_2$ interfaces, their stability and electronic nature are discussed. Next, the band alignment from the explicit models of the InP/$TiO_2$ interfaces considered are presented. In the penultimate section the thickness dependence of $TiO_2$ covering InP (thickness from 0.6 to 2.1 nm) is discussed and in the last part a summary is provided.

### 4.1.1 Introduction

The energy and environmental transition towards an efficient use of renewable sources implies, among others, the development of new semiconducting materials for photo-catalysis and environmental remediation. The aim is to develop efficient, cheap, and eco-friendly devices. $TiO_2$, one of the most studied oxides ever, is one of best candidates, mainly because of its versatility and low cost.[233–235] Unfortunately, the efficiency of bare $TiO_2$ is low because of its quite large band gap (3.2-3.4 eV), and fast electron-hole recombination. The first issue can be addressed by introducing in the lattice specific doping species, either metals and non-metals.[236–238] However, when charge carriers are generated by light absorption, the doping strategy does not hinder, and sometimes favors, their recombination often resulting in photo-catalytic systems less efficient than expected. To overcome this issue, heterojunction based materials offer a potential solution, since in many instances charge carriers recombination is reduced or slowed down, thanks to the opposite migration path of holes and electrons across the junction.[7,8,239]

---

The content of this sub-chapter is published in the Journal of Physical Chemistry C and Journal of Solid-State Electronics: L. A. Cipriano, G. Di Liberto, S. Tosoni, and G. Pacchioni, “Structure and band Alignment of InP Photocatalysts Passivated by $TiO_2$ Thin Film”, *J. Phys. Chem. C.*, 125, 21, (2021) 11620-11627. https://doi.org/10.1021/acs.jpcc.1c01666; L. A. Cipriano, G. Di Liberto, and S. Tosoni, “Computational Study of Group III-V Semiconductors and Their Interaction with Oxide Thin Films”, *Solid State Electronics*, 184 (2021) 108038. https://doi.org/10.1016/j.sse.2021.108038

The basic idea is that if the band edges of the two species are properly aligned, as in a so-called type-II junction, photo-excited electrons and holes will be energetically promoted in the two sides of the junction, thus reducing the probability of recombination. This results in a more efficient migration toward electrochemically active sites on the surface of the photocatalyst. Many examples of $TiO_2$-based heterojunctions have been reported, since this offers the possibility to take advantage of $TiO_2$ virtues, and at the same time to minimize the electron-hole recombination mechanism.[29,158,240–243] However, the problem due to low visible light absorption remains, if $TiO_2$ is the absorbing species.

For this reason, in the last few years several studies proposed to combine $TiO_2$ with small band gap materials, such as III-V semiconductors.[149–156,244–246] III-V semiconductors absorb a significant fraction of the solar light spectrum, thanks to their band gaps between 1.5 eV and 2.5 eV. However, these materials often are unstable in water or in contact with air, and they suffer from degradation and oxidative processes that alter their functionality. This is not the case of $TiO_2$, a stable and non-toxic material. The simple idea is that combining the two materials one can obtain a device with a strong light absorption power that, if covered by a protecting $TiO_2$ layer, can avoid the detrimental processes associated to degradation in air or humid environments.[149–156,244–246] Eventually, if the band edges are aligned according to a type-II junction, visible light photo-generated electrons on the semiconductor will be efficiently injected into $TiO_2$, and then towards the active redox sites on the surface.

In this context, the InP/$TiO_2$ (anatase) heterojunction has emerged as a promising candidate for photocatalysis and solar cells,[150,154] where anatase films of various thickness are grown on an InP support or nanoparticle. Experiments showed that: *i)* due to the InP low band gap, 1.42 eV, a relevant fraction of solar light can be harvested; and *ii)* photogenerated electrons can be efficiently promoted from InP to $TiO_2$.[155,247,248] In fact, InP/$TiO_2$ photo-cathodes displayed an enhanced activity compared to the separated components,[153] and InP/$TiO_2$-based solar cells reached up to 19.2% efficiency at the laboratory scale.[155] Moreover, InP/$TiO_2$ has been successfully used for $CO_2$ photoreduction; in this case it has been found that the optimal $TiO_2$ thickness is of about 3 nm.[154] Therefore, it is interesting to study this system at the atomistic level in order to unravel the physics behind InP/$TiO_2$ interfaces, with the hope to be able to contribute to the rational design of new devices with improved properties. In the present sub-chapter the study of InP/$TiO_2$ interface has three main goals: *i)* describe the atomistic nature of the interface in terms of chemical structure and stability; *ii)* determine from first principles the

effective band edges alignment of the heterojunction; *iii)* discuss the role of the $TiO_2$ film thickness for the efficiency of the heterojunction.

### 4.1.2 Computational details

The calculations have been performed at the level of Density Functional Theory (DFT), as implemented in the VASP 6.1.0 code.[96,97,249] The valence electrons, O (2s,2p), P (3s, 3p), Ti (3p, 4s, 3d), and In (5s, 5p), have been expanded into a set of plane waves with a kinetic cut-off of 400 eV, whereas the core electrons were treated with the Projector Augmented Wave (PAW) approach.[250,251] The hybrid exchange−correlation formulation proposed by Heyd, Scuseria and Ernzerhof (HSE06) was adopted,[178] since it provides accurate structural and electronic properties of both semiconductors and metal oxides.[16,17,174]
A conjugate-gradient algorithm was employed for geometry optimization of the direct interface.[252,253] The truncation criteria for electronic and ionic loops were set to $10^{-6}$ eV and $10^{-3}$ eV/Å, respectively. For the optimized bulk materials an 8×8×8 Monkhorst−Pack k-point grid was set,[254] and for slabs model we reduced the k-points sampling mesh to 4×4×1.

### 4.1.3 Nature of different InP and $TiO_2$ surfaces

The most stable surfaces of InP are the (100) and (110) ones. The first is polar and usually undergoes reconstruction,[201,203,206,208,255] while the (110) surface is stable, and does not reconstruct.[211–216,218,219] Thus, InP slabs terminated by the (110) surface were considered in this study.[200] As was described in the chapter above, InP form part of the III-V semiconductors, materials that present a quantum confinement effect.[200] In the chapter of role of quantum confinement in III-V semiconductors was found that a ~3 nm thick slab model is needed to guarantee fully converged electronic properties to the bulk on InP. To describe the properties of InP(110) surface, a 12 atomic layers thick model was considered (thickness ~2.4 nm), since it represents a good compromise between convergence to bulk properties, and computational feasibility. Indeed, the calculated band gap with a 12-layers slab, 1.51 eV, is only 0.06 eV higher than the bulk one, 1.45 eV. The surface energy to form this model, $E_s$ = 0.70 $Jm^{-2}$, is consistent with other values reported in the literature.[200]

In the case of anatase $TiO_2$, the most relevant surfaces are the (101) and (001) ones. As a first approximation to model a very thin $TiO_2$ passivating layer on the InP/$TiO_2$ interface, a thin films with both (101) and (001) surface terminations of thickness

around 0.6 nm and 0.8 nm were considered. The calculated band gaps of both thin surfaces are significantly higher than the bulk one, as a consequence of quantum size effects due to finite size of the model.[162,256,257] The calculated surface energy of $TiO_2$(101) is substantially lower than that of $TiO_2$(001), $E_s$ = 0.2 $Jm^{-2}$, an effect that can be attributed to the finite size of the films.[163,256,258] In Table 12 are reported the calculated lattice parameters (*a*, *b*, and γ, in Å and degrees - ◦ -), band gap ($E_g$, in eV), and surface energy ($E_s$, in $Jm^{-2}$) of the optimized $TiO_2$(101), $TiO_2$(001), and InP(110) 2D models used to construct the heterojunction.

**Table 12.** Lattice parameters (*a*, *b*, and γ) , band gap ($E_g$, in eV), and surface energy ($E_s$, in $Jm^{-2}$) of $TiO_2$(101), $TiO_2$(001), and InP(110) slabs.

| Model | Thickness / nm | a / Å | b / Å | γ / ° | $E_g$ / eV | $E_s$ / $Jm^{-2}$ |
|---|---|---|---|---|---|---|
| $TiO_2$(101) | 0.6 | 3.596 | 10.847 | 94.7 | 4.20 | 0.96 |
| $TiO_2$(001) | 0.8 | 3.685 | 3.685 | 90.0 | 3.78 | 1.21 |
| InP(110) | 2.4 | 4.198 | 5.958 | 90.0 | 1.51 | 0.70 |

### 4.1.4 Nature of different InP/$TiO_2$ heterojunction models

Starting from the relaxed surface structures of InP and $TiO_2$, were designed two models of InP/$TiO_2$ heterostructures, one where InP(110) is interfaced with $TiO_2$(101), and the second one where the contact involves the $TiO_2$(001) film. Designing a suitable model for an interface of two solid materials requires a super cell which minimizes the lattice mismatch, to avoid spurious strain-related effects.[259] This can be done by adopting large simulation cells, accounting for the non-epitaxial growth due to poorly matching lattices, or by finding the proper orientation that minimizes the lattice mismatch, and maximizes the chemical interaction at the interface. Here, was found a reasonable starting configuration for both InP/$TiO_2$ interfaces with good cation-anion matching, by placing $TiO_2$(101) and (001) thin films on a (1x1) InP(110) supercell rotated by 45°. Since in reality the $TiO_2$ thin film is grown to cover InP, the lattice parameters were fixed to those of InP, and in that way the strain is transferred to the $TiO_2$ phase, a usual procedure when simulating thin films supported on semiconductors.[260] This results in a tensile strain of 1.1% and 5.1% for *a* and *b* lattice vectors of the $TiO_2$(101) film, and 1.1% and 6.9% for the $TiO_2$ (001) ones. These are high strains, and therefore their impact on the $TiO_2$ electronic properties were checked, finding that the band gap deviations compared to the respective unstrained models of $TiO_2$(101) and (001) are of about 0.2 eV. The position of the VB and CB edges is not remarkably affected by the strain, either; the largest deviation with respect to the unstrained model is an increase of 0.29 eV reported for the conduction band minimum of $TiO_2$(101).

As will show in the next sup-chapters, uncertainties in this range do not affect the general conclusions, and in this respect the lattice strain can be considered acceptable.

Figure 17 shows the optimized structures of InP/$TiO_2$(101) and InP/$TiO_2$(001) interface models, where the formation of new chemical bonds at the interface were observed: In-O bonds display lengths in the range 2.27-2.31 Å, and the Ti-P ones are within 2.67 and 2.79 Å. These values are in line with the typical In-O and Ti-P distances in $In_2O_3$ (2.18 to 2.23 Å),[261] TiP (2.44 to 2.55 Å),[262] $Ti_5P_3$ and $Ti_3P$ (2.49 to 2.77 Å),[263] and $TiP_2$ compounds (2.51 to 2.74 Å).[264] This suggests that In-O and Ti-P bonds at the interface have a comparable strength to those of the corresponding binary compounds.

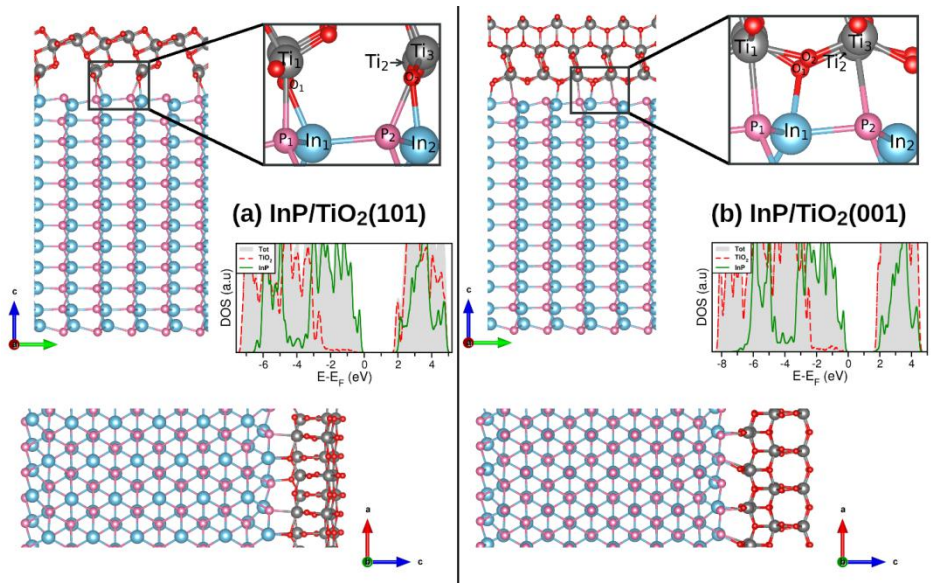


**Figure 17.** Side views of (a) InP/$TiO_2$(101) and (b) InP/$TiO_2$(001) explicit interfaces. The new-chemical bonds between InP and $TiO_2$ formed at the interface are shown in the insets. DOS of the systems are also reported: grey shaded area, total DOS; green line, InP; red dashed line, $TiO_2$. Atoms: Grey: Ti; red: O; pink: In; light blue: P. [265]

The interfacial energy ($E^{int}$), defined as the formation energy of the composite models with respect to the bulk materials, has been computed following Eq. 11:[34]

$$E^{int} = \frac{E_{(InP/TiO_2)} - N E_{bulk,TiO_2} - M E_{bulk,InP}}{2A} \qquad \textit{Eq. (11)}$$

$E_{(InP/TiO2)}$, $E_{bulk,TiO2}$ and $E_{bulk,InP}$ are the DFT total energies of the InP/$TiO_2$ interface, $TiO_2$ bulk, and InP bulk structures, respectively. *N* and *M* are the number of $TiO_2$ and InP formula units in the composite system, while *A* is the interface area.

The formation energy of the heterojunction, $E^{int}$, results from two steps: *(i)* the surfaces of InP and $TiO_2$ are cut from their respective bulk structures with an endothermic process (surface energy), and *(ii)* the interface is formed by putting them into contact (adhesion energy). The interfacial energies are 1.35 $Jm^{-2}$ for InP(110)/$TiO_2$(101) and 1.80 $Jm^{-2}$ for InP(110)/$TiO_2$(001). In addition, the calculated adhesion energy is -0.75 $Jm^{-2}$ for InP(110)/$TiO_2$(101) and -0.65 $Jm^{-2}$ for InP(110)/$TiO_2$(001), indicating that the formation of both interfaces is thermodynamically a favorable process. Furthermore, the adhesion of InP(110) with $TiO_2$(101) is 0.1 $Jm^{-2}$ larger than with $TiO_2$(001). By comparing these data with the surface energies reported in Table 12, one can also evaluate the energy cost of straining the titania film to form the interface. Cutting an InP(110) from the bulk costs 0.70 $Jm^{-2}$ (Table 12). Cutting an unstrained $TiO_2$(101) surface from the bulk, in turn, has a cost of 0.96 $Jm^{-2}$ (Table 12). Thus, the creation of the unstrained, separated components of the interface implies a cost of 1.66 $Jm^{-2}$. By subtracting the adhesion energy from the interfacial energy, one obtains the formation energy of the strained, separated components, which is, for InP(110) and $TiO_2$(101), 2.10 $Jm^{-2}$. Straining the $TiO_2$(101) film, thus, has a cost of 0.44 $Jm^{-2}$. One can consistently calculate the cost of straining the $TiO_2$(001) film, which results as large as 0.54 $Jm^{-2}$. Interestingly, the energy gain when forming the interface (adhesion energy) is in both cases higher that the energy cost to strain the $TiO_2$ units. This leads to an overall energy gain to form the interface when compared to separated surfaces.

### 4.1.5 Charge transfer and band alignment

The charge transfer across the interface by considering the atomic charge distribution layer by layer was analyzed by means of the Quantum Theory of Atoms in Molecules (QTAIM).[266–270] Charge polarization effects are mainly localized at the contact region, and they rapidly disappear by moving away from the interface, see Figure 18. Even if atomic charges are far for providing a quantitative estimate of the charge transfer,[271–273] they suggest that the interaction at the contact region between InP and $TiO_2$ has mainly a covalent character, in line with what found in the structural analysis where the formation of short, direct bonds has been observed. This is further corroborated by the analysis of the charge density difference plots, calculated as $\rho_{InP/TiO2} - (\rho_{InP} + \rho_{TiO2})$, where $\rho_{InP/TiO2}$ is the charge density of the composite, and $\rho_{InP}$, $\rho_{TiO2}$ those of the composing units, Figure 18. The plots clearly show that upon formation of the interface, there is an accumulation of charge between the Ti-P and the In-O atoms, a typical indication of a covalent character of the bonding.

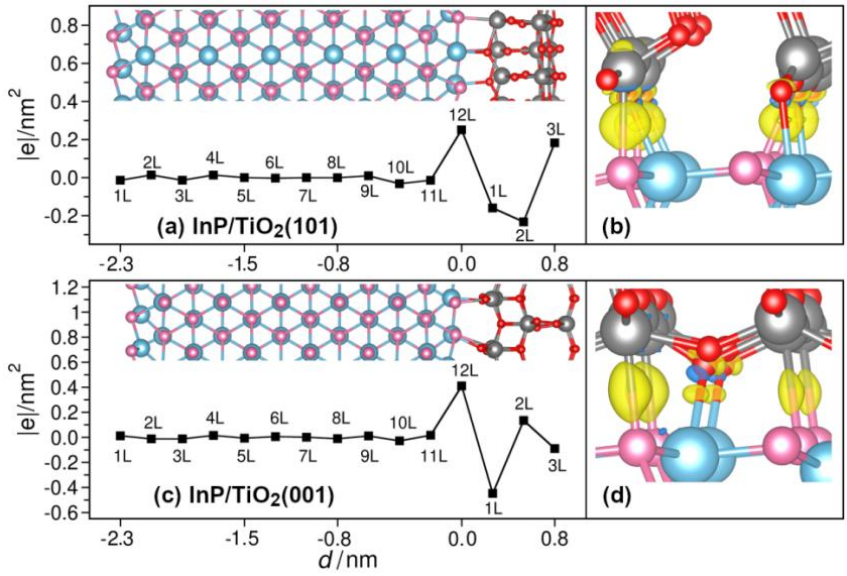


**Figure 18.** (a) calculated atomic charge (normalized with respect to the surface area) of each crystallographic layer in InP/$TiO_2$(101) interface model; (b) charge density difference plot (Dr), where charge accumulation regions are in yellow, and depletion ones in blue. Panels (c) and (d) are the same but for the InP/$TiO_2$(001) interface. [265]

Moving to the electronic properties, and in particular the band alignment, first by looking simply at the density of states (DOS) for a qualitative description. Figures 17(a) and 17(b) also report the DOS of InP/$TiO_2$(101) and InP/$TiO_2$(001) interface models projected on the two composing units. In both cases the main contribution to the Valence Band Maximum (VBM) is due to InP, while the Conduction Band Minimum (CBM) is predominantly projected onto $TiO_2$, despite a significant hybridization. Even though the analysis of the DOS allows one to get an idea of the band alignment, it cannot provide a quantitative description because of hybridization effects. The relative position of the band edges can be estimated accurately by aligning the VBM and CBM of the separated components by using as a common reference the core level binding energies, e.g. the $O_{1s}$ and $P_{2p}$ orbital energies, similarly to what is done in XPS experiments.[35–37,274–278] The convergence of the VBM and CBM values with the inner shells of the core levels was carefully checked and the Conduction Band Offset (CBO) and Valence Band Offset (VBO) were computed by using equations 12 and 13.

$$E_{CBO} = [(E_{CBM} - E_{P_{2p}})_{InP} - (E_{CBM} - E_{O_{1s}})_{TiO_2}] + (E_{P_{2p}} - E_{O_{1s}})_{InP/TiO_2} \quad \text{Eq. (12)}$$

$$E_{VBO} = [(E_{VBM} - E_{P_{2p}})_{InP} - (E_{VBM} - E_{O_{1s}})_{TiO_2}] + (E_{P_{2p}} - E_{O_{1s}})_{InP/TiO_2} \quad \text{Eq. (13)}$$

For InP/$TiO_2$(101) the computed Conduction Band Offset (CBO) is 0.17 eV, while the Valence Band Offset (VBO) is 2.75 eV, indicating that the band edges of InP are higher in energy than those of $TiO_2$. In the case of InP/$TiO_2$(001), CBO and VBO are 0.10 eV and 2.60 eV, respectively. These values are close to those obtained from the DOS curves. This is an important result, since it shows that InP/$TiO_2$ is always expected to behave as type-II heterojunction, irrespective of the anatase facet involved in the junction, (001) or (101), and of the method used to obtain the alignment, thus providing a first principles rationalization of the experimental findings,[153–155] see Figure 19.

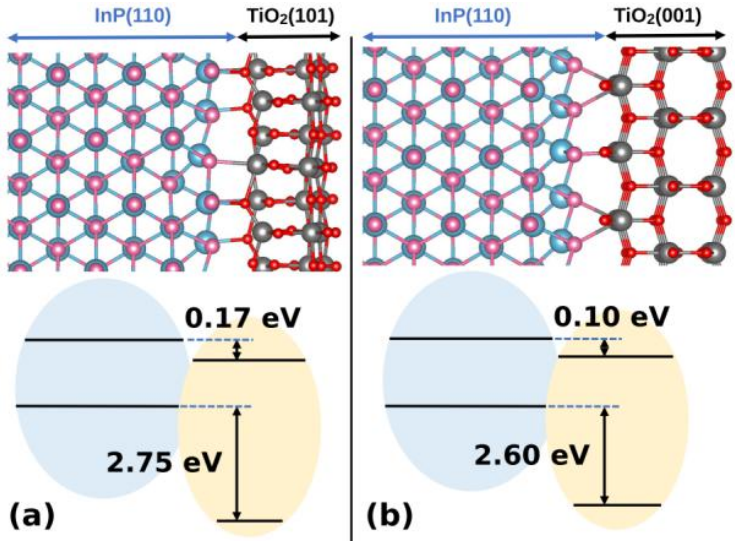


**Figure 19.** Band alignment of (a) the InP/$TiO_2$(101) and (b) the InP/$TiO_2$(001) heterojunction models. Grey: Ti; red: O; pink: In; light blue: P. [265]

### 4.1.6 Effect of the $TiO_2$ film thickness in the InP/$TiO_2$ interface

As the $TiO_2$(101) film allow to obtain the most stable InP/$TiO_2$ interface, here is described the role played by the $TiO_2$(101) film thickness from about 0.6 nm to ~2 nm in thickness. This is a regime where electron tunneling can dominate over classical charge carrier diffusion in an insulating material.[279] In general, the probability of tunneling rapidly decreases with the thickness of a potential barrier. On the other hand, the band edges of the film can change going from ultrathin to thin layers, until they converge to typical bulk values. In this respect, the band alignment affects the potential barrier for charge carrier transfer. So, to address this aspect, InP/$TiO_2$ interfaces with $TiO_2$(101) thickness of 0.6 nm, 1.3 nm and 2.1 nm were simulated. The structural analysis indicates that by increasing the $TiO_2$(101) thickness from 0.6 nm to 2.1 nm, the structural properties of the interface do not exhibit significant changes. The interface energy ($E^{int}$) goes from 1.35 J/$m^2$ (0.6 nm

film) to 1.06 J/m$^2$ (1.3 nm film) and 1.14 J/m$^2$ (2.1 nm film), reflecting the initial decrease in the $TiO_2$ (101) surface energy as a function of the slab thickness.

While the nature of the valence and conduction bands does not vary with film thickness, the $TiO_2$ band gaps decreases by increasing the thickness, until it approaches the bulk's value, indicating that quantum confinement effects vanish rapidly with the size of the $TiO_2$ layer.[256] Indeed, the $TiO_2$(101) band gap goes from 4.20 eV (0.6 nm), to 4.11 eV (1.3 nm), and 3.85 eV (2.1 nm). Thus, while the $TiO_2$ thickness does not affect the band edges alignment, Figure 20, being InP/$TiO_2$ always a type-II junction, it affects the band offsets. Both *VBO* and *CBO* increase with the thickness of the coating film, as reported in Figure 20. However, while going from 0.6 nm to 1.3 nm-thick films the increase is significant both for VBO (0.53 eV) and CBO (0.26 eV), a further increase in thickness up to 2.1 nm affects significantly only the CBO (0.21 eV), while the VBO (0.03 eV) seems almost converged. However, significant changes in the band offset by further increasing the thickness are not expected, because a 2.1 nm anatase slab displays a band gap value almost converged to the bulk one. This result provides further support to the conclusion that the properties of the system are reasonably converged with anatase films of more than 2 nm thickness.

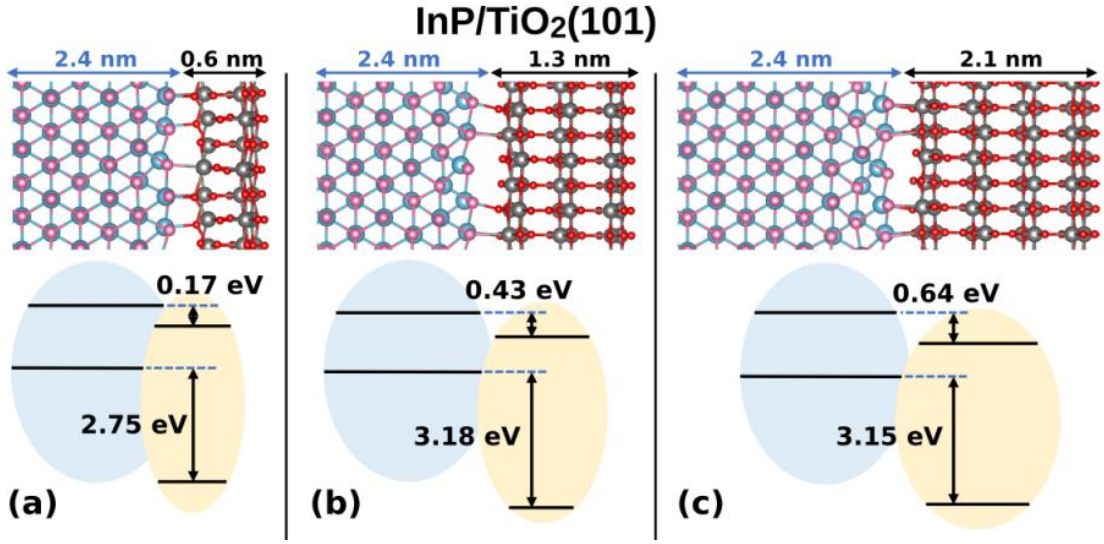


**Figure 20.** Band alignment of the InP/$TiO_2$(101) heterojunction with different $TiO_2$ thickness: (a) 0.6 nm; (b) 1.3 nm; and (c) 2.1 nm. Grey: Ti; red: O; pink: In; light blue: P. [265]

So far, the discussion is based on the band structure of the ground state of the system. However, photoexcitation implies the generation of an electron-hole pair, and it is an exited state problem. To address, this aspect the coexistence of one electron and one hole in the system was simulated. This is done by computing the lowest triplet configuration, which provides a reasonable approximation to the real excited state which corresponds to a singlet open shell configuration.[280]

As the nature of the valence and conduction bands does not vary with film thickness, the triplet configuration for the InP/$TiO_2$ heterojunction was study with $TiO_2$(101) film 1.3 nm thick, which is an intermediate thickness and implies less computational demand. Figure 21 shows that a vertical excitation from the ground state structure results in a delocalized solution where the hole is shared by several P atoms, and the photo-generated electron is distributed over few Ti and In atoms. This excited state is 1.9 eV above in energy than the ground state, thus compatible with the photo-excitation of InP under visible light. This process is followed by an atomic relaxation with polaron formation. If the atomic coordinates are relaxed, a localized solution with one electron localized on a Ti atom of $TiO_2$ and the corresponding hole on a P atom of InP is found, i.e., on the two sides of the interface. The atomic relaxation leads to a non-radiative decay with an energy gain of 1.3 eV, Figure 21. Interestingly, the charges migration and electron-hole localization follow what predicted by the band alignment picture. Therefore, this result corroborates and validates the prediction obtained based on ground state properties.

### 4.1.7 kinetics effects

Although they are not include explicitly in this study, since this requires the simulation of excited states dynamics,[281,282] some qualitative correlation between our results and the expected performances of the devices in terms of efficiency of carriers' migration can be done. This is based on the analysis of the carriers' effective mass, calculated from the curvature of the band structure of InP and $TiO_2$.[200] The electron mobility in InP is quite high, as can be evinced by the low effective mass ($m_e^*$), 0.10 (DFT) and 0.08 (experimental).[147] The results of the first principles calculations show that *i)* high electrons' mobility in InP, and *ii)* the energetically favorable migration towards $TiO_2$ are beneficial for electrons' injection from InP into $TiO_2$, and this prediction is in line to what experimentally observed: the electrons' transfer efficiency in InP/$TiO_2$ may reach up to 85%.[248] Then, when electrons migrate into the $TiO_2$ unit, their mobility strongly decreases, as shows also by the calculated $m_e^*$ of 1.05 (DFT), to be compared with the experimental one ~0.4-1.[283,284] This explains why the efficiency of InP/$TiO_2$ devices deteriorates when the $TiO_2$ film thickness increases, as reported by Zeng et al.[154] In particular, they showed that the efficiency of InP/$TiO_2$ improves when the $TiO_2$ coating reaches ~3 nm, whereas the insulating character of $TiO_2$ prevails at higher thicknesses. If the latter regime can be easily understood in the light of carriers' mobility in $TiO_2$, when the $TiO_2$ thickness is small quantum tunneling prevails over classical diffusion,[279] and the probability of electrons transfer should decrease rapidly with the thickness.

This contradiction can be explained by taking into consideration the fact that the overall potential well is determined by the band edges alignment, and, as reported above, the conduction band offset increases with the thickness of the $TiO_2$ film from 0.6 nm to 2.1 nm, thus favoring the electron transfer process.

Overall, the calculations show that not only the InP/$TiO_2$ system is described as a type-II junction, irrespective of the $TiO_2$ surface in contact with InP, but, most importantly, the behavior is retained by increasing the size of the passivating anatase film, providing a theoretical rationalization of the beneficial spatial separation of photogenerated carriers under visible light in titania-coated semiconducting nanoparticles.[150,153,155] Last, based on the band edges alignments, was possible to predict that increasing the $TiO_2$ thickness from 0.6 nm to 2.1 nm is beneficial for carrier's separation, because a larger band offset implies a stronger thermodynamic drive for photoelectrons' migration from InP to $TiO_2$. This in a regime where electron migration from InP to the surface of the $TiO_2$ component is not affected by the detrimental insulating character of $TiO_2$, which is expected to become dominant at larger thicknesses.[154] This conclusion is consistent with recent experiments showing improved photocatalytic efficiency of InP/$TiO_2$ photocatalysts by increasing the $TiO_2$ film thickness from less than 1 nm up to an optimal value of about 3 nm.[154]

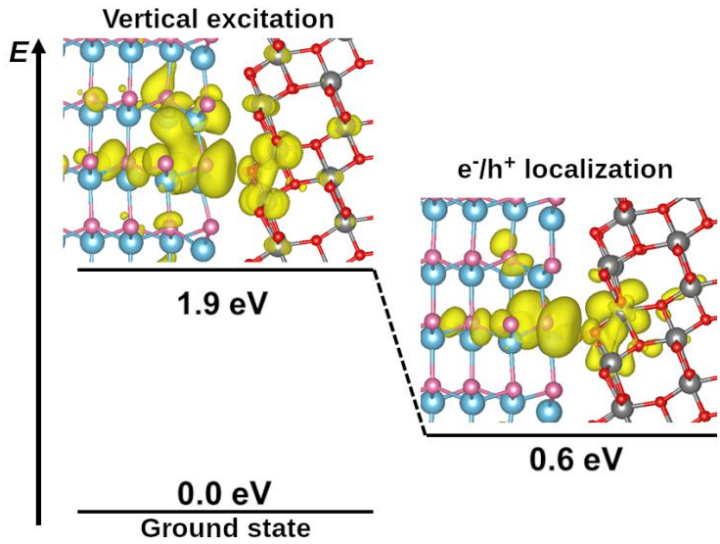


**Figure 21.** Energetics of electron and hole generation in the InP/$TiO_2$(101) heterojunction, where the $TiO_2$ film thickness is 1.3 nm. The vertical excitation has a cost of 1.9 eV, compatible with the photoexcitation of InP. The localization of a hole on InP and an electron on $TiO_2$ (polaron formation) leads to an energy gain of 1.3 eV and stabilizes the excited state. Spin density isosurfaces at 0.0005 e/$A^3$ are reported. Grey: Ti; red: O; pink: In; light blue: P. [265]

### 4.1.8 Summary

Two different InP/$TiO_2$ interfaces made by InP(110) converged slabs with ultrathin $TiO_2$ films of ~0.6-0.8 nm thickness exposing both (101) and (001) surfaces were modellated. These simulations allow to found that irrespective of the $TiO_2$ surface, the formation of a InP/$TiO_2$ junction is a favorable process, characterized by the formation of new covalent In-O and Ti-P interface bonds. Where the InP/$TiO_2$(101) interface is more stable than the InP/$TiO_2$(001) one. The band edges alignment is consistent with a type-II junction, where $TiO_2$ band edges are lower in energy than the InP ones. This will favor the migration of photogenerated electrons from InP to $TiO_2$, consistently with the experimental observation.

By studying the role of the $TiO_2$ film thickness, it was found that the system always behaves a type-II junction, but the increase in the band offset observed for thicker films implies that the thermodynamic gain for carrier's migration increases with the $TiO_2$ thickness up to about 2 nm. These results provide a first principles rationalization of experiments showing that InP/$TiO_2$ outperforms the separated components, in particular if the coating titania layer is thicker than 2 nm.

## 4.2 Rational design of binary and ternary semiconductor heterojunctions for photocatalysis

As was already mentioned, the band alignment of the heterojunction is of fundamental importance to achieve an efficient charge carriers separation, so as to reduce electron/hole recombination and improve photoactivity. In this sub-chapter we report some examples that addressed methodological aspects that need to be consider in the design of binary and ternary semiconductor heterojunctions and how these are determined at the level of density functional theory (DFT).

The sub-chapter is organized as follows. First, a short introduction and the description of the computational details is given. Next, some considerations that need to be address in the design of heterojunctions for specific examples of the type-II heterojunctions and the ternary heterojunctions is discussed. Last, some general recommendations are given.

### 4.2.1 Introduction

The applications of heterojunctions in photocatalysis cover various aspects of modern life.[285–293] As was already mentioned in the introduction, the key requirements for the design of an efficient photocatalyst are (1) a good visible light absorption, (2) a favorable position of the edges of the valence and conduction bands (VB and CB) with respect to target redox species, (3) an efficient charge carriers separation upon excitation, (4) a high mobility and low recombination rate of the charge carriers, and last but not least (5) a good chemical stability.[37,294–300] Composite materials in which two or more units are in intimate contact thanks to the formation of a junction region can in principle successfully address all these aspects.[7,8] In the photocatalysis process the Type-II heterojunction shows the best challenges, this is because when the band edges are positioned according to a Type-II alignment, the photogenerated electrons and holes migrate towards different components of the heterojunction, hindering recombination and enhancing the efficiency of the redox processes.

---

The content of this sub-chapter is published in the Chemistry -A European Journal: G. Di Liberto, L. A. Cipriano, S. Tosoni, and G. Pacchioni, “Rational Design of Semiconductor Heterojunctions for Photocatalysis”, *Chem. A. Euro. J.*, 27, (2021) 13306-13317. https://doi.org/10.1002/chem.202101764

Sometimes the advantage of creating a heterojunction consists in the possibility to protect a chemically unstable low-band gap semiconductor by coating it with a corrosion resistant thin oxide film as was shown in the last chapter and in another works;[150–152,301] this can lead to a visible-light active and chemically stable photocatalyst.

The possibility to engineer and design interfaces between different semiconductors opens in principle a variety of systems to investigate. In doing this, one has to take into account a number of parameters, such as the choice of the surface terminations that are interfaced, the nature of the chemical bonds, the occurrence of a charge transfer at the interface, the possibility to growth nanofilms exploiting quantum confinement effects, etc. An important role in this context is played by electronic structure calculations based on Density Functional Theory (DFT). In this sub-chapter the systems that will be discussed have been selected based on their relevance for practical applications, on the existence of experimental results showing the possibility to construct the junctions, and in order to identify specific effects that determine the final behavior of the junction. Which gives the possibility to discuss the underlying physical principles behind semiconductor heterojunctions for photocatalysis, and to show how is it possible to conceive new atomic-scale interfaces and predict their performances.

### 4.2.2 Computational details

Most of the systems discussed is this sub-chapter have been studied using the CRYSTAL code[92,302]; for a few cases the VASP periodic code has been used.[96,97,249]

### 4.2.3 Examples of Heterojunctions

#### 4.2.3.1 Type-II heterojunctions: joining different semiconductors

Here are presented four cases of Type-II heterojunctions as described by DFT calculations. In the first three cases anatase $TiO_2$ is interfaced with various semiconductors: halide perovskites;[303] ternary compounds such as $BiVO_4$ and $SrTiO_3$;[243,304] and in the last example $BiVO_4$ is interfaced with $WO_3$.[305]

##### 4.2.3.1.1 $TiO_2/CsPbX_3$

In this example the role of surface termination was considered. Over the past few years there have been a growing interest towards organic-inorganic halide perovskites, $ABX_3$, where A is an organic cation or an alkali metal cation, B an

inorganic cation, and X is the halogen.[306–310] These materials find application in solar cells, light emitting diodes, photocatalysis, etc.[311–317] $CsPbX_3$ perovskites have been used in combination with oxide films, such as $TiO_2$, that protect them from chemical attack[314,318–322] and provide a Type-II alignment of the band edges.[294,303,309,323] The most relevant polymorphs of $CsPbX_3$ materials are the cubic (a) and orthorhombic (g) phases.[308,310,324] Using the CRYSTAL code and the HSE06 functional the properties of α-$CsPbX_3$ (X= Cl, Br, I) 2D nanostructures have been studied.[325]

The (001) surface of α-$CsPbX_3$ (X = Cl, Br, I) 2D nanostructures has two main terminations, $PbX_2$- and CsX-, while the (110) one is characterized by three terminations, X, Cs, or PbX. This offers a great variability in designing the junction with $TiO_2$. The $PbX_2$-terminated slabs have band edges lower in energy than the CsX-terminated ones, but their stability is similar. In the case of the (110) surface, X-termination displays the lowest surface energy. Since the corresponding band edges are in closer agreement with the experiment, it is likely that this is the termination of (110) surfaces in real samples. Taking the most stable terminations, the band edges of the (110) slabs are always below those of the (001) ones, so that it is possible in principle to take advantage of this feature to design systems that induce charge carriers separation. Using the independent units method, without explicitly simulating the interface, a qualitative estimate of the band alignment in $CsPbX_3/TiO_2$ has been obtained, showing a Type-II alignment for all three perovskites, Figure 22.

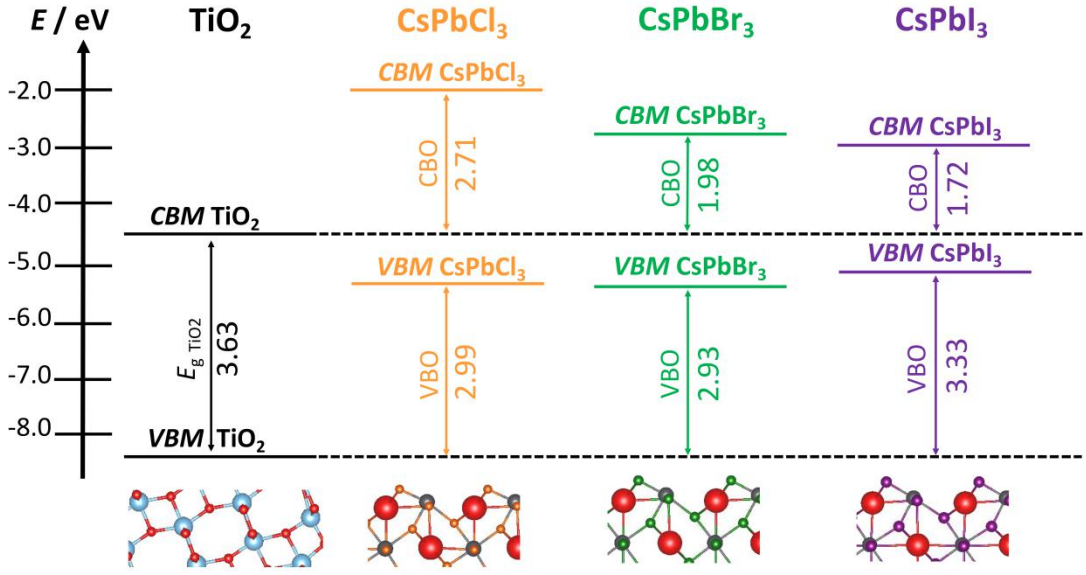


**Figure 22.** Band edges offset of $CsPbX_3$(110) and $TiO_2$(101) moieties in $CsPbX_3/TiO_2$ heterojunctions (DFT/HSE06 results). [9]

This example shows the importance of the selection of the proper facet to construct the heterojunction, a result that has been obtained without the explicit consideration of the interface.

#### 4.2.3.1.2 $TiO_2/BiVO_4$

$TiO_2/BiVO_4$ is a highly active system in photocatalytic water splitting.[326,327] This example was used to discuss the role of slab thickness and surface termination - CRYSTAL calculations with HSE06 and $PBE0_{DD}$ functionals.[328] As is reporter in Ref 96, slabs of about 2 nm thickness for both $TiO_2$(101) and $BiVO_4$(010) components, Figure 23, showed converged structural and electronic properties, with a marginal effect of the choice of the functional. However, using thinner slabs results in considerably shifted VBM and CBM values, Figure 23, showing the importance to check-out the converged electronic and structural properties with respect to slab thickness.

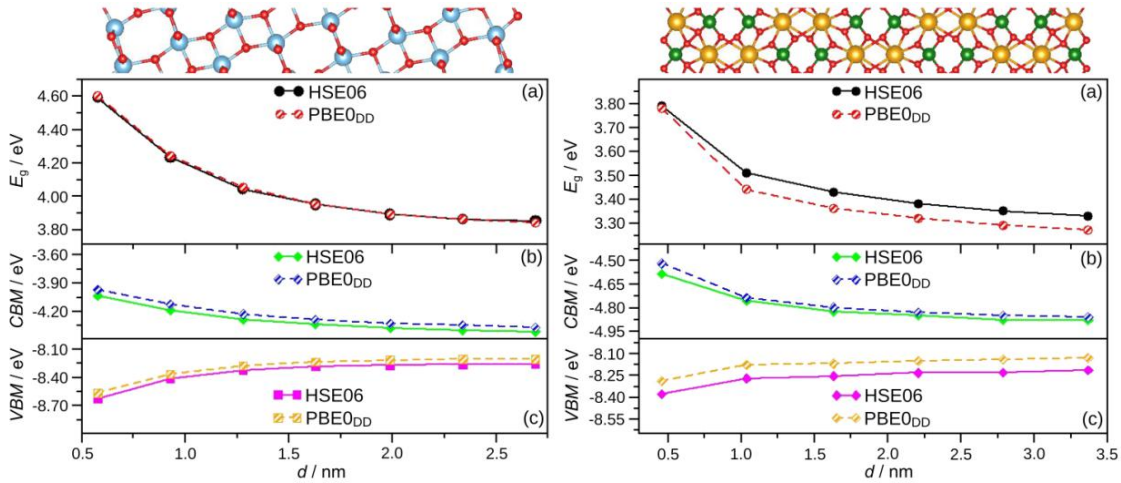


**Figure 23.** Left: $TiO_2$(101); right: $BiVO_4$(010). (a) band gap ($E_g$), (b) Conduction Band Minimum (*CBM*), and (c) Valence Band Maximum (*VBM*). [9]

Also with this example, the band edges of the independent units (no explicit interface) were used to analyze the type of alignment in $TiO_2/BiVO_4$ comparing two $BiVO_4$ surfaces, (010) and (110). If $TiO_2$(101) is interfaced with the $BiVO_4$(010) surface the alignment is of Type-I, and the offset of the VB is negligible, Figure 24, thus reducing the driving force for the separation of the charge carriers. On the contrary, $TiO_2$(101)/$BiVO_4$(110) is a Type-II heterojunction, where the band edges of $BiVO_4$ are higher in energy that those of $TiO_2$. Therefore, the $TiO_2$(101)/$BiVO_4$(110) interface outperforms the $TiO_2$(101)/$BiVO_4$(010) one showing once more the importance of the surface termination.

This prediction, consistent with the experimental observations,[304] is obtained with the simple approach of the "independent units" but is nevertheless useful to assess the nature of the junction and represents a case of facet engineering.

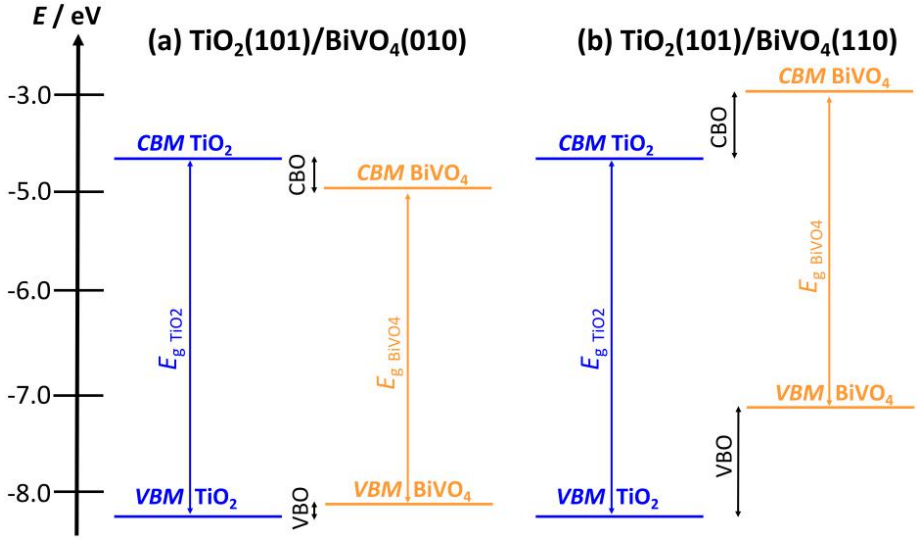


**Figure 24.** (a) Type-I band alignment of $TiO_2$(101)/$BiVO_4$(010); (b) Type-II band alignment of $TiO_2$(101)/$BiVO_4$(110) (HSE06 results). [9]

#### 4.2.3.1.3 $TiO_2$/$SrTiO_3$

The third example, is the interface of anatase $TiO_2$(001) with $SrTiO_3$(001). Differently from the previous two cases, here an explicit interface was constructed (CRYSTAL calculations, $PBE0_{DD}$ functional).[278] $TiO_2$/$SrTiO_3$ represents an archetype of nearly-epitaxial matching between the two materials, due to the favorable lattice mismatch between the (001) surfaces of the two semiconductors which minimizes the strain.[243,329] However, two surface terminations are possible for $SrTiO_3$, SrO and $TiO_2$ termination, giving rise to two different interface models.

The band alignment has been obtained using (a) the independent units and (b) the surface terminated junction models, Figure 25. In both cases a Type-II heterojunction is predicted, and the band offsets differ by about 0.1 eV only. Furthermore, the calculated offsets are fully consistent with the experimental ones.[243] This example shows that the use of independent units, without explicit description of the interface, can be used in selected cases to predict the band alignment. However, as shown below, this does not hold true in presence of relevant polarization or charge transfer at the interface.

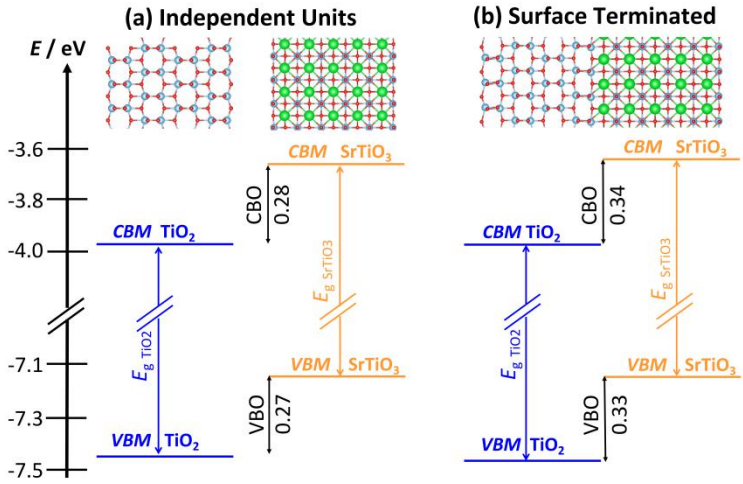


**Figure 25.** Band alignment for the $TiO_2$(001)/$SrTiO_3$(001) heterojunction, where $SrTiO_3$ is terminated with a $TiO_2$ layer. (a) independent units; (b) surface terminated junction models (explicit interface). Blue: $TiO_2$; orange: $SrTiO_3$. [9]

The impact of oxygen vacancies ($O_v$) was also considered in this example, as they are commonly present.[242,330] $O_v$ on $TiO_2$ or in the contact region slightly decrease the offsets by 0.0–0.1 eV, while $O_v$ on the $SrTiO_3$ side (less stable) lead to an increase of the offsets. In general, the presence of oxygen vacancies has only a moderate impact on the band alignment of the $TiO_2$/$SrTiO_3$ junction.

#### 4.2.3.1.4 $WO_3$/$BiVO_4$

The last example of heterojunction made of two different components is $WO_3$/$BiVO_4$. Photoanodes based on the $WO_3$/$BiVO_4$ heterojunction showed excellent solar-to-hydrogen conversion efficiency in water splitting.[305,331–333] This is thanks to the visible light absorption of $BiVO_4$ combined with the high electron conductivity of $WO_3$. The nature of $WO_3$/$BiVO_4$ has been investigated with the aim to study the nature of charge transfer at the interface (CRYSTAL code, $PBE0_{DD}$ and HSE06 functionals).[334] Recent experimental results confirm that the (010) surface of $BiVO_4$ is involved in the junction with $WO_3$.[335] A $WO_3$ slab of 1.6 nm thickness exhibits converged properties while for $BiVO_4$ 2 nm films are required to recover the bulk properties. The band alignment predicted by considering the separate units is qualitatively the same obtained simulating the explicit interface (surface terminated junction approach).

The role of charge polarization in this interface has been considered. This is an important aspect that should always been discussed, besides the position of the band edges.

In fact, the band alignment determines the preferred direction of the photogenerated electrons and holes based on pure thermodynamic arguments; however, the creation of a large interface dipole due to the occurrence of a charge transfer may favor or disfavor charge carriers migration.[336,337] In the case of $WO_3$/$BiVO_4$ the charge polarization at the interface is beneficial for charge separation since there is a charge accumulation on the $BiVO_4$ side on the interface and a consequent charge depletion at the opposite side. This effect, together with the band alignment, explains the superior photoactivity of this heterojunction. A model limited to the separate units would not account for this phenomenon.

#### 4.2.3.2 Type-II heterojunctions: joining different facets of the same semiconductor

A Type-II junction can be created also by joining differ surface terminations of the same semiconductor;[29,338–340] in this case one generates a "surface junction".[7] Here two examples are mentioned, one is the $BiOIO_3$(010)/$BiOIO_3$(100) interface, and the second one involves the combination of two titania anatase facets, $TiO_2$(001)/$TiO_2$(101).

##### 4.2.3.2.1 $BiOIO_3$(010)/$BiOIO_3$(100)

$BiOIO_3$ nanocrystals exposing (010) and (100) surfaces are excellent photocatalysts.[340] However, if one considers the position of the VB and CB of the (010) and (100) surfaces of $BiOIO_3$ one cannot explain the experimental trends. In fact, calculations done at the $PBE0_{DD}$ level with the CRYSTAL code show unambiguously that the most stable (010) and (100) surfaces of $BiOIO_3$ exhibit VBM and CBM positions which are inverted compared to experiment.[341] To reconcile theory with experiment, it is necessary to invoke the formation of a junction between a less stable (010) surface termination of $BiOIO_3$ with the most stable (100) one. When this is done new chemical bonds at the interface result in a thermodynamically stable system and a significant charge polarization at the interface. This junction not only provides the correct band alignment, but also exhibits a position of the energy levels that is fully consistent with the experiment, Figure 26. This example shows that to rationalize the behavior of semiconductor heterojunctions it is important to describe the formation of explicit interfaces with atomistic precision, and to take into account the overall thermodynamic stability of the system, and not only the most stable surface terminations. This is a typical example where it is necessary to employ the "alternating slabs junction" or the "surface terminated junction" approaches.

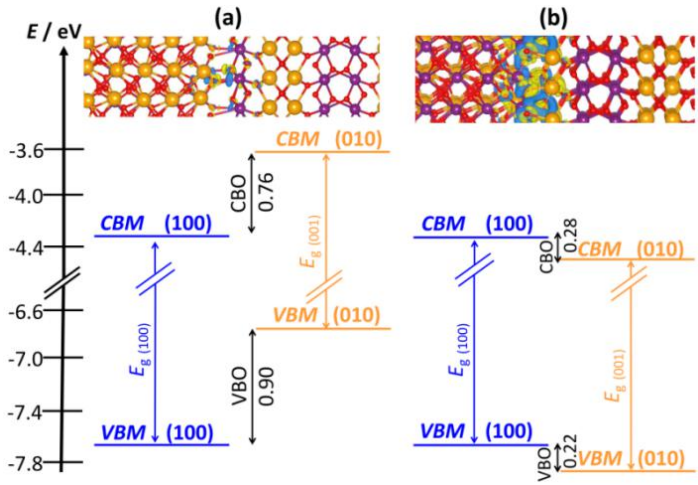


**Figure 26.** Band alignment in $BiOIO_3$(100)/$BiOIO_3$(010) (a) interface built from the most stable $BiOIO_3$(100) and $BiOIO_3$(010) surface terminations; (b) interface build from the most stable $BiOIO_3$(100) surface and the less stable $BiOIO_3$(010) termination. Only this latter model explains the observed band alignment of the $BiOIO_3$(100)/$BiOIO_3$(010) heterojunction. [9]

#### 4.2.3.2.2 $TiO_2$(001)/$TiO_2$(101)

This case represents the most common example of junction formed by interfacing two polymorphs of the same material, Degussa P25,[342] a mixture of anatase (75%) and rutile (25%) widely used to benchmark the photocatalytic efficiency of new materials. An heterostructure formed by combining the (101) and (001) facets of anatase $TiO_2$ provides interesting photocatalytic properties, even better than the reference P25,[29,338,343–345] and has been studied with the CRYSTAL code and PBE0[60] and $PBE0_{DD}$ functionals. Two models have been used, the simple "independent units" approach and that based on "surface terminated junctions". A two-step process was followed in order to design a realistic model of the heterojunction. The superposition of (101) and (001) anatase facets leads to unacceptable strains and poor Ti-O match at the interface. Thus, a superlattice was created by rotating the two surfaces by an angle of ~45°, so that the lattice strain is considerably reduced (6.3% and 0.9%) and a good cation-anion match in the contact region is achieved.

The resulting band alignment, obtained by considering electronic states on inner layers, is of Type-II, Figure 27, and is predicted also by the independent units model.[158,277] The picture provided by the band alignment was assessed by simulating the explicit formation of a hole in the VB and of an electron in the CB according to a singlet-triplet excitation process.[280] The vertical excitation was followed by a structural relaxation that leads to hole and electron localization and polaron

formation.[346–348] The generation of charge carriers upon photon absorption starts at the (001) surface with formation of delocalized holes in the VB and electrons in the CB. The structural relaxation induces hole localization on a single O ion on the (001) side of the junction and migration of the excited electron to the (101) side, where it localizes to form a $Ti^{3+}$ ion, as shown by the spin density plots, Figure 27. Of course, this process can be studied only when the effect of the interface is explicitly included in the model.

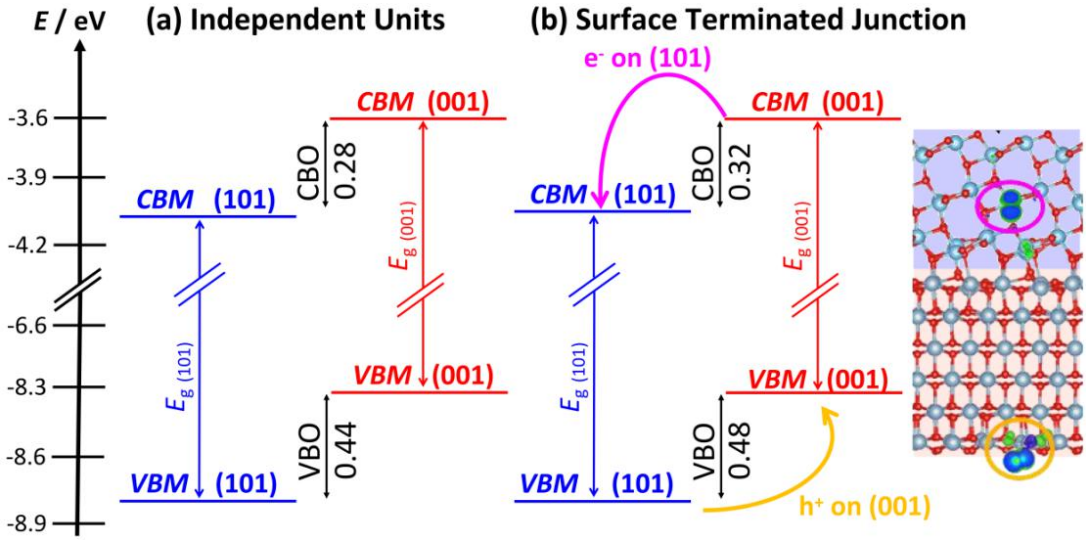


**Figure 27.** Band alignment of (001)-(101) anatase surface junction (PBE0 results). [9]

The effect of Nitrogen doping on the properties of the $TiO_2$(001)/$TiO_2$(101) junction have been also addressed.[160] While doping of oxide semiconductors has been addressed in several studies, much less attention has been dedicated to the combined effect of doping and formation of heterojunctions. The effect of N-doping on anatase and rutile $TiO_2$ has been studied extensively by some of us.[237,349–352] The presence of isolated N-dopants results in localized defect states just above the VB of the material, thus increasing the absorption in the visible region of the spectrum. N-dopants also favour the formation of O vacancies.

In a recent study, Sun et al. synthetized a junction formed by N-doped (001)-(101) anatase $TiO_2$ surfaces.[344] The new photocatalyst exhibits higher photoactivity under visible light with respect to the undoped samples, suggesting that the two main strategies to improve $TiO_2$ performances (heterostructure and doping) can also work in a concerted way. A systematic analysis shows that both substitutional and interstitial N-dopants localize preferentially at the interface. At higher dopant concentrations, also doping of the inner layers becomes energetically accessible.

The band alignment picture however is not strongly altered by the presence of the N-impurities. This provides a solid theoretical basis for the experimental observation that the N-dopants are not detrimental for photocatalysis, while they increase the visible-light absorption capability. This is true also when the presence of the N-dopants is combined with O vacancies, commonly present in real samples. The excess electrons associated to the O vacancy ($Ti^{3+}$ $3d^1$) states are spontaneously transferred to the low-lying N-states, causing a remarkable decrease of the O vacancy formation energy. Despite these compensating mechanisms and internal charge transfers, the overall band alignment in N-$TiO_2$(001)/N-$TiO_2$(101) remains the same of the undoped junction.

#### 4.2.3.3 Ternary heterojunctions

In this section two examples of heterojunctions formed by three components are discussed. In the first one, $TiO_2$/$TiO_2$/ZnS, a Type-II heterojunction is supposed to increase the efficiency due to a cascade process. In the second example, $C_3N_4$/$SrTiO_3$/$TiO_2$, the inclusion of a $SrTiO_3$ buffer layer between $C_3N_4$ and $TiO_2$ results in an inversion of the charge polarization at the interface and in a completely different behavior, from Type-II in $C_3N_4$/$TiO_2$ to Z-scheme in $C_3N_4$/$SrTiO_3$/$TiO_2$.

##### 4.2.3.3.1 $TiO_2$/$TiO_2$/ZnS

As was described above, the anatase (101)-(001) junction exhibits an efficient charge separation; where the (101) side stabilizes the photogenerated electrons and the (001) side the photogenerated holes. An even better separation of charge carriers could be achieved adding a third component with higher hole-stabilizing capability, such as a ZnS(110) layer grown on the anatase (001) surface. This results in a ternary $TiO_2$/$TiO_2$/ZnS composite, investigated with the CRYSTAL code and the PBE0 functional.[277] New Zn-O and Ti-S bonds form at the interface between $TiO_2$ and ZnS giving rise to non-negligible structural reconstruction, also beyond the interfacial region.

The formation of a ternary compound has some effect on the band offsets. The computed band alignment is consistent with the experimental evidence,[353] i.e. the ternary $TiO_2$/$TiO_2$/ZnS heterojunction promotes a charge carriers' cascade. This has been confirmed by an explicit simulation of a photoexcited electron-hole pair, which shows electron localization on the $TiO_2$ side and hole formation on the ZnS side of the junction. However, the analysis of the band alignment alone is not sufficient to conclude on the direction and efficiency of charge carriers' migration.

The excitation of one electron from the VB to the CB (triplet state) results in a full localization of the electron on a $Ti^{3+}$ ion of $TiO_2$(001) and of the hole on a S site of the ZnS(110) surface, with formation of two polarons spatially separated by about 0.8 nm, Figure 28. The following step consists in localizing the electron on the $TiO_2$(101) moiety, as predicted by the band alignment. However, this step implies a penalty of 0.8 eV due to Coulombic forces hindering the electron-hole spatial separation. In this respect, the $TiO_2/TiO_2/ZnS$ junction is predicted to have good photoactivity, but not to overperform the $TiO_2/TiO_2$ one. Coulomb forces act against the separation of charge carriers predicted based on the relative energy of the band edges. This highlights the necessity of explicitly including structural and electronic junction's effects, as well as charge carriers' localization. Complex semiconductor architectures made by three or more units may exhibit effects that cannot be predicted by a simple inspection of the band edges of the system.

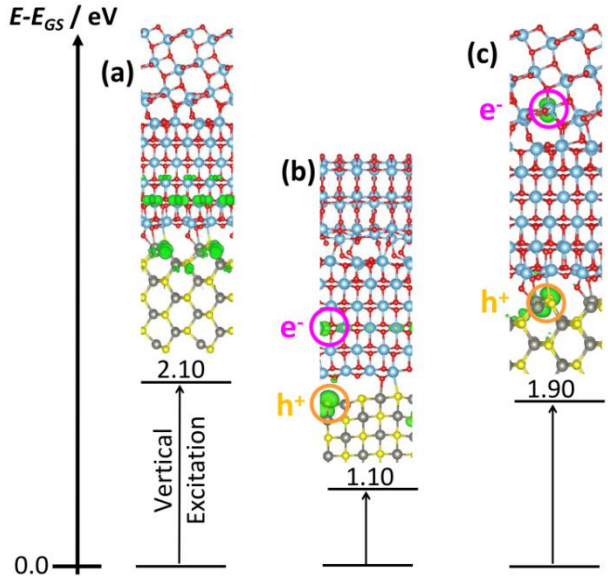


**Figure 28.** Triplet excited configurations in $TiO_2/TiO_2/ZnS$. (a) vertical excitation; (b) a relaxed configuration where $h^+$ is localized on ZnS(110) and $e^-$ on $TiO_2$(001) (two polarons). (c) a relaxed configuration where $h^+$ is localized on ZnS(110) and $e^-$ in on $TiO_2$(101). Spin density iso-surfaces at 0.003 $|e^-|/a_0^3$ are shown in green. Light blue: Ti; red: O; yellow: S; grey: Zn. [9]

#### 4.2.3.3.2 $C_3N_4/SrTiO_3/TiO_2$

The last case considered also shows that the simple inspection of the band alignment to predict the charge carriers separation may not be sufficient. This is the case of graphitic carbon nitride, g-$C_3N_4$,[354–357] a material which has attracted a lot of attention due to a high visible-light activity, chemical stability, and facile synthesis.

Beside these positive aspects, the activity of g-$C_3N_4$ is deteriorated by a fast recombination of charge carriers,[356] a problem that can be mitigated by creating a g-$C_3N_4$/$TiO_2$ (anatase) interface.[358–361] Experimentally it has been shown that the $TiO_2$ band edges are lower in energy than those of g-$C_3N_4$;[7,336,337,359] accordingly, g-$C_3N_4$/$TiO_2$ should behave as a Type-II junction. On the contrary, photogenerated electrons and holes in g-$C_3N_4$/$TiO_2$ follow a different migration scheme, referred to as direct Z-scheme.[7,337,362] Differently from a Type-II junction where electrons and holes migrate towards the energetically most favourable component, Figure 29(a-b), a different transport mechanism occurs in direct Z-scheme photocatalysts. Here the photogenerated electrons on side A, with lower CB, recombine with the holes photogenerated on semiconductor B with a higher VB. In this way the photogenerated electrons in B and holes in A can be preserved, Figure 29(c-d). Coherently with this scheme, in g-$C_3N_4$/$TiO_2$ electrons do not migrate from g-$C_3N_4$ to $TiO_2$, as expected for a Type-II junction, and are retained on g-$C_3N_4$. At the same time, holes do not migrate from $TiO_2$ to g-$C_3N_4$, but they tend to stay on the oxide. This change in behaviour from Type-II to direct Z-scheme in g-$C_3N_4$/$TiO_2$ is due to an important effect: the generation of an interface dipole that determines a bend bending which prevents the flow of charge carriers as predicted by the Type-II alignment, Figure 29.[337]

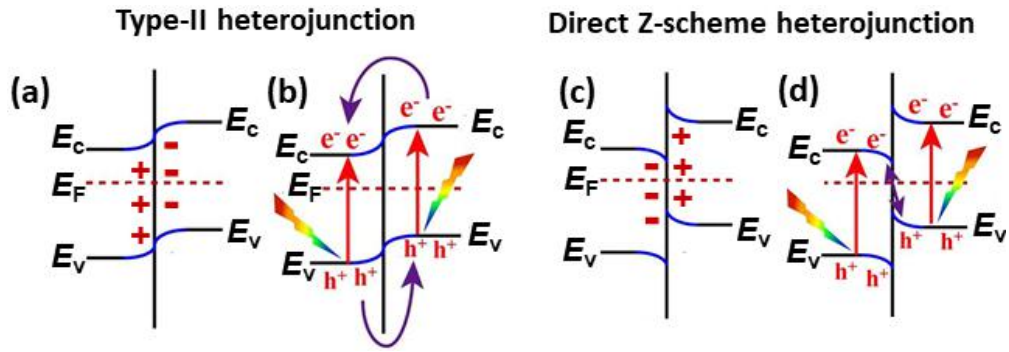


**Figure 29.** Type-II and direct Z-scheme heterojunction. (a) and (b) Type-II photocatalyst: (a) Band bending at the interface due to the formation of the interface dipole; (b) Photo-generated carriers migrate according to the alignment shown in (a). (c) and (d) Direct Z-scheme photocatalyst; (c) Band bending at the interface due to the formation of the interface dipole; (d) Photo-generated carriers migrate according to the alignment shown in (c). Reproduced with permission and adapted from Ref. 337.

The problem has been recently addressed by performing VASP DFT calculations with the HSE06 functional.[363] The g-$C_3N_4$/$TiO_2$ interface was built by combining the g-$C_3N_4$ and $TiO_2$(001) units (as experimentally observed).[364] In g-$C_3N_4$/$TiO_2$ the VB and CB bands of $TiO_2$ are 0.63 eV and 0.24 eV, respectively, below those of g-$C_3N_4$ (Type-II alignment).

However, the DFT calculations show the formation a large interface dipole of 1.2 D, with charge polarization $\delta^-$ on $TiO_2$ and $\delta^+$ on g-$C_3N_4$, which confer to the junction the typical direct Z-scheme character, Figure 30. This provides a first principles rationalization of the observed behaviour of g-$C_3N_4$/$TiO_2$ photocatalyst under irradiation and shows that the band alignment can be insufficient to predict the direction of charge carriers' migration.

However, the direction of the charge carriers flow can be reversed by modifying the interface. This requires to switch the direction of the interface dipole. A way to do this is to introduce a buffer layer between the g-$C_3N_4$ and $TiO_2$ components. In particular, the addition of a thin $SrTiO_3$ layer, thus creating a ternary g-$C_3N_4$/$SrTiO_3$/$TiO_2$ junction,[365] leads to the desired result. The g-$C_3N_4$/$SrTiO_3$ interface is characterized by stronger covalent bonds compared to the g-$C_3N_4$/$TiO_2$ one. The band edges of $SrTiO_3$ are between those of $TiO_2$ and g-$C_3N_4$, leading to a cascade sequence of Type-II alignments, as for the $TiO_2$/$TiO_2$/ZnS case discussed above. The strong chemical bonds at the g-$C_3N_4$/$SrTiO_3$ side of the interface result in a large dipole of opposite sign compared to that of g-$C_3N_4$/$TiO_2$. The insertion of the $SrTiO_3$ layer leads to the creation of an interface dipole that favours migration of photogenerated electrons toward $TiO_2$ ($\delta^+$ charge polarization) and photogenerated holes toward g-$C_3N_4$ ($\delta^-$ charge polarization). This picture is fully consistent with the experiments,[365] thus providing a rationalization of the opposite behaviour of g-$C_3N_4TiO_2$, a direct Z-scheme photocatalyst, and g-$C_3N_4$/$SrTiO_3$/$TiO_2$, a classical Type-II heterojunctions, Figure 30.

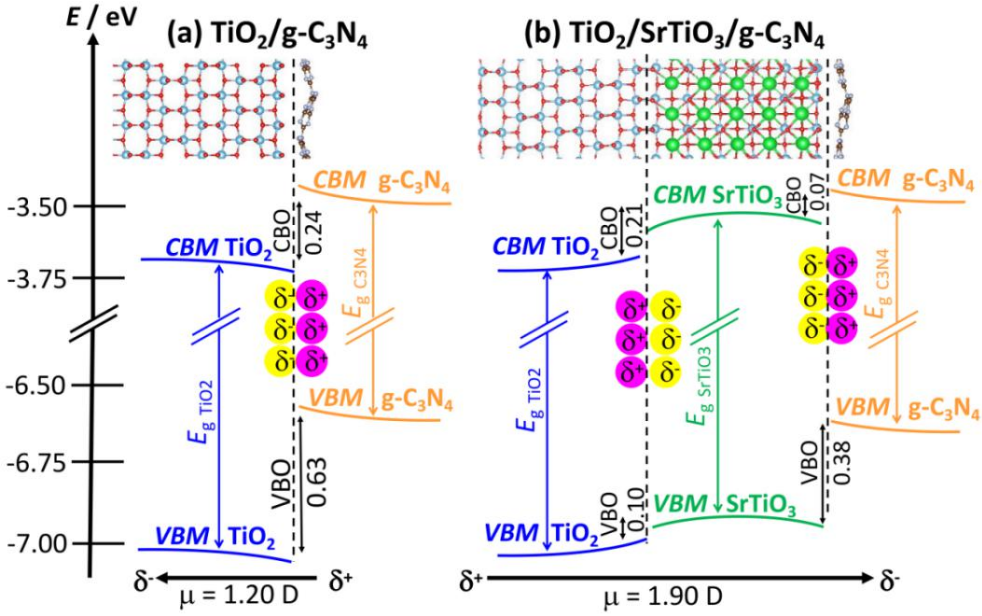


**Figure 30.** Band alignment and interface dipole in g-$C_3N_4$/$TiO_2$, a direct Z-scheme photocatalyst, and g-$C_3N_4$/$SrTiO_3$/$TiO_2$, a Type-II heterojunctions. The change in behaviour is due to the $SrTiO_3$ buffer layer, and the inversion of the interface dipole. [9]

### 4.2.4 Summary

From a methodological point of view, the use of hybrid functionals or other self-interaction corrected functionals is recommended, while less important is the choice of the hybrid functional used due to them guarantees a balanced description of the two (or more) components of the junction. Different models can be adopted to determine the band alignment. In some cases, the use of the simple "independent units" model is sufficient to predict the band alignment.

In the other cases, either the "alternating slabs junction" or the "surface terminated junction" models are employed, and the chemical nature of the interface is explicitly included. In both cases, the choice of the surfaces to be joined is crucial: this determines the amount of strain in the model, the thermodynamic stability of the interface, the occurrence of charge transfer, the final band offsets, etc. Both "alternating slabs junction" and "surface terminated junction" approaches make use of slabs to represent the bulk materials, and a proper study of the convergence of the electronic properties with slab thickness is required. Once the explicit model of the interface is defined, some other aspects need to be considered. One is the direction of the charge polarization at the interface. This results in an interface dipole that can facilitate the charge carriers separation, or act to modify the nature of the band alignment, for instance from Type-II to a direct Z-scheme. In the examples have been shown how in some systems the inclusion of buffer layers can be used to reverse the sign of the charge polarization and the nature of the band alignment.

Another aspect that is worth considering is the explicit formation of photogenerated electron/hole pairs by computing the triplet excited state of the system. The subsequent structural relaxation results in polarons formation and carriers localization on the two sides of the junction. However, this may result in a strong coulomb interaction that makes the charge carriers separation less favorable, despite the alignment of the bands. From the few cases studied it does not seem that point defects or impurity atoms included in one or both sides of the junction have a major effect on the final alignment and band offsets. On the other hand, very few studies have been dedicated to this aspect, and further work is necessary to provide an answer to this question.

# Chapter V: Co-Catalyst

In this chapter are provided two particular examples of co-catalyst for electro-catalysis applications, both based on single atom catalyst (SACs) for the prediction of the hydrogen evolution reaction (HER). First, a collaboration with the group of Prof. In-Hwan Lee from the Korea University is presented and in the second part the role of dihydride and dihydrogen compounds in the hydrogen evolution reaction is discussed.

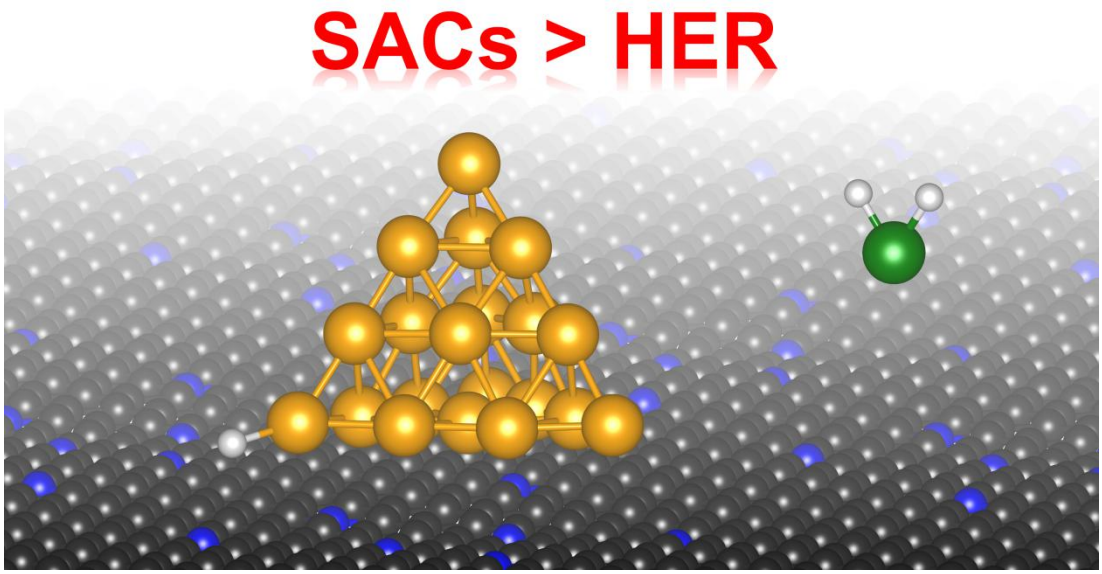

## 5.1 Gold nanoclusters supported on nitrogen-doped graphene as a photocatalyst for hydrogen conversion

Here is reported a collaboration with the group of Prof. In-Hwan Lee from the Korea University, where they have been synthesized a series of well-dispersed and stable size-different Au spherical nanocatalysts: single atoms, SAs (r = 0.25nm); nanoclusters, NCs (r = 0.5-1.0nm); and nanoparticles, NPs (r = 10nm) on nitrogen-doped graphene (N-Gr) via the pyrolysis method. They have observed that Au NCs/N-Gr photocatalyst exhibit an impressive HER achievement (3.16 µmol $mg^{-1}_{cat}$ $h^{-1}$) over Au single atoms/N-Gr (2.06 µmol $mg^{-1}_{cat}$ $h^{-1}$) and Au nanoparticles/N-Gr (0.92 µmol $mg^{-1}_{cat}$ $h^{-1}$) under visible-light, with a maximum apparent quantum yield of 14.30%. In order to simulate the experimental observations and to provide an additional answer to the observed trend, we have been considered the single $Au_1$ atom (SAs), $A_{20}$ clusters (NCs), and Au(111) surface (NPs) supported on N-doped graphene (N-Gr) to evaluate the HER by computing the free energy of hydrogen adsorbed in the different models.

### 5.1.1 Introduction

A photocatalyst represent a fundamental part for the photocatalysis process. In the last years attention is given to the develop of hydrogen cells for the water splitting process by using a photocatalyst,[366] which can help to solve environmental issues. In this respect plasmonic metals represent an advantageous photocatalyst to enhance light-to-fuel production due to the effect of surface plasmon resonance (SPR), which results from interactions between light and plasmonic nanoparticles (NPs).[367] Thus far, gold and silver NPs are known as the best SPR host materials because they offer extremely free electron densities (~$10^{23}$ $cm^{-3}$) in the visible-light region.[368] Mustafa S. Y, et al,. have been reported the size-dependence of SPR has an essential role in practical applications.[369] In the limit of larger metal NPs (mean diameter larger than 25 nm), the SPR peak commonly strengthens as d decreases.[370]

---

The content of this sub-chapter is published in the Journal of Materials Chemistry A: D. V. Dao, L. A. Cipriano, G. Di Liberto, T. T. D. Nguyen, S-W. Ki, H. Son, G-C. Kim, K. H. Lee, J-K. Yang, Y-T. Yu, G. Pacchioni, and I-H. Lee, "Plasmonic Au Nanoclusters Dispersed in Nitrogen-Doped Graphene as a Robust Photocatalysts for Light-to-Hydrogen Conversion, *J. Mater. Chem. A*., 9 (2021) 22810-22819. https://doi.org/10.1039/D1TA05445G

This trend remains insufficiently investigated for the case of smaller metallic NPs with diameters below 25 nm. For example, Peng et al. have been demonstrated that as d decreases, the SPR peak strengthens for Ag NPs.[371] Furthermore, Zeng et al. have been proposed that Au single atoms (SAs) immobilized by carbon nitride bring superior photocatalytic hydrogen evolution.[372] The shape dependence of plasmon resonance of gold nanoparticles has been considered by Colleen L. N. and Jason H. Hafter, they found that metal nanoparticles cause enhanced optical absorption and scattering that is tunable through the visible and near-infrared.[373] These investigations imply that nanoclusters can be potentially used under light irradiation for the SPR.

In the last years particular attention have been given to graphene (Gr), a two-dimensional (2D) carbon structure which is considered as a proper electron acceptor to prolong the lifetime of plasmon-produced charge carriers. Indeed, Gr has been widely utilized in photocatalysis because it has a large surface area, excellent electron transfer capability, and chemical stability.[374,375] As a support, the Gr 2D material can accelerate the separation and transportation of produced electron-hole pairs and also prevent the agglomeration of photocatalyst particles, thus improving photoconversion.[375] Furthermore, it has been reported that nitrogen-doped graphene (N-Gr) present interest as a photocatalyst for the hydrogen production because of its highly tunable optical properties.[376,377] The C–N bonds can additionally strengthen the light absorption to facilitate the photocatalytic reactions. As a result, N-Gr can also serve as a photocatalyst, particularly for light-driven hydrogen production.[377]

### 5.1.2 Computational details

The calculations were performed at the level of Density Functional Theory (DFT), as implemented in VASP 6.1.1 code.[95–97] The valence electrons, C ($2s^2 2p^2$), N ($2s^2 2p^3$), and Au ($6s^1 5d^{10}$) have been expanded on a set of plane waves with a kinetic cut-off of 400 eV, whereas the core electrons were treated with the Projector Augmented Wave (PAW) approach.[250,251] The Perdew-Burke-Ernzerhof (PBE) exchange−correlation functional was used.[19] The truncation criteria for electronic and ionic loops were set to $10^{-6}$ eV and $-10^{-3}$ eV/Å, respectively. The reciprocal space has been sampled by a Γ-centered mesh adopting a 5×5×1 grid. The grid was increased to 20×20×1 for the density of states calculations (DOS). Dispersion forces have been considered according to the Grimme's D3 parametrization scheme.[378]

A Nitrogen-dopant concentration of about 4% was considered in all models, similar to that found experimentally. Simulations span from relatively small cells when $Au_1$ was adsorbed, to big supercells to accommodate $Au_{20}$ nanoclusters.

Here is just reported a summary of how Prof. In-Hwan Lee group's have been synthesized a series of size-different Au spherical nanocatalysts; single atoms: SAs (r = 0.25 nm), nanoclusters: NCs (r = 0.5-1.0 nm), and nanoparticles: NPs (r = 10 nm) supported on nitrogen-doped graphene (N-Gr) via the pyrolysis method, see Figure 31, which represents in a schematic way the procedure followed to synthesize the mentioned catalysts. More information about the experimental details, preparation and structural characterization of Gr, N-Gr, Au SAs/N-Gr, Au NCs/Gr, Au NCs/N-Gr, and Au NPs/N-Gr) can be found in the original paper and in its corresponding supporting information.[379]

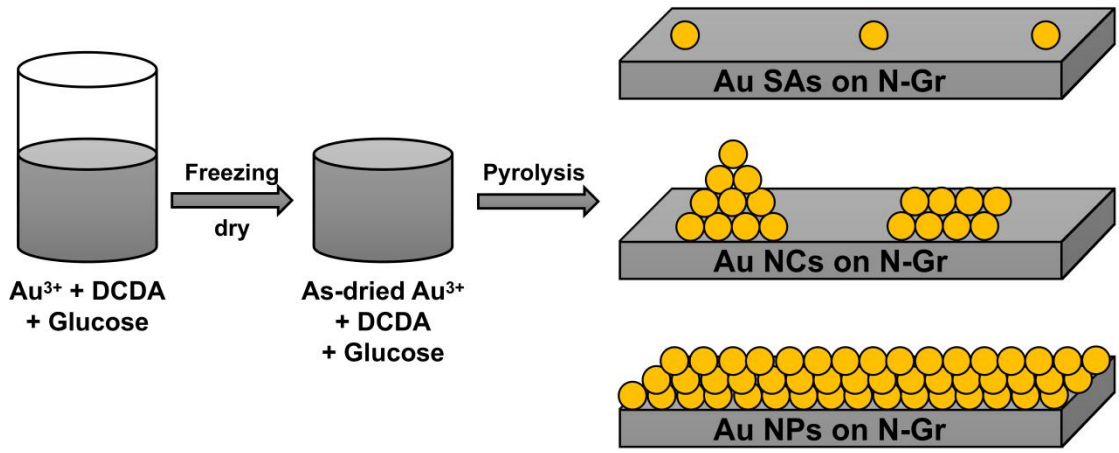


**Figure 31.** Schematic representation of the experimental procedure.

### 5.1.3 Results and discussion

#### 5.1.3.1 Photoelectrocatalytic HER mechanism

The evaluation of the photocatalytic hydrogen production was performed in a mixed aqueous solution of 0.25 M $Na_2SO_3$ and 0.25 M $Na_2S$ as sacrificial agents under visible-light irradiation. After testing the samples for five hours, it was found that the Au NCs/N-Gr nanocomposites deliver the highest hydrogen amount (15.8 µmol $mg^{-1}$), followed by Au SAs/N-Gr (10.3 µmol $mg^{-1}{}_{cat}$), Au NPs/N-Gr (4.6 µmol $mg^{-1}{}_{cat}$), and free N-Gr (1.2 µmol $mg^{-1}{}_{cat}$) respectively, as described in Figure 32(a).

Next, the HER rate was normalized as a function of time and it was found that the Au NCs/N-Gr nanocomposites achieve excellent photocatalytic activity with an HER rate of about 3.16 µmol $mg^{-1}_{cat}$ $h^{-1}$, which is 153%, 343%, and 1317% more than those obtained from Au SAs/N-Gr (2.06 µmol $mg^{-1}_{cat}$ $h^{-1}$), Au NPs/N-Gr (0.92 µmol $mg^{-1}_{cat}$ $h^{-1}$), and N-Gr (0.24 µmol $mg^{-1}_{cat}$ $h^{-1}$), respectively, see Figure 32(b).

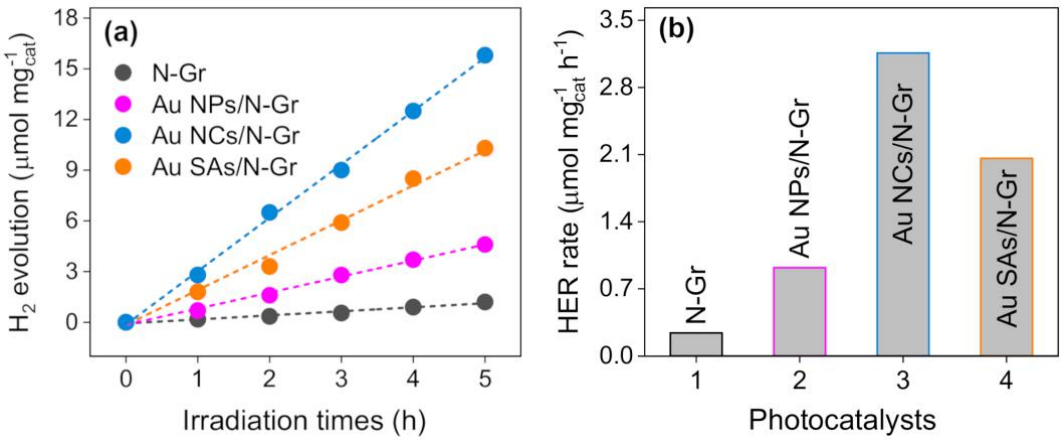


**Figure 32.** (a) Time-dependent hydrogen production amount and (b) Hourly hydrogen production rate. [379]

From Figure 32, the results show that the Au NCs consisting of a few tens of atoms supported on N-Gr offer the best activity for light-to-hydrogen conversion in a mixture of $Na_2SO_3$ and $Na_2S$ solution. The Au SAs exhibit an inferior performance compared to the Au NCs, even if it has a strong photocurrent response. The inferior performance of the Au SAs was attributed to the fast recombination of electronic excitations on the surface before being accessible to the N-Gr to direct the catalytic reactions.

As the Au NCs/N-Gr was the best photocatalyst, the HER activity was also performed in methanol and TEOA aqueous sacrifices as the common hole scavengers under visible-light. However, the highest hydrogen production was obtained with the mixture of $Na_2SO_3$ and $Na_2S$ (3.16 µmol $mg^{-1}_{cat}$ $h^{-1}$), then in TEOA (1.82 µmol $mg^{-1}_{cat}$ $h^{-1}$), and MeOH (0.84 µmol $mg^{-1}_{cat}$ $h^{-1}$), respectively.

### 5.1.3.2 DFT modeling of the HER activity

In order to study the HER activity by DFT modeling, four different catalysts have been compared: (a) N-Gr; (b) single Au atoms supported on N-Gr (Au SAs/N-Gr); (c) small Au nanoclusters (Au NCs/N-Gr); (d) Au nanoparticles (Au NPs/N-Gr). To represent these catalysts, the following DFT models have been considered:

(a) N-Gr: a N-Gr supercell with a concentration of about 4% of N atoms, close to that experimentally observed; in particular, the graphitic Nitrogen N-Gr was simulated, as this is the dominant species from XPS analysis carried out by our experimental colleges.

(b) Au SAs/N-Gr: a Au single atom stabilized on N-Gr, $Au_1$/N-Gr;

(c) Au NCs/N-Gr: a $Au_{20}$ nanocluster (either with the tetrahedral or planar shape) supported on N-Gr, $Au_{20}$/N-Gr;

(d) Au NPs/N-Gr: since nanoparticles of 20 nm contain from half-a-million to a million of atoms, here the Au NPs was represented by studying the adsorption of hydrogen on the extended Au(111) surface.

#### 5.1.3.2.1 Characterization of the catalysts

We observed that after doping with nitrogen, N-Gr remains as a flat monolayer and the Fermi level in N-Gr is shifted to the valence band, confirming that nitrogen-doped graphene behaves as a n-type semiconductor. Compared to graphene, each N-atom introduces an excess electron delocalized over the entire plane. After testing different Au adsorption sites, it was found that Au atom binds preferentially on the C atom adjacent to the N-dopant on the N-Gr support, on top of $C_{ortho}$ with a BE = -0-99 eV, see Figure 33(a-b).

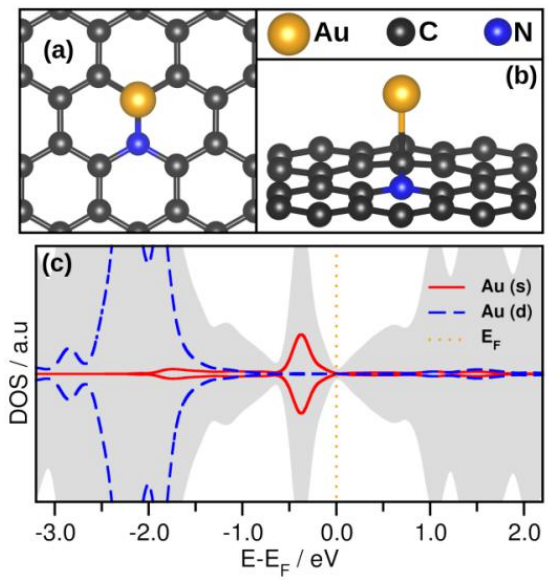


**Figure 33.** (a) top and (b) side views of Au binding on top of $C_{ortho}$, on N-Gr and (c) density of states for this site. [379]

On this site, the Au atom assumes a negatively charged state, $Au^{-1}$. This result can be obtained by the combined analysis of atomic charges according to the Quantum Theory of Atoms In Molecules (QTAIM),[266–270] and the density of states (DOS) profile, Figure 33(c). These results show that the dispersion of Au metal can lead to fully reduced states by the N-Gr reducing agent during the pyrolysis stage, in line with the XPS analysis carry out in the experimental section of this study.[379]

For $Au_{20}$, two stable conformers have been considered, tetrahedral (T-$Au_{20}$) and planar (P-$Au_{20}$), see Figure 34. Gas-phase T-$Au_{20}$, which has been observed experimentally, is 2.80 eV more stable than the planar isomer; the band gap is 1.80 eV for T-$Au_{20}$ and 0.69 eV for P-$Au_{20}$, respectively, showing that at this cluster size the system is non-metallic.

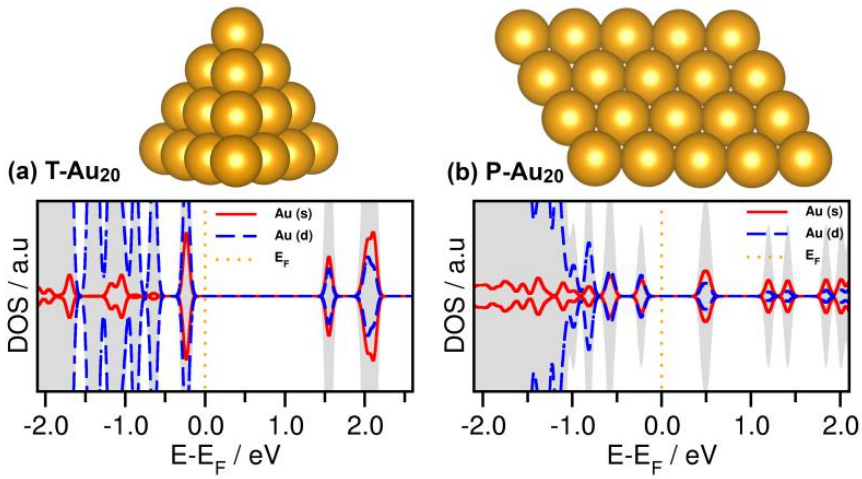


**Figure 34.** (a) Tetrahedral (T-$Au_{20}$) and (b) planar (P-$Au_{20}$) conformers and its corresponding density of states. Yellow balls correspond to gold atom. [379]

Both isomers have been adsorbed on pristine graphene, Gr, and N-doped graphene, N-Gr. On graphene, Gr, the T-$Au_{20}$ isomer is 1.22 eV more stable than the P-$Au_{20}$ one, and in both cases, the interaction is dominated by dispersion forces, with no charge transfer to the support, Table 13 and Figure 35. Things are very different on N-graphene. Here P-$Au_{20}$ becomes the preferred structure, 0.13 eV more stable than the T-$Au_{20}$ isomer. The two structures are thus iso-energetic on N-graphene as also reported recently. The bonding, however, is no longer due exclusively to dispersion interactions. In fact, when dispersion contributions are removed, T-$Au_{20}$ is unbound by 0.30 eV while P-$Au_{20}$ is bound by -1.04 eV. This is a genuine chemical bond which reflects the occurrence of an electron transfer at the interface, -1.69 |e|from N-Gr to P-$Au_{20}$.

Notice that T-$Au_{20}$ has the same BE on both graphene and N-graphene (0.05 eV more stable on graphene), while P-$Au_{20}$ is by far more stable on N-graphene, see Figure 36 for the isomers on N-Gr and its respective density of states.

**Table 13.** $Au_{20}$ isomers on graphene and N-graphene. Binding energy with ($BE_{WD}$, in eV) and without dispersion ($BE_{WOD}$, in eV), relative energy with and without dispersion contribution ($RE_{WD}$ and $RE_{WOD}$, in eV), bond lengths (d, in Å), dipole moment (μ, in a.u.), and charge transfer from the support to the isomers (CT, in |e|).

| site | $BE_{WD}$ | $RE_{WD}$ | $BE_{WOD}$ | $RE_{WOD}$ | $d_{C\text{-}N}$ | $d_{Au\text{-}N}$ | $d_{Au\text{-}C}$ | μ | CT |
|---|---|---|---|---|---|---|---|---|---|
| T-$Au_{20}$/Gr | -2.26 | 0.00 | 0.22 | 0.00 | --- | --- | 3.12-3.46 | 1.51 | -0.04 |
| P-$Au_{20}$/Gr | -3.85 | 1.22 | 0.45 | 1.75 | --- | --- | 3.32-3.60 | 1.20 | -0.13 |
| T-$Au_{20}$/N-Gr | -2.21 | 0.13 | 0.30 | 0.00 | 1.41 | 3.48-3.69 | 3.16-3.52 | 3.49 | -0.48 |
| P-$Au_{20}$/N-Gr | -5.14 | 0.00 | -1.04 | 0.34 | 1.41 | 3.50-3.60 | 3.35-3.66 | 6.98 | -1.69 |

Comparing the DOS plots of the gas-phase clusters and after adsorbing them on Gr; with T-$Au_{20}$ was observed that the valence band is shifted to lower energy levels with respect to the Fermi level, while with P-$Au_{20}$ the conduction band is shifted close to the Fermi level, the band gap of the clusters remain intact, see Figures 34 and 35. However, when the clusters were adsorbed on N-Gr, the band gaps are reduced. On T-$Au_{20}$/N-Gr the band gap is reduced by 0.3 eV and the conduction band was shifted to the Fermi level; with P-$Au_{20}$/N-Gr the conduction band was also shifted to the Fermi level and the band gap is reduced by 0.1 eV with respect to the gas-phase cluster, see Figures 34 and 36.

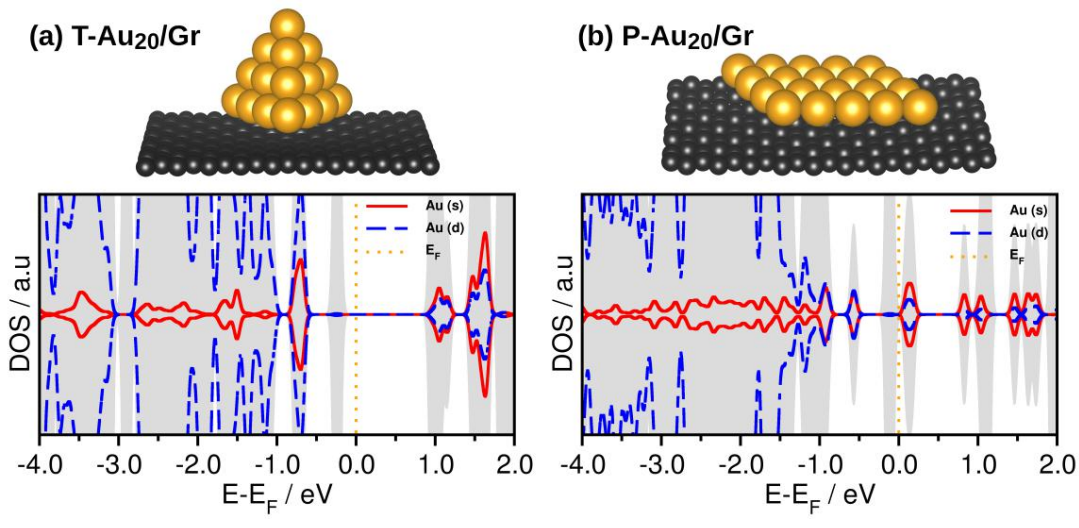


**Figure 35.** Side view of the $Au_{20}$ isomers on Gr and it respective density of states. (a) T-$Au_{20}$/Gr and (b) P-$Au_{20}$/Gr. Black and yellow balls correspond to carbon and gold atoms, respectively. [379]

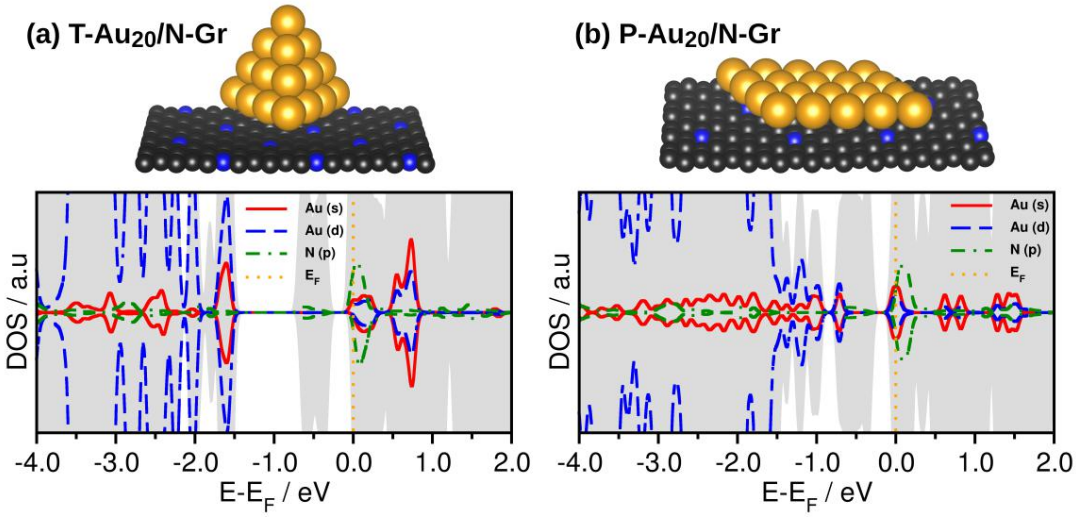


**Figure 36.** Side view of the $Au_{20}$ isomers on N-Gr and it corresponding density of states. (a) T-$Au_{20}$/N-Gr and (b) P-$Au_{20}$/N-Gr. Black, blue, and yellow balls correspond to carbon, nitrogen, and gold atoms, respectively. [379]

#### 5.1.3.2.2 HER activity of the catalyst

The thermodynamics of the adsorption and hydrogen evolution on the four model catalysts was evaluated following the procedure proposed by Nørskov et al.[380] One starts by computing the energy of an H atom adsorbed on a given site; the adsorption energy is defined with respect to the free $H_2$ molecule:

$$\Delta E_H = \frac{1}{n}(E_{surf+nH} - E_{surf} - \frac{n}{2}E_{H_2}) \qquad \text{Eq. (14)}$$

Since we adsorbed just one H atom the equation is reduced to:

$$\Delta E_H = E_{surf+H} - (E_{surf} + \frac{1}{2}E_{H_2}) \qquad \text{Eq. (15)}$$

The H adsorption on N-Gr implies four sites. The most stable is on top of the $C_{ortho}$, which is indicated with a gray shading color in Table 14, see also Figure 37(a). Since with N-Gr the most stable site was the $C_{ortho}$, an Au atom was adsorbed on top on this site and next the H was adsorbed as well on top of Au, $Au_1$/N-Gr, see Figure 37(b). With Au(111) surface three possible sites were found, where the hollow site is the most stable, Table 14 and Figure 37(c).

**Table 14.** Adsorption energy of hydrogen on different sites ($\Delta E_H$, in eV) of N-Gr, Au1/N-Gr, and Au(111) surface, respectively. N-H, C-H, C-Au, and Au-H bond distances are also reported in the Table. The most stable site is indicated in shading gray color.

| Model | site | $\Delta E_H$ | $d_{N-H}$ | $d_{C-H}$ | $d_{C-Au}$ | $d_{Au-H}$ |
|---|---|---|---|---|---|---|
| N-Gr | N | 1.62 | 1.05 | --- | --- | --- |
| | $C_{ortho}$ | 0.41 | --- | 1.12 | --- | --- |
| | $C_{meta}$ | 1.01 | --- | 1.13 | --- | --- |
| | $C_{para}$ | 0.66 | --- | 1.12 | --- | --- |
| $Au_1$/N-Gr | $Au_1/C_{ortho}$ | -0.60 | --- | --- | 2.43 | 1.57 |
| Au(111) | $Au_1$ | 0.45 | --- | --- | --- | 1.60 |
| | $Au_{23}$ | 0.45 | --- | --- | --- | 1.60 |
| | Hollow | 0.26 | --- | --- | --- | 1.93 |

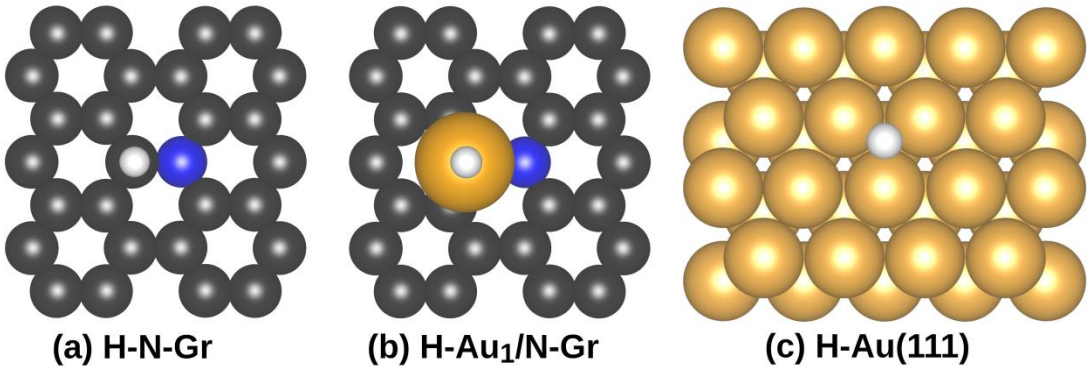


**Figure 37.** Top view of the one hydrogen adsorbed on (a) N-Gr, (b) $Au_1$/N-Gr, and Au(111) respectively. Black, blue, yellow, and white balls correspond to carbon, nitrogen, gold, and hydrogen atoms. [379]

Contrary to N-Gr and the Au(111) surface, several adsorption sites exist on T-$Au_{20}$ and P-$Au_{20}$ supported on N-Gr, see Table 15 and Figure 38. In the case of T-$Au_{20}$, the strongest adsorption sites are the Au1 and Au4 atoms at the interface with N-Gr, with a binding energy $\Delta E_H$ of -0.40 eV, marked in shading gray color (a negative adsorption energy indicates an exothermic process). While with P-$Au_{20}$, the strongest adsorption site is the Au2.

**Table 15.** Adsorption energies of hydrogen on T-$Au_{20}$/N-Gr and P-$Au_{20}$/N-Gr supports ($\Delta E_H$, in eV), and the C-Au, N-Au, and Au-H bond distances ($d$, in Å). The most stable site is indicated in shading gray color.

| System | site | $\Delta E_H$ | $d_{C\text{-}Au}$ | $d_{N\text{-}Au}$ | $d_{Au\text{-}H}$ |
|---|---|---|---|---|---|
| T-$Au_{20}$/N-Gr | Au1 | -0.40 | 3.37-3.50 | 3.48-3.49 | 1.63 |
| | Au2 | 0.09 | 3.17-3.50 | 3.46-3.56 | 1.63 |
| | Au3 | 0.10 | 3.31-3.50 | 3.40-3.47 | 1.63 |
| | Au4 | -0.39 | 3.29-3.54 | 3.42-3.50 | 1.63 |
| | Au5 | 0.13 | 3.27-3.53 | 3.46-3.59 | 1.77 |
| | Au6 | 0.22 | 3.31-3.51 | 3.38-3.53 | 1.60 |
| | Au7 | 0.17 | 3.21-3.50 | 3.57-3.59 | 1.77 |
| | Au8 | -0.15 | 3.31-3.52 | 3.46-3.56 | 1.62 |
| P-$Au_{20}$/N-Gr | Au1 | -0.20 | 3.39-3.60 | 3.51-3.63 | 1.61 |
| | Au2 | -0.47 | 3.40-3.58 | 3.52-3.64 | 1.72 |
| | Au3 | 0.23 | 3.31-3.54 | 3.42-3.61 | 1.79 |

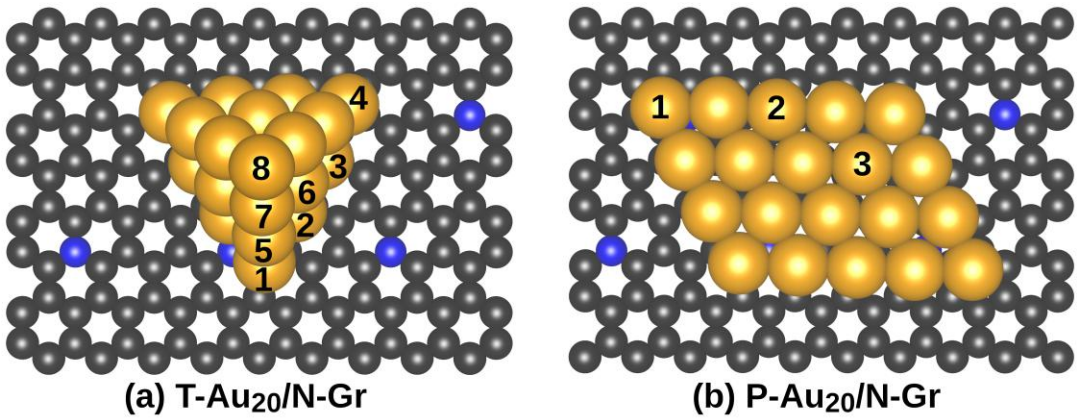


**Figure 38.** Hydrogen adsorption sites of (a) T-$Au_{20}$ and (b) P-$Au_{20}$ supported on N-Gr. Black, blue, and yellow balls correspond to carbon, nitrogen, gold, and hydrogen atoms. [379]

After knowing which is the most stable site for each support, it was possible to compare the activity of the various catalysts by using the full set of adsorption data. In order to do this, one has to compute the free energies for H adsorption and generate a plot of the free energy diagram for the HER at standard conditions. The free energy of the adsorbed hydrogen is defined as:[380]

$$\Delta G_H = \Delta E_H + \Delta E_{ZPE} - T\Delta S_H \qquad \text{Eq. (17)}$$

Where $\Delta E_{\mathrm{H}}$ is the adsorption energy for each catalyst, and $\Delta E_{ZPE}$ is the zero-point energy. The entropy of adsorption of ½ $H_2$ is $\Delta S_H \cong \frac{1}{2} S^0_{H_2}$, where $S^0_{H_2}$ is the entropy of $H_2$ in the gas-phase at standard conditions, e.g., 130.68 J $mol^{-1}$ $K^{-1}$ at 298.15 K and 1 bar. Considering these conditions, $T\Delta S_H$ becomes -0.193 eV.

In Table 16 are reported the computed free energies for H adsorbed on the more stables sites for each catalysts. From these data, one can construct the free energy diagram for the HER at equilibrium, as shown in Figure 39. The best catalysts are those where the H adsorption has a free energy close to that of the precursor, $H^+ + e^-$ (0 eV), and of the product, ½ $H_2$ (0 eV). This is because the catalysts that exhibit free energies close to those of reactants and products, e.g., close to zero, are at the apex of the typical volcano plot of HER. These catalysts do not bind too strongly or too weakly to the reacting species. Table 16 reports the adsorption energy ($\Delta E_H$, in eV), the contribution due the ZPE ($\Delta E_{ZPE}$, in eV), the entropy contribution ($T\Delta S_H$, in eV), and the free energy ($\Delta G_H$, in eV) of hydrogen in the four supports considered in this study.

**Table 16.** Adsorption energy ($\Delta E_H$, in eV), the contribution due the ZPE ($\Delta E_{ZPE}$, in eV), the entropy contribution ($T\Delta S_H$, in eV), and the free energy ($\Delta G_H$, in eV) of hydrogen in the supports considered in this study.

| Name | Catalyst | $\Delta E_H$ / eV | $\Delta E_{ZPE}$ / eV | $T\Delta S_H$ / eV | $\Delta G_H$ /eV |
|---|---|---|---|---|---|
| N-Gr | N-Gr | 0.41 | 0.18 | -0.19 | 0.78 |
| Au(111) | Au NPs | 0.26 | -0.01 | -0.19 | 0.44 |
| T-$Au_{20}$/N-Gr | Au NC | -0.40 | -0.01 | -0.19 | -0.22 |
| P-$Au_{20}$/N-Gr | Au NC | -0.47 | -0.01 | -0.19 | -0.29 |
| $Au_1$/N-Gr | Au SAs | -0.60 | 0.03 | -0.19 | -0.38 |

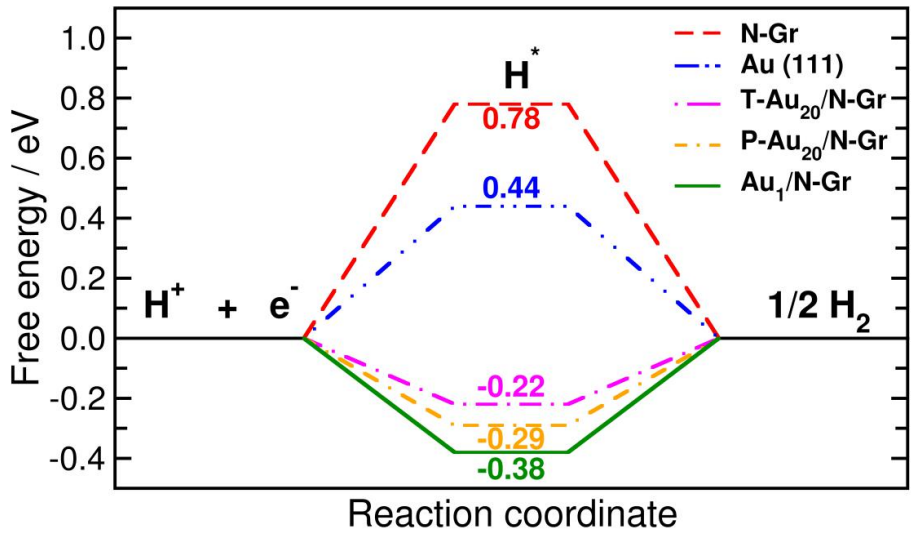


**Figure 39.** H adsorption free energy on: N-Gr (red), Au (111) (blue), T-$Au_{20}$/N-Gr (magenta), P-$Au_{20}$/N-Gr (orange), and $Au_1$/N-Gr (green). Results from DFT-PBE calculations. [379]

From Figure 39, it emerges that the worst catalyst is N-Gr; this is because H binding on N-Gr is too weak, with a positive adsorption energy of 0.41 eV, see Table 16.

This corresponds to a very high free energy for adsorption, 0.78 eV. N-Gr is not able to dissociate $H_2$ and is not a good catalyst for the reaction. Au(111), which models the surface of Au NPs of around 20 nm in size, also has a positive adsorption energy of 0.26 eV (hollow site), which indicates that $H_2$ dissociation is endothermic. The free energy for adsorption is still quite high, 0.44 eV, although 0.34 eV lower than N-Gr, showing that Au NPs are much better catalysts than N-Gr. However, they still bind hydrogen too weakly. The third case is that of Au NCs. Here we notice that both T-$Au_{20}$/N-Gr and P-$Au_{20}$/N-Gr, the nearly isoenergetic tetrahedral and planar isomers of $Au_{20}$ on N-Gr, are able to adsorb hydrogen with an exothermic reaction (-0.40 eV or -0.47 eV, see Table 16). The corresponding free energies are -0.22 eV and -0.29 eV, respectively, e.g., close to the optimal zero value expected for an ideal catalyst. Finally, a Au single atom catalyst binds H rather strongly, by -0.60 eV, so that taking into account the *ZPE* and $\Delta S_H$ corrections this results in a too negative free energy, -0.38 eV, and an HER activity which is expected to be in between that of the Au NCs and the Au NPs.

Thus, according to the DFT calculations, Au NCs/N-Gr containing a few tens of atoms are the best catalysts for the HER process, followed by Au SAs/N-Gr, Au NPs/N-Gr and N-Gr. This is precisely the order of reactivity measured experimentally. However, the DFT results refer to the intrinsic activity of the catalysts considered, and do not include plasmonic effects. This suggests that beside the stronger plasmon resonance, also the intrinsic binding capability of the H species plays a role in the overall photocatalytic performance in HER. The two effects, plasmon resonance and H binding ability seem to work together and result in a high light-to-hydrogen conversion for the Au NCs/N-Gr photocatalyst.

### 5.1.4 Summary

Taken together, the experimental and theoretical investigations suggest that an efficient and stable photocatalyst based on Au NCs/N-Gr nanocomposites can be obtained for light-to-fuel conversion. Where the photocatalyst performance follow the next order; Au NCs/N-Gr > Au SAs/N-Gr > Au NPs/N-Gr > N-Gr, respectively. These performances were synergistically attributed to two effects, (a) the strong surface plasmon resonance stimulated by light absorption and transferred near the surface of Au NCs, where the N-Gr conductive support can prolong the plasmon-produced hot electrons and direct the light-to-hydrogen conversion; (b) a intrinsic binding capability of the H on the different supports.

## 5.2 Single atom catalysts for hydrogen evolution reaction: the role of dihydride or dihydrogen complexes

This study start from the idea that the activity of SACs in HER is usually rationalized or predicted using the original model proposed by Nørskov and based on the formation of a MH intermediate. However, SACs differ substantially from metal surfaces, and can be considered analogs of coordination compounds, where at variance with metal surfaces, stable dihydride or dihydrogen complexes (HMH) can form. We show that the formation of stable HMH intermediates, in addition to the MH one considered in the original model, may change the kinetics of the process for SACs. The sub-chapter is organized as following; first an introduction and the computational details are given. Next, the equations for modelling the kinetics of HER on surfaces and SACs is discussed, and a new equation is provide. In the last part an experimental benchmark and the comparison of the new model is presented.

### 5.2.1 Introduction

The hydrogen evolution reaction (HER) is one of the simplest but at the same time most important reactions in chemistry, $2\ H^+ + 2\ e^- \rightarrow H_2$. It is a two-electron transfer reaction occurring at the cathode in electrochemical water splitting, $H_2O \rightarrow H_2 + ½\ O_2$.[381–384] It offers the potential to produce $H_2$, a critical chemical species, important both as reagent (e.g. in ammonia synthesis),[385] as fuel (e.g. in fuel cells technology),[386] and in several other industrial processes (e.g. electronics, metallurgy, chemical industry, etc.). To achieve a high energetic efficiency for water splitting, specific catalysts that minimize the overpotential necessary for the HER are needed.[387] Among the best catalysts is platinum, which however has the disadvantage of being a critical and costly raw material.[388,389] For this reason, an intense activity has been dedicated to the search for new materials with high catalytic efficiency for the HER.

Among new catalysts for the HER, there is the emerging class of single atom catalysts (SAC).[390–392]

---

The content of this sub-chapter is published in the Journal of American Chemistry Society: G. Di Liberto, L. A. Cipriano, and G. Pacchioni, “Role of Dihydride and Dihydrogen Complexes in Hydrogen Evolution Reaction on Single Atom Catalysts”, *J. Am. Chem. Soc.*, 143, 48 (2021) 20431-20441. https://doi.org/10.1021/jacs.1c10470

The concept of SAC was introduced in 2011[393] although the presence of isolated atoms or single sites at the surface of heterogeneous catalysts is known since a longer time.[391,394,395] SACs consist of isolated metal atoms dispersed and stabilized on a support, and their chemistry is largely determined by the interaction with the surrounding - in this respect, they are less "single" than the name suggests. Certainly, in terms of structure SACs are better defined than supported metal particles, where the activity is largely dependent on the size and shape of the nanoparticle.[396] Since in SACs the active site is relatively well defined, they are expected to provide higher selectivity than supported nanoparticles. SACs have the additional advantage of using tiny quantities of precious metals, thus making them interesting for the design of novel classes of industrial catalysts.

Theoretical studies based on electronic structure calculations, in particular on Density Functional Theory (DFT), have proven useful for the preliminary screening of the large set of new catalytic materials for HER.[397–399] The screening of the "best" catalysts for HER is usually done following the proposed model by Nørskov and coworkers in a seminal paper.[380] This approach allows one to construct a volcano plot following the Sabatier principle, a qualitative concept in heterogeneous catalysis that states that the interactions between the catalyst and the substrate should be neither too strong nor too weak. Recently, the Sabatier principle was revisited by including in the analysis the applied overpotential resulting in an extended Sabatier principle which suggests that the optimum hydrogen-evolution catalyst binds hydrogen weakly rather than thermoneutrally, corresponding to the apex of the volcano plot. More details about these approches will be describe in the below sub-chapters.

Coming back to the Nørskov's model, the exchange current *i* for $H_2$ evolution, a measure of the efficiency of the reaction, is plotted against the H atom adsorption free energy, $\Delta G_H$. This model, originally developed for $H_2$ evolution from extended metal surfaces, is commonly employed in its original formulation also for the study of SACs.[400–407] The basic assumption of this model is that the adsorption free energy of the H atom is the only parameter required for describe the HER, as the recombination of two H atoms on the active site gives rise to the formation and desorption of $H_2$ into the gas-phase. This hypothesis is widely verified, and in fact on metal surfaces $H_2$ can only exist in dissociated form or in a physisorbed state where the molecule is weakly bound to the surface by van der Waals forces.[408]

However, the mechanism of $H_2$ formation and release can be very different on SACs as these class of materials can be considered surface analogs of organometallic complexes.[409–411] In organometallic chemistry the existence and the nature of stable dihydride and dihydrogen complexes - HMH - is well established.[412,413]

These consist of two H atoms bound to the same metal center. Changing the ligands, $L_x$, the level of activation and population of the $H_2$ anti-bonding orbital can be tuned, with formation of a classical dihydride complex, $ML_x(H)(H)$ (oxidative addition), or of the less conventional dihydrogen complexes $ML_x(H_2)$ where the H-H bond is only partly activated - typical H-H distance 0.8-0.9 Å. Pioneering work by Kubas has shown that dihydrogen complexes can have high chemical stability.[414,415] Since SACs have clear analogies with coordination complexes, it is to be expected that these kind of HMH intermediates can also form in this case. When this occurs, the original computational recipe of HER on metal surfaces can be insufficient, and a more elaborated model that accounts for the formation of two-hydrogen complexes is required. This does not necessarily imply that the original model leads to incorrect conclusions, only if both H adsorption processes on SACs are relevant, this affects the prediction of the kinetics of the reaction. However, it is not possible to exclude a priori the existence of the HMH intermediates and their role in the reaction.

This sub-chapter introduces an extension of the original Nørskov's theory by developing a theoretical approach that accounts for the presence of two intermediates in HER on SACs, the single hydrogen, MH, and the two-hydrogen, HMH, complexes. Here, the effect of the overpotential and of the solvent is not included but some details about these effects will be discussed below. However, we will show that for the specific case of SACs neglecting the possible formation of the second intermediate can have much larger effects than the overpotential or solvent effects.

The goal of this sub-chapter is to provide the fundamental kinetic equations and to report numerical DFT simulations demonstrating that: (a) the formation of the two intermediates is possible for most of the SACs considered, (b) the HMH intermediate can have different nature, dihydride or dihydrogen, depending on the interaction with the support, and (c) the proposed model should be used when predicting the activity of SACs, since the original model, designed and well-grounded for metal surfaces, may lead to different conclusions about the activity of SACs in HER. The model proposed here, validated for a selected number of experimental SACs, is general and can be applied for a preliminary screening of the HER activity of any catalyst made by supported single atoms, as well as of homogeneous catalysts based on coordination compounds.

### 5.2.2 Computational details

Spin polarized DFT calculations have been performed with the VASP 6.2.0[95–97] code using the generalized gradient approximation as formulated in the Perdew–Burke–Ernzerhof (PBE) functional.[19] Dispersion contributions have been introduced using the D3 Grimme's correction.[378]

The valence electrons, H (1s), C (2s,2p), N (2s, 2p), S (3s, 3p), Mo (4p, 5s, 4d), Sc (4s, 3d), Ti (4s, 3d), V (4s, 3d), Cr (4s, 3d), Mn (4s, 3d), Fe (4s, 3d), Co (4s, 3d), Ni (4s, 3d), Cu (4s, 3d), W (6s, 5d) Pd (5s, 4d), and Pt (6s, 5d), have been expanded into a set of plane waves with a kinetic cutoff of 400 eV, whereas the core electrons were treated with the projector augmented wave approach.[250,251] The truncation criteria for electronic and ionic loops were set to $10^{-6}$ eV and $10^{-3}$ eV/Å, respectively. In all cases where graphene is the support a 5×5×1 Monkhorst−Pack k-point grid was used;[254] for $MoS_2$ we reduced the k-point sampling mesh to the gamma point 1×1×1.

The hydrogen evolution reaction (HER) has been studied on first row transition metal (M) atoms either free (unsupported) or stabilized on solid surfaces: M adsorbed on N-graphene (M/N-Gr where the symbol / indicates adsorption on the surface) (4x4 supercell); M replacing a C atom of N-graphene (M@N-Gr where the symbol @ indicates incorporation of the M atom in the graphene lattice), (4×4 supercell); a graphene model with 3N atoms that coordinate the M atom replacing a C atom (M@3N-Gr) (4×4 supercell); a M atom adsorbed on a molybdenum disulfide layered compound (M/$MoS_2$) (6×6 supercell).

### 5.2.3 Modelling of HER on metal surfaces

Before to present the new kinetic model for HER on SACs, the basic features of the original model are briefly summarized. In standard conditions, the change of Gibbs free energy, $\Delta G^0$, for the semi-reaction $2\ H^+ + 2\ e^- \rightarrow H_2$ is equal to zero. Thus, the potential needed to promote the reaction is also zero, since $\Delta G^0 = - nFE^0$, where $n$ is the number of electrons involved, $F$ the Faraday's constant, and $E^0$ is the reduction potential. However, in catalytic processes this is true only in principle, since an extra potential - the overpotential h - is required for the reaction to occur; in the original model, it is assumed that h = 0, an approximation that has been subject of intense work in the last few years. When a proton is reduced on a metal catalyst, the next reaction occurs (Volmer step):

$$\mathrm{H^+ + e^- + M \rightleftarrows MH} \qquad \text{Eq. (18)}$$

where M is a metal site, and MH denotes an adsorbed H atom on the surface.
In this simple reaction, $\Delta G^0_H$ can differ from zero. In particular, if the H atom is strongly bound to the surface $\Delta G^0_H < 0$; *vice versa*, if H is weakly bound then $\Delta G^0_H > 0$. Now, in order to form $H_2$ the reaction can follow two different mechanisms. The first one is called Heyrovsky reaction, which involves the direct reduction of the second proton on the same metal site, i.e.:

$$\mathrm{MH} + \mathrm{H^+} + \mathrm{e^-} \rightarrow \mathrm{M} + \mathrm{H_2} \qquad \text{Eq. (19)}$$

The second path involves the Tafel reaction, where two H atoms bound to two different metal sites can combine:

$$2\ \mathrm{MH} \rightarrow 2\mathrm{M} + \mathrm{H_2} \qquad \text{Eq. (20)}$$

Usually the two paths occur in parallel, *i.e.* both are relevant, and their predominance depends on the H coverage.[416,417] Once the $H_2$ molecule forms, it can weakly bind to the surface thanks to dispersion forces. However, the physisorbed intermediate is almost at the same energy of the separated systems, M + $H_2$,[418,419] and it is fully justified to ignore this minimum in the overall thermochemistry of the reaction. This also means that the overpotential can be simply described by $\Delta G^0_H$, either following Volmer-Heyrovsky (VH) or Volmer-Tafel (VT) mechanisms. This behavior was described by Trasatti making use of a volcano curve where the exchange current, $i_0$, of HER on different metal catalysts is plotted against the strength of the M-H bond, the exchange current is proportional to the amount of $H_2$ produced.[420]
In their seminal paper, Nørskov and co-workers provided a link between the empirical observations and the atomistic calculation of the H adsorption free energy under the basic assumption that every reaction barrier other than thermochemistry is neglected.[380] The approach consists in evaluating the adsorption energy of an H atom on a metal ($\Delta E_H$) computed with respect to the clean surface M and gas-phase $H_2$:

$$\Delta E_H = E_{MH} - \left(E_M + \frac{E_{H_2}}{2}\right) \qquad \text{Eq. (21)}$$

Then, it is possible to calculate the change of Gibbs free energy as:

$$\Delta G^0{}_H = \Delta E_H + \Delta E_{ZPE} - \mathrm{T}\Delta S^0{}_H \qquad \text{Eq. (22)}$$

Here, $\Delta E_{ZPE}$ is the zero-point energy correction, and $\Delta S^0_H$ is the entropy variation of the reaction at standard conditions, usually approximated as $\Delta S^0_H \approx -\frac{S^0_{H_2}}{2}$. $\Delta G^0_H$ varies with the H coverage,[421] but this dependence is usually neglected. Irrespective of the Volmer-Heyrovsky or Volmer-Tafel mechanisms for $H_2$ evolution, the relation between exchange current $i_0$ and $\Delta G^0_H$ can be represented as a volcano plot, Figure 40(a). This can be analytically derived by solving the kinetic equations under the steady-state approximation for the MH reaction intermediate.[422] For simplicity, the equations are reported at pH = 0. This leads to two working equations for VH (Eq. 23), and VT (Eq. 24) paths, at standard conditions:

$$Log(i_0) = Log\left(-2ek_{VH}\frac{e^{\frac{\Delta G^0{}_H}{2k_bT}}}{1+e^{\frac{\Delta G^0{}_H}{k_bT}}}\right) = Log(i^{VH}_{max}) + Log\left(\frac{e^{\frac{\Delta G^0{}_H}{2k_bT}}}{1+e^{\frac{\Delta G^0{}_H}{k_bT}}}\right). \quad \text{Eq. (23)}$$

$$Log(i_0) = Log\left(-2ek_{VT}\left(\frac{e^{\frac{\Delta G^0{}_H}{2k_bT}}}{1+e^{\frac{\Delta G^0{}_H}{k_bT}}}\right)^2\right) = Log(i^{VT}_{max}) + Log\left(\left(\frac{e^{\frac{\Delta G^0{}_H}{2k_bT}}}{1+e^{\frac{\Delta G^0{}_H}{k_bT}}}\right)^2\right) \quad \text{Eq. (24)}$$

$k_{VH}$ and $k_{VT}$ are the kinetic constants of the VH and VT paths respectively. The top of the volcano plot, Figure 38(a), corresponds to $\Delta G^0{}_H = 0$; the left side of the plot is associated to metal surfaces that bind H too strongly, and the right side to metals that bind H too weakly. The best condition consists in a metal that binds H neither too strongly nor too weakly, as in this case the required overpotential h tends to zero, making the reaction favorable.

This means that the prediction of the activity of any metal catalyst in HER can be deduced simply from the adsorption energy of an H atom on that metal surface, i.e. by evaluating $\Delta G^0_H$, hence the overpotential h. This strategy has been widely and successfully applied in several computational studies of HER on metal surfaces.[423–425]

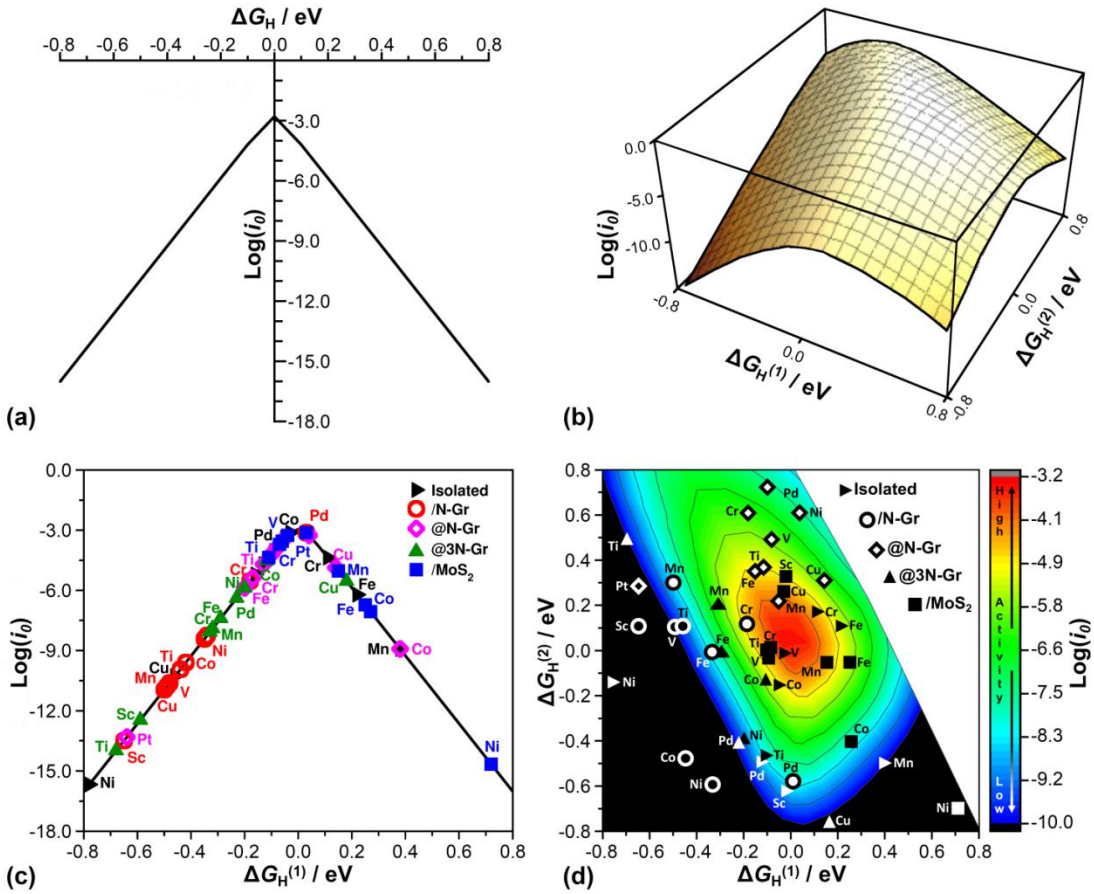


**Figure 40.** (a) Two-dimensional volcano plot for HER reaction assuming the formation of a MH intermediate (classical kinetic model); (b) three-dimensional volcano plot for HER reaction assuming the formation of MH and HMH intermediates (new kinetic model proposed here); (c) two-dimensional volcano plot derived from numerical DFT results for the case of HER reaction on 55 SACs computed assuming the formation of a single MH intermediate; and (d) three-dimensional volcano plot derived from numerical DFT results for the case of HER reaction on 55 SACs assuming the formation of MH and HMH intermediates. Red: high activity; blue: low activity. When $Log(i_0) < -10$ (extremely low activity) the color is black. In panels (c) and (d) are only reported the intermediates having both, $\Delta G_H^{(1)}$ and $\Delta G_H^{(2)}$ between -0.8 eV and 0.8 eV. [426]

### 5.2.4 Modelling of HER on single atom catalysts (SAC)

The approach described above, derived for an extended metal surface, has been applied so far in its original formulation also to the case of SACs. However, SACs, isolated metal atoms anchored on a support, can behave quite differently from an atom of a metal surface. As we mentioned in the introduction, transition metal

atoms surrounded by ligands are at the core of coordination chemistry and several examples have been reported where a single transition metal (TM) atom can bind and coordinate two H atoms, forming HMH complexes.[412–415,427,428] In the respect, the Volmer step on SACs, *i.e.* the formation of the MH surface complex, Eq. (18), can be followed by the addition of a second H atom with formation of a stable HMH intermediate. This introduces a new step in the process, with the consequence that the kinetic equations describing the evolution of $H_2$ become considerably more complex. The exchange current in this case depends on two variables instead of one:

i) the free energy change for the adsorption of the first H atom ($\Delta G^0{}_{H^{(1)}}$), as in the conventional kinetics of metal surfaces:

$$\mathrm{H^+ + e^- + M \rightleftarrows MH} \quad \text{(MH formation)} \qquad \text{Eq. (25)}$$

ii) the free energy change for the adsorption of the second H atom ($\Delta G^0{}_{H^{(2)}}$):

$$\mathrm{H^+ + e^- + M \rightleftarrows HMH} \quad \text{(HMH formation)} \qquad \text{Eq. (26)}$$

Furthermore, the third reaction step, $H_2$ evolution:

$$\mathrm{HMH \rightarrow M + H_2} \quad (H_2 \text{ evolution}) \qquad \text{Eq. (27)}$$

is also a function of $\Delta G^0{}_{H^{(1)}}$ and $\Delta G^0{}_{H^{(2)}}$, because the overall reaction 2 $H^+$ + 2 $e^- \rightarrow H_2$ is thermoneutral in standard conditions. This leads to:

$$\Delta G^0_{H^{(3)}} = \Delta G^0_{H^{(1)}} + \Delta G^0_{H^{(2)}} \qquad \text{Eq. (28)}$$

Solving the kinetic equations using the same approximations done to for the case of metal surfaces (see Kinetics of HER in the supporting information of the paper published on JACS), one obtains the following expression for the exchange current $i_0$:

$$\begin{aligned} &Log(i_0) \\ &= Log(i_{max}) \\ &+ Log\left(\frac{e^{\frac{\left(\Delta G^0{}_{H^{(1)}} + \Delta G^0{}_{H^{(2)}}\right)}{2k_bT}}}{1 + e^{\frac{\Delta G^0{}_{H^{(1)}}}{k_bT}} + e^{\frac{\left(\Delta G^0{}_{H^{(1)}} + \Delta G^0{}_{H^{(2)}}\right)}{k_bT}} + e^{\frac{\Delta G^0{}_{H^{(1)}}}{2k_bT}} + e^{\frac{\Delta G^0{}_{H^{(2)}}}{2k_bT}} + e^{-\frac{\Delta G^0{}_{H^{(1)}}}{2k_bT}}}\right) \end{aligned} \qquad \text{Eq. (29)}$$

Interestingly, the exchange current is still described by a volcano plot, Figure 40(b), where the maximum current occurs when both; $\Delta G^0{}_{H^{(1)}}$ and $\Delta G^0{}_{H^{(2)}}$ are close to zero, *i.e.* the formation of H adsorbates is thermoneutral.

In this respect, the key requirements for a good HER catalyst are unchanged. However, in the case of HER on SACs two formation energies, and not just $\Delta G^0{}_{H^{(1)}}$, determine the overall performance of the catalyst.

Of course, as we mentioned above, if the rate determining step of the reaction is the formation of the first intermediate, MH, one recovers the typical two-dimensional volcano plot of the standard model, Figure 40(a). However, if the second intermediate is sufficiently stable, the overall kinetics cannot be described by one variable. So far, this possibility has not been considered in previous studies. In the next sections is provided some numerical examples based on first principles calculations of the different conclusions that can be reached if one neglects the formation of the HMH intermediate using the classical one-variable model, its also reported a benchmark of the proposed model against available experimental measurements.

#### 5.2.4.1 Experimental benchmark

Here is reported a validation of the proposed kinetic model by comparing the predicted behavior of DFT calculations with experiment for a few selected cases. This kind of comparisons is far from simple because the results from DFT calculations can be compared to experiment only if the structure of the active SAC is the same. While the structure is defined at atomistic level in the calculations, this is not always the case in experiment. Electron microscopy, X-ray spectroscopies (XANES and EXAFS), high resolution STEM, infrared spectroscopy of adsorbed probe molecules, etc., often in combination, can provide essential information and sometime unambiguous identification of the structure of the catalyst.[429] More often, the nature of the SAC is only partly elucidated, making a direct comparison with DFT problematic. The second aspect is the dynamical behavior of SACs under reactive conditions.[430,431] The local coordination and position of a SAC can change in the course of the reaction depending on the oxidizing or reducing environmental conditions.[432] A third problem is that often the catalyst contains small aggregates beside SACs, and the overall activity can be due to a combination of active sites. A fourth problem is that DFT total energies are affected by intrinsic errors,[433] as reaction free energies depend on the details of the calculation (exchange-correlation functional, size of the supercell, nature of the pseudopotential, treatment of dispersion, etc.). Finally, we have seen above that recent work has shown the importance of other effects like the applied overpotential[434–436] and the interaction with the solvent.[437] Taking into account all these aspects, four representative experimental studies for a total of six catalysts

where the nature of the SAC has been clearly identified, so that a comparison with DFT calculations is meaningful.

The comparison is based on a key physical quantity in HER, the overpotential $\eta$, as the absolute value of the exchange current, $i_0$, depends on a kinetic constant which is unknown. The overpotential $\eta$ match with the absolute value of free energy of the reaction, $|\Delta G_H|$; if the reaction occurs in one step, $\eta = |\Delta G_H^{(1)}| / e$; and if two steps are involved, MH and HMH intermediates, $\eta = |\Delta G_H^{(1)} + \Delta G_H^{(2)}| / ne$, where $n$ is the number of electrons involved (2 in this case).

The first example of the computational procedure followed here considers the case of a Co atom stabilized at N-doped graphene, where Co is located on a carbon vacancy and coordinated to three N atoms, Co@3N-Gr (see Figure 41), a system which has been studied both theoretically and experimentally.[405,438,439]

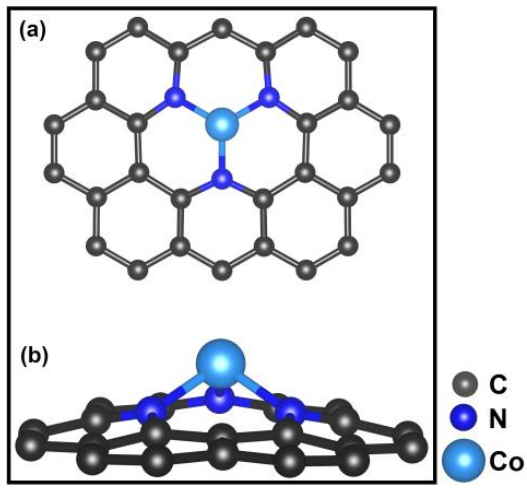


**Figure 41.** (a) top and (b) side view of Co@3N-Gr. Black, dark blue, and light blue balls represent the carbon, nitrogen, and cobalt atoms, respectively. [426]

Figures 42(a-c) report the structures of the CoH@3N-Gr and HCoH@3N-Gr complexes, respectively. The H---H distance in HCoH is of 0.90 Å, indicating the formation of an activated $H_2$ molecule, a precursor state of $H_2$ desorption.[440,441] Both calculated H-H (0.90 Å) and Co-H (1.56 Å) bond lengths for the Co@3N-Gr SAC compare very well with those reported for an experimentally isolated Co dihydrogen complex (0.86 Å and 1.57 Å respectively, derived from DFT calculations[442]), Figure 42(d).

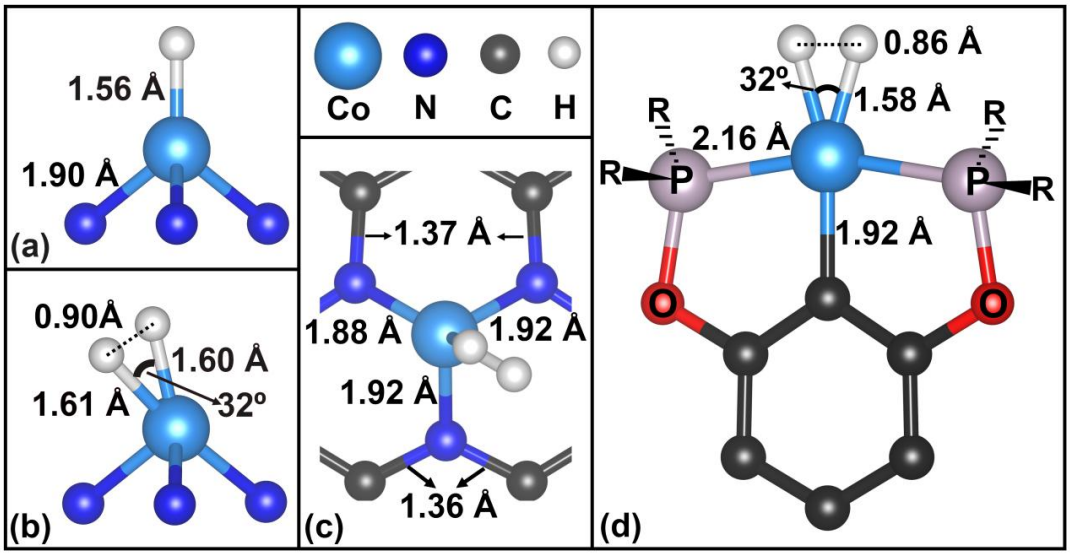


**Figure 42.** (a) side view of CoH@3N-Gr intermediate, (b) side and (c) top views of the HCoH@3N-Gr dihydrogen intermediate (DFT calculations); in (a) and (b) the (3N-Gr) support is not reported for clarity. (d) side view of a Co dihydrogen coordination compound isolated experimentally; the geometry reported has been obtained from DFT calculations of the new complex.[442] Selected distances and angles are reported. [426]

It is interesting to compare the predicted HER activity for Co@3N-Gr with the experimental results of Fei et al., who reported a high activity for this catalyst.[438,443] For each path, one- or two-intermediates, we have calculated the exchange current and the $\Delta G_H$ values using the equations reported above. The measured overpotential (0.15-0.18 eV)[444] is well reproduced using both a kinetic model based on a single intermediate ($\Delta G_H^{(1)}$= -0.12 eV) or on two intermediates ($\Delta G_H^{(2)}$= -0.15 eV). Thus, this is a case where the formation of the dihydrogen complex does not alter the conclusions obtained with the original model since both steps have $\Delta G_H \approx 0$. However, this is not a representative example, and in other cases quite different results are obtained with the two procedures.

The second case is that of Co atoms supported on $MoS_2$, Co/$MoS_2$. Usually, TM atoms are incorporated into the lattice of $MoS_2$ replacing a Mo cation;[445,446] when this occurs, the activity of the surface S atoms near the TM ion changes and results in good HER activity (rather than SACs, these systems should be better classified as doped $MoS_2$). Recently, a system consisting of Co atoms supported on the surface of $MoS_2$ has been reported and an overpotential $\eta$ = 84 mV for the HER has been measured at 10 mA $cm^{-2}$.[447] High-angle annular dark-field STEM (HADDF-STEM) images indicate that the Co atoms adsorb on the Mo-top sites, thus this is the site considered in the calculations. If we use the classical model, $\Delta G_H^{(1)}$ = 340 meV ($\eta$ = 340 mV); when we consider also the second step, $\Delta G_H^{(2)}$ = -665 meV, we have $\Delta G_H^{(3)}$ = -324 eV and $\eta = |\Delta G_H| / 2$ = 162 mV (Figure 43).

This is consistent with Co/$MoS_2$ being a catalyst with a very low overpotential for HER. Notice that if we assume that the Co atom is on the hollow site of $MoS_2$ instead of on-top of Mo, the corresponding overpotentials are $\eta$ = 269 mV (one step) and $\eta$ = 59 mV (two steps): also in this case Co is predicted to be an efficient catalyst and the agreement with experiment is quantitative.

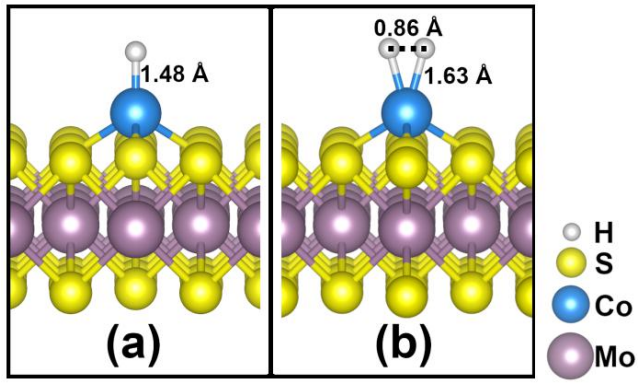


**Figure 43.** Optimized structures of (a) CoH/$MoS_2$ and (b) HCoH/$MoS_2$ complexes. [426]

The third example deals with Ni atoms trapped at defective graphene, Ni@D-Gr. In this atomically dispersed catalyst, Ni atom is stabilized at a C-divacancy and its coordinated to four C atoms in a square planar geometry, as shown HADDF-STEM and XANES measurements.[448] The catalyst exhibits an overpotential of 70 mV at 10 mA $cm^{-2}$. Simulating Ni@D-Gr as in previous cases, one can obtain overpotentials of $\eta$ = 464 mV with the classical model, and $\eta$ = 197 mV with the two-steps model. While the two-H model is more or less consistent with experiment (197 mV versus 70 mV) the single step model is completely inconsistent (464 mV versus 70 mV).

The final example deals with TM atoms stabilized at N-doped graphene (M@4N-Gr). In a recent study has been synthesized and characterized three catalysts adsorbed on a C-divacancy and coordinated to 4 N-atoms, M@4N-Gr (M = Co, Ni, and W).[405] The three catalysts have been selected based on DFT calculations that showed that Co@4N-Gr is expected to be much more active in HER than Ni@4N-Gr and W@4N-Gr. Using the classical model, in fact, the DFT overpotentials predicted in ref. [405] are 130 mV for Co, and 930 mV and 1620 mV for W and Ni.[405] According to these values, only Co@4N-Gr should be active, while W@4N-Gr and in particular Ni@4N-Gr should be totally inert. The measured overpotentials at 10 mA $cm^{-2}$ however are 230 mV (Co), 530 mV (W) and 590 mV (Ni),[405] showing that all three catalysts may be active, with Co exhibiting the lowest overpotential. We have computed $\eta$ for Co@4N-Gr, Ni@4N-Gr, and W@4N-Gr catalysts with the two kinetic models, Figure 44. With the classical model we obtain $\eta$ = 162 mV (Co), $\eta$ = 882 mV (W) and $\eta$ = 1614 mV (Ni), the same DFT values reported in ref 405.

However, when also the HMH complex is considered, the computed overpotentials are 257 mV for Co, and 439 mV for W, in quantitative agreement with the experiment (230 meV and 530 meV, respectively).[405] Quite interesting is the case of Ni, since here neither dihydride nor dihydrogen complexes form. The adsorption of a second H leads to a $H_2$ molecule weakly physisorbed, Figure 44(d). This is a typical case where the conventional one step model is valid. This also means that the computed overpotential for Ni is $\eta$ = 1614 mV, in agreement with the theoretical value reported in ref. [405], but in contrast with the measured overpotential of 590 mV. We can only speculate that the structure of the Ni catalyst is probably different from that considered here, but more work is required to clarify this point.

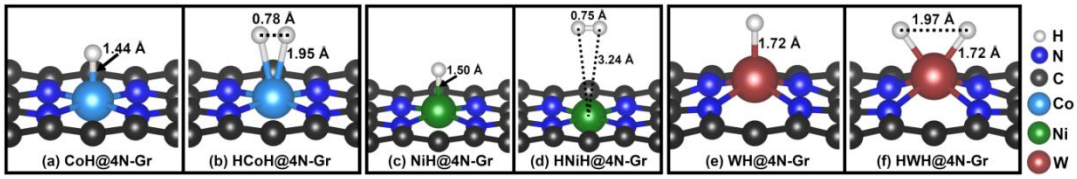


**Figure 44.** Optimized structures of (a) CoH@4N-Gr, (b) HCoH@4N-G, (c) NiH@4N-G, (d) HNiH@4N-G, (e) WH@4N-G, and (f) HWH@4N-G complexes. [426]

Overall, the new model accounts for the features observed experimentally and provide a better agreement with the experimental data than the classical one-step model. The results have been obtained using the PBE exchange-correlation functional. In order to assess the importance of this choice on the final results, the analysis for M@4N-Gr has been repeated using the PBESOL and revPBE functionals. While differences of up to 250 meV are found in the adsorption energies, the same general conclusions are obtained with the three functionals: the HMH model improves the agreement with experiments for Co@4N-Gr and W@4N-Gr, while for Ni@4N-Gr no model (MH or HMH) provides a good result, suggesting that the Ni catalyst occupies a different site.

#### 5.2.4.2 Formation of two-hydrogen complexes on SACs

To assess the role of two-hydrogen HMH complexes in the prediction of the catalytic activity of SACs, DFT calculations have been performed on a larger series of model systems: (a) isolated, gas-phase TM atoms (M, from Sc to Cu, Pd and Pt); (b) the same group of atoms adsorbed on N-doped graphene, M/N-Gr; (c) M atoms replacing a C atom in N-doped graphene, M@N-Gr; (d) M atoms replacing a C atom in graphene doped by three N atoms (pyridinic), M@3N-Gr; and (e) M atoms adsorbed on $MoS_2$, M/$MoS_2$. In this way a hypothetical set of 55 systems to model the HER on SACs is generated.

For each system we have considered the activity as predicted (I) by the classical one-intermediate model, and (II) by the new two-intermediates model (formation of HMH complexes).

In most cases the adsorption of two H atoms on the 55 models of SACs results in the formation either of dihydride or of dihydrogen complexes. In particular, all the isolated TM atoms considered lead to the classical dihydride species, characterized by long H---H distances (from 1.75 to 3.25 Å) and short M-H distances, see Figure 45, consistent with matrix-isolation experiments.[449]

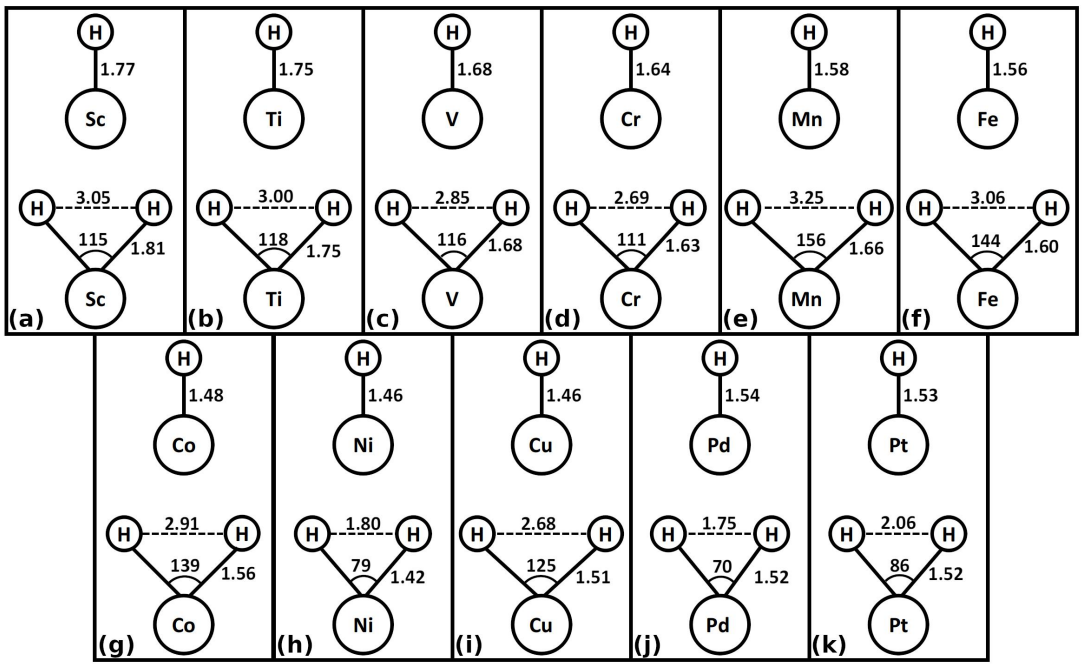


**Figure 45**. Schematic view of the MH and HMH intermediates on free M atoms. Bond lengths are reported in Å, bond angles in degrees (º). (a) ScH, HScH; (b) TiH, HTiH; (c) VH, HVH; (d) CrH, HCrH; (e) MnH, HMnH; (f) FeH, HFeH; (g) CoH, HCoH; (h) NiH, HNiH; (i) CuH, HCuH; (j) PdH, HPdH; and (k) PtH, HPtH. [426]

For M atoms adsorbed on N-Gr, M/N-Gr, only Co, Ni, and Pd form dihydrogen complexes, the rest give rise to dihydride species. When the metal atoms are incorporated in N-Gr, M@N-Gr, we found four cases of dihydrogen species (Ti, Cr, Mn, Fe), the rest being dihydrides; for M@3N-Gr the dihydrogen complexes form in the case of Mn, Fe, Co, Ni, and Cu, while when the metal atoms are supported on $MoS_2$ the majority of SACs form dihydrogen species (Ti, V, Cr, Mn, Fe, Co, Ni, Cu, and Pd), see Figure 46.

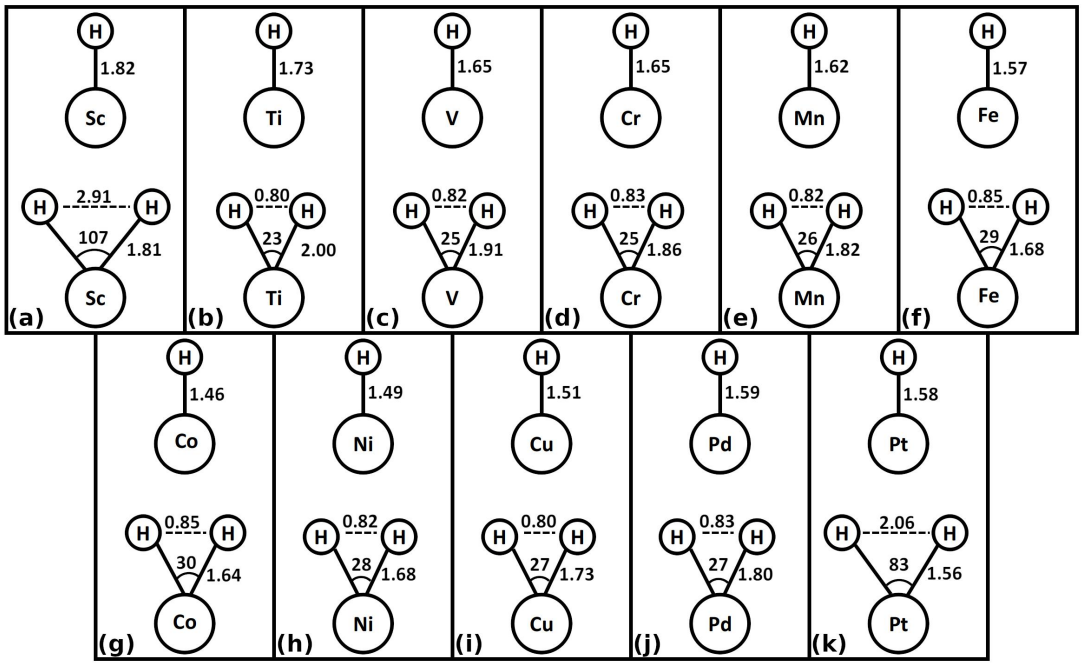


**Figure 46.** Schematic view of the $MH/MoS_2$ and $HMH/MoS_2$ intermediates. The bond lengths and angles are reported in Å and degrees (º), respectively. (a) $HSc/MoS_2$, $HScH/MoS_2$; (b) $TiH/MoS_2$, $HTiH/MoS_2$; (c) $VH/MoS_2$, $HVH/MoS_2$; (d) $CrH/MoS_2$, $HCrH/MoS_2$; (e) $MnH/MoS_2$, $HMnH/MoS_2$; (f) $FeH/MoS_2$, $HFeH/MoS_2$; (g) $CoH/MoS_2$, $HCoH/MoS_2$; (h) $NiH/MoS_2$, $HNiH/MoS_2$; (i) $CuH/MoS_2$, $HCuH/MoS_2$; (j) $PdH/MoS_2$, $HPdH/MoS_2$; and (k) $PtH/MoS_2$, $HPtH/MoS_2$. [426]

The reasons for the formation of dihydride or dihydrogen complexes have been widely discussed for organometallic complexes and depend on the nature of the ligands - electron donor species favor dihydride, electron attractor ligands favor dihydrogen. This is apparent if one compares free, unsupported, and $MoS_2$-supported transition metal atoms: the free metal atoms have sufficient electron density to break the $H_2$ molecule so that only dihydride complexes are formed; on $MoS_2$ the bonding of M with three electronegative S atoms reduces the electron density and the dihydrogen complexes dominate. An efficient descriptor is the d-band center; for the case of a single H atom adsorption on $M/MoS_2$ it has been shown that a linear correlation exists between the position of the $d_z^2$ orbital of M and the strength of the M-H bond.[450]

One might wonder why, if dihydride or dihydrogen complexes on SACs are predicted to exist by DFT calculations, they have not been observed. Actually, a few examples of metal atoms on surfaces binding two H atoms are known, although their relevance for HER has not been recognized so far. Well documented cases of transition metal atom anchored on a silica surface that bind more than one H atom have been reported by Basset and coworkers, $[\equiv SiO)_2ZrH_2]$, $[\equiv SiO)WH_3(Me)_2]$, and $[\equiv SiO)_2TaH_3]$.[451–454]

Recently, combining inelastic neutron scattering and infrared spectroscopy, the formation of a dihydrogen complex has been demonstrated for Cu ions coordinated to a zeolite framework.[455] The coexistence of dihydride and dihydrogen species has been reported for the Ru atoms of the $RuO_2$(110) surface based on HREELS measurements and DFT calculations.[456] The formation of dihydrogen and multi-hydrogen complexes has been observed in DFT calculations on the HER of Pt atoms on N-Gr,[390] $MoS_2$,[457] onion-like carbon nanospheres,[458] defective graphene and h-BN,[459] although their relevance for the kinetics of the process has not been fully appreciated. More difficult is the observation of HMH complexes on SACs stabilized on metal oxides, as here a tendency towards the spillover of one of the H atoms to the surface, with formation of MH and OH species, has been reported.[460,461] Of course, the fact that HMH species can form on SACs, does not necessarily means that these can also be observed in real samples at room temperature. The majority of cases studied show a positive $H_2$ desorption energy, i.e. an endothermic process, but this ranges from a few tens of an eV for many complexes up to 2.86 eV for the case of HPtH@3N-Gr. Using a Redhead equation for first-order desorption processes,[462] $\Delta E_{des} = RT_{des} [\ln(\nu T_{des}) - 3.64]$, and assuming a pre-factor $\nu = 10^{13}$ $s^{-1}$, one can estimate that thermal desorption of $H_2$ from HMH is possible for temperatures above 300 K only if $\Delta E > 0.8$ eV. This condition is fulfilled for a few cases: for M/N-Gr, Sc, Co, Ni, Pd, Pt (0.94 eV, 1.40 eV, 1.47 eV, 0.98 eV, and 1.58 eV, respectively); for M@N-Gr and M/$MoS_2$ only Pt (0.89 eV and 1.86 eV, respectively); for M@3N-Gr, V, Ni, Cu, Pd, and Pt (0.87 eV, 1.08 eV, 1.09 eV, 1.19 eV, and 2.86 eV, respectively). When stable dihydrogen or dihydride complexes form, they can be detected using neutron diffraction, or spectroscopic techniques such as $^1$H NMR and IR, Figure 47.[427]

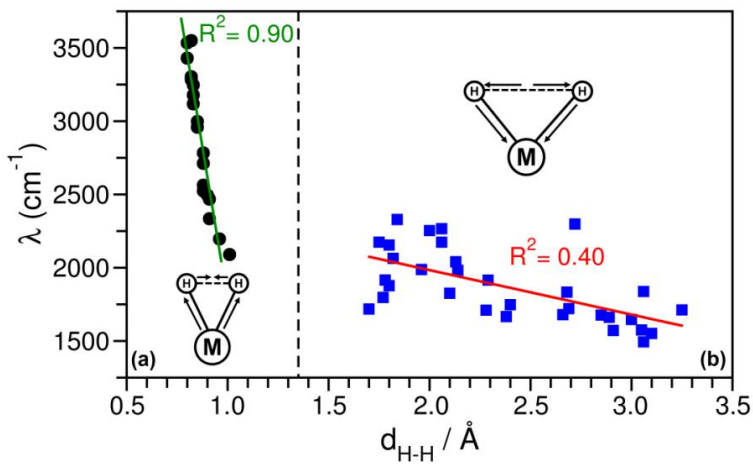


**Figure 47.** Correlation between the vibrational frequency (H-H, or M-H), and the H-H distance for the various HMH complexes considered in this work. The distinct feature of dihydrogen (a) and dihydride (b) complexes provides a fingerprint of the nature of the HMH complex. [426]

### 5.2.4.3 Comparison of kinetics based on one or two intermediates

Having discussed the formation, nature and stability of the HMH complexes for the 55 SAC models, we consider now their impact on the kinetics of HER. Using the original Nørskov' model, the plot of the exchange current vs $\Delta G_H^{(1)}$ results in the classical two-dimensional volcano plot, see Figure 40(c); on the other hand, if one considers the adsorption of two H atoms on the catalytic center, the exchange current is plotted against $\Delta G_H^{(1)}$ and $\Delta G_H^{(2)}$, resulting in a three-dimensional volcano plot, see Figure 40(d).

Both models lead to a volcano-type behavior, but the two volcano plots cannot be directly compared, being described by a different number of variables. Thus, we introduce a common descriptor of the efficiency of a given catalyst, defined as the ratio of the exchange current, $i_0$, and the maximum exchange current, $i_{max}$ (corresponding to the top of volcano curve). If the logarithm of $i_0/i_{max}$ is close to zero, then the SAC has an exchange current close to the top of volcano curve, hence maximum efficiency. On the contrary, when the exchange current is low, $\mathrm{Log}(i_0/i_{max})$ is a negative number. In this way, we can directly compare the efficiency predicted by the two kinetic models. In Figure 48 we report a periodic table where the atoms investigated are color coded: red corresponds to the most active SACs, blue or black to the most inactive ones; and green corresponds to a weak activity. The results are shown for all the studied cases.

Figure 48(a,I) refers to the predicted activity based on the classical MH intermediate model for isolated metal atoms; the same for the two-intermediate models is shown in Figure 48(a,II). The inclusion of the HMH intermediate in the kinetics leads to a drastic reduction in the number of "good" catalysts: with model I Sc, Ti, V, Cr, Fe, Co, and Pd are predicted to be good catalysts for HER, Figure 48(a,I), while with model II only V, Cr, Fe, and Co exhibit high exchange currents, Figure 48(a,II). This is because in the first case the condition $\Delta G_H^{(1)} \sim 0$ eV is sufficient to guarantee high efficiency, while in the second one also the condition $\Delta G_H^{(2)} \sim 0$ eV needs to be satisfied. Notice that even in Figure 48(a,II) there are metal atoms (e.g. Co) satisfying the ideal conditions for HER, i.e. $\Delta G_H^{(1)} \sim 0$ eV and $\Delta G_H^{(2)} \sim 0$ eV.

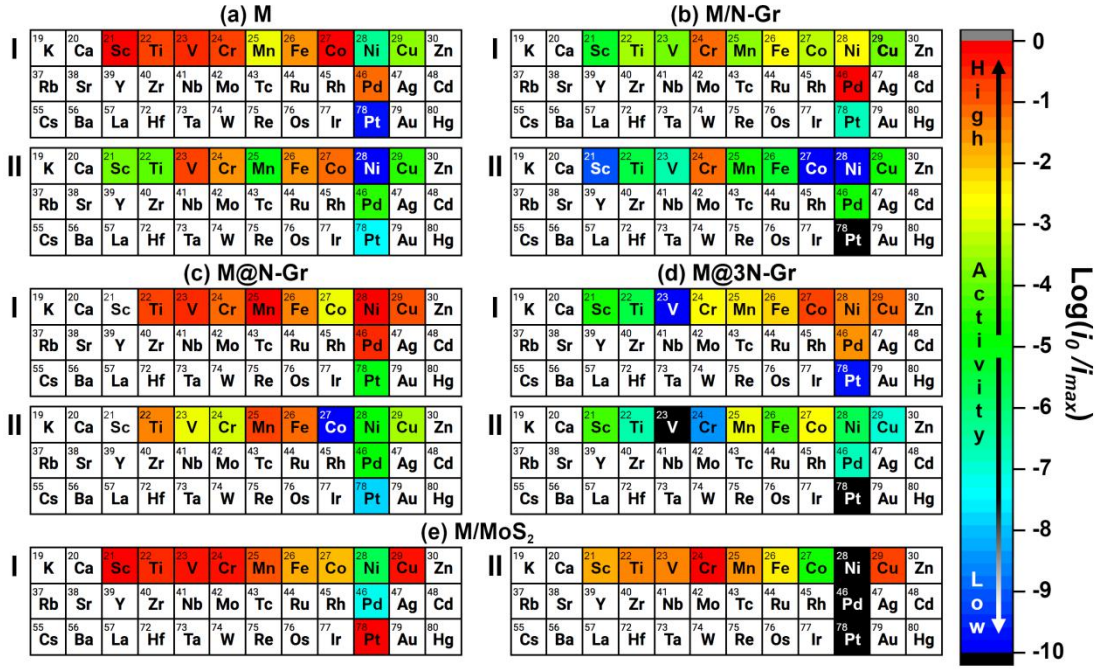


**Figure 48.** Predicted efficiency for the HER reaction for 55 models of SACs. (a) free M atoms, M; and (b) M atoms adsorbed on N-Gr, M/N-Gr; (c) M atoms incorporated on N-Gr, M@N-Gr; (d) M atoms incorporated on 3N-Gr, M@3N-Gr; and (e) M atoms adsorbed on $MoS_2$, M/$MoS_2$. (I) classical model based on a single MH intermediate; (II) model based on both MH and HMH intermediates (two-hydrogens complex). The color refers to the ratio of the exchange current $i_0$ for a given atom and the maximum exchange current, $i_{max}$, and provides a visual measure of the expected HER activity. The best catalysts (in red) have Log($i_0/i_{max}$) close to zero; the worse catalysts (in blue) have Log($i_0/i_{max}$) close to -10. Atoms are coloured in black when Log($i_0/i_{max}$) < -10. On Sc@N-Gr the HMH complex does not form; only the one-intermediate model can be applied. [426]

The second model correspond to M adsorbed on N-Gr, M/N-Gr; when the model I is considered (MH intermediate only), Cr and Pd exhibit high currents, Figure 48(b,I), while when also HMH intermediates is considered (model II) the picture changes, with only Cr as good catalyst, Figure 48(b,II). The next two cases are that of the M atoms incorporated on N-doped graphene with the graphitic and pyridinic configuration.[463,464] In the first one, a carbon atom of the lattice is replaced by a N atom (N-Gr), M@N-Gr; and in the second, three C atoms are replaced by N atoms (3N-Gr), M@3N-Gr. In both cases the M atoms are stabilized at a C vacancy. When the model I is considered (MH intermediate only), Ti, V, Cr, Mn, Fe, Co, Ni, Cu, and Pd on N-Gr exhibit high currents, Figure 48(c,I), while when also HMH intermediates are considered (model II) the picture changes, with only Ti, Mn, and Fe still characterized by good performances, Figure 48(c,II).

A similar trend is found for the M atoms stabilized on 3N-Gr, Figure 48(d). Using model I all SACs, with the exception of Sc, Ti, V and Pt are predicted to be active, with particularly high efficiency for Co, Ni, Cu and Pd, Figure 48(d,I); on the contrary,

much lower efficiencies are expected with model II, Figure 48(d,II), with only Mn and Co still exhibiting a good HER activity.

The last SACs considered consists of M atoms supported on a $MoS_2$ monolayer. The metal atoms have been adsorbed in a hollow site above three sulfur atoms, as recently suggested experimentally.[465] For some atoms, e.g. Pt, the preferred position is on-top of Mo[465] and indeed, different results are obtained for the HER depending on the adsorption site. Given the model character of our calculations, for the discussion we consider only the hollow site. Also in this case, going from the single MH intermediate (model I) to that based on MH and HMH intermediates (model II) the number of good SACs predicted by theory is considerably reduced. In the first case all the atoms with the exception of Ni and Pd have very high exchange currents, Figure 48(e,I), while in the refined model only Sc, Ti, V, Cr, Mn, and Cu are still very effective and satisfy simultaneously the condition $\Delta G_H^{(1)}$ ~0 eV and $\Delta G_H^{(2)}$ ~0 eV, Figure 48(e,II). For all other SACs the expected activity is decreased by some orders of magnitude.

#### 5.2.4.4 Beyond Nørskov' model

The volcano plots discussed above represent a simple yet valuable tool to screen electrode materials for electrocatalytic processes. They are based on the combination of linear scaling relations with Sabatier's principle and the Brønsted–Evans–Polanyi approach[466] which links thermodynamics to kinetics. The volcano's apex corresponds to a material that binds the reaction intermediates neither too strongly nor too weekly at zero overpotential $\eta$ (i.e. $\Delta G = 0$ at $\eta = 0$). In this respect, the original model of Nørskov and coworkers,[380] extended here to the special case of SACs, identifies the potential catalysts for which $\Delta G = 0$ at $\eta = 0$. It is entirely based on a thermodynamic approach, while kinetic effects due to the presence of reaction barriers or to the applied overpotential are not included. Recently, several authors have addressed this limitation showing that there are deviations to the original model if the effect of the applied overpotential is explicitly taken into account.[434–436,467] In particular, the most active electrocatalysts bind the reaction intermediate species with $\Delta G > 0$ for $\eta \neq 0$. This corresponds to a shift of the apex of the volcano plot of the order of 200 meV, which means that electrocatalysts that bind weakly to the surface rather than forming thermoneutral bonds can be active and should be considered as potentially good candidates.[435,436] This shows that for a quantitative assessment of the performance of an electrocatalyst, the effect of the overpotential, although small ($\approx$0.2 eV), must be included.

Another aspect that is usually neglected in the modeling of materials for electrocatalysis is the solvation energy contribution, given by the interaction of the chemical intermediates with the solvent.[437,468] In principle, *ab initio* molecular dynamics studies can address this problem,[469] but they are computationally very demanding. Recently, approximated but computationally amenable recipes have been proposed to account for solvation based on microsolvation models.[470] Furthermore, the combined effect of the applied overpotential and of the solvent can affect the morphology of the surface or induce surface reconstructions.

To assess the importance of these terms, we have introduced the effect of the solvent on the formation of MH and HMH intermediates for Co@4N-Gr, Ni@4N-G and W@4N-Gr, using the implicit solvent approach where the water molecules are replaced by a continuum dielectric. The MH and HMH formation energies, $\Delta E^{(1)}$ and $\Delta E^{(2)}$, respectively, change by -0.03/-0.04 eV only after inclusion of the solvent.

Finally, HER reactions are also pH dependent.[471] Nevertheless, in most cases the experimentally observed behavior of HER catalysts in variable pH conditions are rationalized based on DFT calculations where the pH is not explicitly taken into account.[472,473] The pH contribution to the Gibbs free energy can be included by considering a term of the type $k_b$Tln(10)pH, as reported by Nørskov and co-workers.[474,475] Of course, one issue that remains open is the stability of the MH and HMH complexes in strong acid or basic conditions, but this is something the goes beyond the simple model to predict the HER activity.

This brief discussion shows that substantial progresses have been done in recent years in the study of reactions at electrode surfaces with DFT approaches. The Nørskov's model has been used extensively in the past and will most likely continue to be used due to its simplicity. It provides a rapid screening of potentially useful catalysts at low computational cost, thus allowing to examine large sets of new materials. What should be stressed in the present context, is that things are quite different, and more complex when one moves from extended metal surfaces to single atom catalysts. As we have discussed above, the possible formation of dihydrogen and dihydride complexes results in new intermediates not considered in the original model. The formation of these intermediates can significantly alter the thermodynamics and the kinetics of the process, resulting in $\Delta G$ values that can differ by 1 eV or more from those obtained with the one H model. In this respect, the effects that we are discussed in this paper for SACs can dominate over other important, but quantitatively less relevant terms such as the role of the solvent and of the overpotential.

### 5.2.5 Summary

In this sub-chapter, we have shown that the predicted HER activity of isolated transition metal atoms supported on a solid surface, often referred to as single atoms catalysts (SACs), cannot be predicted with the standard model[380] based on the assumption that the MH complex is the only intermediate, as for HER on metal electrodes. SACs, that can be considered analogs of coordination compounds, bind hydrogen differently and can form two-hydrogen intermediates, HMH, not present on metal surfaces. The HMH intermediate is a precursor of the $H_2$ desorption step that should be taken into account in the kinetics of the process. We have extended the kinetic model proposed by Nørskov and coworkers to the case where this second intermediate forms; the resulting HER activity, as measured by the exchange current, is described by a three-dimensional volcano plot as the reaction now depends on two free energies of H adsorption instead of one. According to this new model the condition for the best catalyst as measured by the exchange current $i_0$ is that both $\Delta G^0_{H^{(1)}}$ and $\Delta G^0_{H^{(2)}}$ are close to zero, *i.e.* that the formation of H adsorbates is thermoneutral. Recent work has shown that a rigid shift of about 200 meV of the apex in a volcano curve occurs when the applied overpotential is included in the analysis.[434–436] Nevertheless, screening studies based on the standard approach provide a first assessment of the performances of a potential new catalyst. In case of SACs we have shown based on DFT calculations that stable dihydride and dihydrogen complexes form in many cases, and that neglecting this reaction step may result in completely different and often too optimistic predictions of the catalytic activity of SACs in HER.

# Conclusions

In this thesis, we have first introduced a method to characterize high correlated transition metal oxides (TMOs) as are MnO, FeO, CoO, NiO and CuO, which pose several problems due to their highly correlated nature. To do this we introduced a different approach (Charge Transition Levels, CTLs) based on the assumption that the band gap in some TMOs can have partial Mott-Hubbard character, and can be defined as the energy associated to the process: $M^{m+}(3d^n) + M^{m+}(3d^n) \rightarrow M^{(m+1)+}(3d^{n-1}) + M^{(m-1)+}(3d^{n+1})$. The band gap is thus associated to the removal (ionization potential, I) and addition (electron affinity, A) of one electron to an ion of the lattice. From this study it was found that CTLs provides a better description of the band gap of highly correlated materials than those obtained with a hybrid functional and high level of theory methods (GW, DMFT), where the values obtained with this approach are close to the experimental measurements.

Next, we studied the description and rationalization of the role of quantum confinement in the group III-V semiconductor thin films and nanostructures by studying (110) surfaces of each semiconductor (AlP, AlAs, AlSb, GaP, GaAs, GaSb, InP, InAs, and InSb). The results indicate that when the quantum confinement is strong, it mainly affects the position of the Conduction Band Minimum (CBM) of the semiconductor, while the Valence Band Maximum (VBM) is almost insensitive to the system's size. The results can be rationalized in terms of electron and hole effective masses, and the slabs results can be generalized to other cases of quantum confinement such as quantum dots, overcoming the need of an explicit consideration and calculation of the properties of semiconductor nanoparticles.

In a dedicated chapter we provide some examples of heterojunctions and we have discerned the methodological aspect that should be considered in the design of new heterojunctions. In particular in all the studies, effort was given to the description of different type-II heterojunctions, since only these kind of junctions are favorable for the separation of photogenerated electrons and holes and are used in photocatalysis. From these studies it was found that the use of hybrid functionals or

other self-interaction corrected functionals is recommended since this guarantees a good description of the two (or more) components in the junction. It is important to mention that different models can be adopted to determine the band alignment and in some cases, the use of the simple “independent units” model is sufficient to predict the band alignment. But in cases where the chemical nature of the interfaces is important, the “alternating slabs junction” or the “surface terminated junction” models are needed since they describe more accurately the properties of the components.

In a specific sub-chapter attention was given to the interface between InP and $TiO_2$, which is a system with applications in photocatalysis and solar cells. To do this the effect of the $TiO_2$ surface in contact with the InP and also the thickness dependence of $TiO_2$ covering InP have been considered. With this, we found that irrespective of the anatase $TiO_2$ surface in contact with InP, (101) or (001), the system behaves as a type-II junction, where the $TiO_2$ band edges are lower in energy than the InP ones, providing a rationalization for the observed electron-hole separation (migration of photogenerated electrons from InP to $TiO_2$, consistently with the experimental observation). From the role of the $TiO_2$ thickness, it was found that a favorable type-II junction is retained for every thickness of the titania passivating film.

In the last chapter of this thesis we have described two cases of co-catalysts, both based on single atom catalyst for the hydrogen evolution reaction. First, the results of a collaboration with the group of Prof. In-Hwan Lee from the Korea University describe the role of different gold particles size (single atoms, SAs; nanocluster, NCs; and nanoparticles, NPs) supported in nitrogen-doped graphene for the hydrogen generalization. It was found that the photocatalyst performance follows the following order; Au NCs/N-Gr > Au SAs/N-Gr > Au NPs/N-Gr > N-Gr, respectively. These performances were attributed to two effects: (a) the strong surface plasmon resonance stimulated by light absorption and charge transferred near the surface of Au NCs, where the N-Gr conductive support can prolong the plasmon-produced hot electrons and direct the light-to-hydrogen conversion; and (b) the intrinsic binding capability of the H on the different supports.

In the last part of the thesis an extension of the Nørskov model was proposed starting form the idea that SACs can present the same behavior of coordination compounds, which is the formation of dihydride or dihydrogen complexes on the metal center (HMH intermediates). With this the formation of stable HMH intermediates was observed, in addition to the MH one considered in the original model. This may change the kinetics of the process for SACs and in some cases the Nørskov model can be insufficient to describe the hydrogen evolution reaction on SACs. According to this new model the condition for the screening of the best catalyst for the HER may depends on how close to zero is the exchange current i0 measured from the free energy of the MH and HMH intermediates.

# References


1 M. R. Hoffmann, S. T. Martin, W. Choi and D. W. Bahnemann, *Chem. Rev.*, 1995, **95**, 69–96.

2 S. H. Mohr, J. Wang, G. Ellem, J. Ward and D. Giurco, *Fuel*, 2015, **141**, 120–135.

3 R. Schlögl, *Angew. Chemie Int. Ed.*, 2003, **42**, 2004–2008.

4 S. Dey and N. S. Mehta, *Resour. Environ. Sustain.*, 2020, **2**, 100006.

5 A. Fujishima and K. Honda, *Nature*, 1972, **238**, 37–38.

6 A. Kubacka, M. Fernández-García and G. Colón, *Chem. Rev.*, 2012, **112**, 1555–1614.

7 J. Low, J. Yu, M. Jaroniec, S. Wageh and A. A. Al-Ghamdi, *Adv. Mater.*, 2017, **29**, 1601694.

8 H. Wang, L. Zhang, Z. Chen, J. Hu, S. Li, Z. Wang, J. Liu and X. Wang, *Chem. Soc. Rev.*, 2014, **43**, 5234–5244.

9 G. Di Liberto, L. A. Cipriano, S. Tosoni and G. Pacchioni, *Chem. – A Eur. J.*, 2021, **27**, 13306–13317.

10 R. L. Anderson, *IBM J. Res. Dev.*, 1960, **4**, 283–287.

11 U. Diebold, *Surf. Sci. Rep.*, 2003, **48**, 53–229.

12 J. P. Perdew, W. Yang, K. Burke, Z. Yang, E. K. U. Gross, M. Scheffler, G. E. Scuseria, T. M. Henderson, I. Y. Zhang, A. Ruzsinszky, H. Peng, J. Sun, E. Trushin and A. Görling, *Proc. Natl. Acad. Sci.*, 2017, **114**, 2801–2806.

13 K. T. Butler, C. H. Hendon and A. Walsh, *Faraday Discuss.*, 2017, **201**, 207–219.

14 H. Yu, J. Li, R. A. Loomis, L.-W. Wang and W. E. Buhro, *Nat. Mater.*, 2003, **2**, 517–520.

15 J. Heyd and G. E. Scuseria, *J. Chem. Phys.*, 2004, **121**, 1187–1192.

16 A. J. Garza and G. E. Scuseria, *J. Phys. Chem. Lett.*, 2016, **7**, 4165–4170.

17 T. Das, G. Di Liberto, S. Tosoni and G. Pacchioni, *J. Chem. Theory Comput.*, 2019, **15**, 6294–6312.

18 S. Körbel, M. A. L. Marques and S. Botti, *J. Mater. Chem. C*, 2016, **4**, 3157–3167.

19 J. P. Perdew, K. Burke and M. Ernzerhof, *Phys. Rev. Lett.*, 1996, **77**, 3865–3868.

20 M. Gerosa, C. E. Bottani, L. Caramella, G. Onida, C. Di Valentin and G. Pacchioni, *Phys. Rev. B*, 2015, **91**, 1–15.

21 J. H. Skone, M. Govoni and G. Galli, *Phys. Rev. B*, 2014, **89**, 195112.

22 M. Gerosa, C. E. Bottani, C. Di Valentin, G. Onida and G. Pacchioni, *J. Phys. Condens. Matter*, 2017, **30**, 44003.

23 C. G. Van de Walle and R. M. Martin, *Phys. Rev. B*, 1987, **35**, 8154–8165.

24 L. Weston, H. Tailor, K. Krishnaswamy, L. Bjaalie and C. G. Van de Walle, *Comput. Mater. Sci.*, 2018, **151**, 174–180.

25 A. Baldereschi, S. Baroni and R. Resta, *Phys. Rev. Lett.*, 1988, **61**, 734–737.

26 E. Cerrato, C. Gionco, M. C. Paganini, E. Giamello, E. Albanese and G. Pacchioni, *ACS Appl. Energy Mater.*, 2018, **1**, 4247–4260.

27 J. Tersoff, *Phys. Rev. B*, 1984, **30**, 4874–4877.

28 J. Tersoff, *Phys. Rev. B*, 1985, **32**, 6968–6971.

29 J. Yu, J. Low, W. Xiao, P. Zhou and M. Jaroniec, *J. Am. Chem. Soc.*, 2014, **136**, 8839–8842.

30 A. Alkauskas, P. Broqvist, F. Devynck and A. Pasquarello, *Phys. Rev. Lett.*, 2008, **101**, 106802.

31 J. C. Conesa, *J. Phys. Chem. C*, 2012, **116**, 18884–18890.

32 J. E. Castellanos Águila, P. Palacios, J. C. Conesa, J. Arriaga and P. Wahnón, *Comput. Mater. Sci.*, 2016, **121**, 79–85.

33 J. E. Castellanos-Águila, L. Lodeiro, E. Menéndez-Proupin, A. L. Montero-Alejo, P. Palacios, J. C. Conesa and P. Wahnón, *ACS Appl. Mater. Interfaces*, 2020, **12**, 44648–44657.

34 K. T. Butler, G. Sai Gautam and P. Canepa, *npj Comput. Mater.*, 2019, **5**, 19.

35 S.-H. Wei and A. Zunger, *Appl. Phys. Lett.*, 1998, **72**, 2011–2013.

36 J. R. Waldrop, S. P. Kowalczyk, R. W. Grant, E. A. Kraut and D. L. Miller, *J. Vac. Sci. Technol.*, 1981, **19**, 573–575.

37 D. O. Scanlon, C. W. Dunnill, J. Buckeridge, S. A. Shevlin, A. J. Logsdail, S. M. Woodley, C. R. A. Catlow, M. J. Powell, R. G. Palgrave, I. P. Parkin, G. W. Watson, T. W. Keal, P. Sherwood, A. Walsh and A. A. Sokol, *Nat. Mater.*, 2013, **12**, 798–801.

38 P. Kalisman, Y. Nakibli and L. Amirav, *Nano Lett.*, 2016, **16**, 1776–1781.

39 Y. Yamada, S. Shikano and S. Fukuzumi, *J. Phys. Chem. C*, 2013, **117**, 13143–13152.

40 S. Liu and Y.-J. Xu, *Nanoscale*, 2013, **5**, 9330–9339.

41 S. Fukuzumi, Y. Yamada, T. Suenobu, K. Ohkubo and H. Kotani, *Energy Environ. Sci.*, 2011, **4**, 2754–2766.

42 S. Fukuzumi and Y. Yamada, *J. Mater. Chem.*, 2012, **22**, 24284–24296.

43 D. Ma, J.-W. Shi, Y. Zou, Z. Fan, X. Ji, C. Niu and L. Wang, *Nano Energy*, 2017, **39**, 183–191.

44 V. Subramanian, E. E. Wolf and P. V Kamat, *J. Am. Chem. Soc.*, 2004, **126**, 4943–4950.

45 R. Su, R. Tiruvalam, A. J. Logsdail, Q. He, C. A. Downing, M. T. Jensen, N. Dimitratos, L. Kesavan, P. P. Wells, R. Bechstein, H. H. Jensen, S. Wendt, C. R. A. Catlow, C. J. Kiely, G. J. Hutchings and F. Besenbacher, *ACS Nano*, 2014, **8**, 3490–3497.

46 S. Cao, Y. Chen, L. Kang, Z. Lin and W.-F. Fu, *J. Mater. Chem. A*, 2015, **3**, 18711–18717.

47 Y. Yamada, T. Miyahigashi, H. Kotani, K. Ohkubo and S. Fukuzumi, *Energy Environ. Sci.*, 2012, **5**, 6111–6118.

48 X.-J. Lv, S.-X. Zhou, C. Zhang, H.-X. Chang, Y. Chen and W.-F. Fu, *J. Mater. Chem.*, 2012, **22**, 18542–18549.

49 L. Sun, B. Åkermark and S. Ott, *Coord. Chem. Rev.*, 2005, **249**, 1653–1663.

50 J. Yang, D. Wang, H. Han and C. Li, *Acc. Chem. Res.*, 2013, **46**, 1900–1909.

51 Á. Morales-García, R. Valero and F. Illas, *J. Phys. Chem. C*, 2017, **121**, 18862–18866.

52 P. S. Bagus, F. Illas, G. Pacchioni and F. Parmigiani, *J. Electron Spectros. Relat. Phenomena*, 1999, **100**, 215–236.

53 J. Muscat, A. Wander and N. M. Harrison, *Chem. Phys. Lett.*, 2001, **342**, 397–401.

54 V. I. Anisimov, J. Zaanen and O. K. Andersen, *Phys. Rev. B*, 1991, **44**, 943–954.

55 S. Dudarev and G. Botton, *Phys. Rev. B*, 1998, **57**, 1505–1509.

56 A. D. Becke, *J. Chem. Phys.*, 1993, **98**, 5648–5652.

57 A. D. Becke, *J. Chem. Phys.*, 1993, **98**, 1372–1377.

58 P. Mori-Sánchez, A. J. Cohen and W. Yang, *J. Chem. Phys.*, 2006, **125**, 201102.

59 A. J. Cohen, P. Mori-Sánchez and W. Yang, *Chem. Rev.*, 2012, **112**, 289–320.

60 C. Adamo and V. Barone, *J. Chem. Phys.*, 1999, **110**, 6158–6170.

61 F. Corà, M. Alfredsson, G. Mallia, D. S. Middlemiss, W. C. Mackrodt, R. Dovesi, and R. Orlando Structure and bonding, Springer, Berlin, Heidelberg, 2004, **113**, 171-232.

62 J. Heyd, G. E. Scuseria and M. Ernzerhof, *J. Chem. Phys.*, 2003, **118**, 8207–8215.

63 J. Heyd, G. E. Scuseria and M. Ernzerhof, *J. Chem. Phys.*, 2006, **124**, 219906.

64 S. J. Clark and J. Robertson, *Phys. Rev. B*, 2010, **82**, 85208.

65 J. Paier, M. Marsman, K. Hummer, G. Kresse, I. C. Gerber and J. G. Ángyán, *J. Chem. Phys.*, 2006, **124**, 154709.

66 C. Di Valentin and G. Pacchioni, *Acc. Chem. Res.*, 2014, **47**, 3233–3241.

67 F. Fuchs, J. Furthmüller, F. Bechstedt, M. Shishkin and G. Kresse, *Phys. Rev. B*, 2007, **76**, 115109.

68 F. Gygi and A. Baldereschi, *Phys. Rev. Lett.*, 1989, **62**, 2160–2163.

69 V. Fiorentini and A. Baldereschi, *Phys. Rev. B*, 1995, **51**, 17196–17198.

70 M. A. L. Marques, J. Vidal, M. J. T. Oliveira, L. Reining and S. Botti, *Phys. Rev. B*, 2011, **83**, 1–5.

71 T. Shimazaki and Y. Asai, *Chem. Phys. Lett.*, 2008, **466**, 91–94.

72 P. Liu, C. Franchini, M. Marsman and G. Kresse, *J. Phys. Condens. Matter*, 2019, **32**, 15502.

73 J. E. Moussa, P. A. Schultz and J. R. Chelikowsky, *J. Chem. Phys.*, 2012, **136**, 204117.

74 P. Deák, Q. Duy Ho, F. Seemann, B. Aradi, M. Lorke and T. Frauenheim, *Phys. Rev. B*, 2017, **95**, 75208.

75 N. F. Mott, *Proc. Phys. Soc. Sect. A*, 1949, **62**, 416–422.

76 S. Lany, *Phys. Rev. B*, 2013, **87**, 85112.

77 L. Hedin, *Phys. Rev.*, 1965, **139**, A796--A823.

78 A. Georges, G. Kotliar, W. Krauth and M. J. Rozenberg, *Rev. Mod. Phys.*, 1996, **68**, 13–125.

79 J. Hubbard, *Proc. R. Soc. Lond. A*, 1963, **276**, 238–257.

80 J. Zaanen, G. A. Sawatzky and J. W. Allen, *Phys. Rev. Lett.*, 1985, **55**, 418–421.

81 S. Lany and A. Zunger, *Phys. Rev. B*, 2008, **78**, 235104.

82 C. G. de Walle, *Phys. Rev. Lett.*, 2000, **85**, 1012–1015.

83 C. G. de Walle and J. Neugebauer, *J. Appl. Phys.*, 2004, **95**, 3851–3879.

84 A. Janotti and C. G. Van de Walle, *Nat. Mater.*, 2007, **6**, 44–47.

85 J. F. Janak, *Phys. Rev. B*, 1978, **18**, 7165–7168.

86 A. Alkauskas, P. Broqvist and A. Pasquarello, *Phys. Rev. Lett.*, 2008, **101**, 46405.

87 A. Alkauskas, P. Broqvist and A. Pasquarello, *Phys. Status Solidi Basic Res.*, 2011, **248**, 775–789.

88 P. Broqvist, A. Alkauskas and A. Pasquarello, *Phys. Rev. B*, 2009, **80**, 85114.

89 A. Alkauskas and A. Pasquarello, *Phys. B Condens. Matter*, 2007, **401–402**, 670–673.

90 A. Chakrabarty and C. H. Patterson, *J. Chem. Phys.*, 2012, **137**, 54709.

91 F. Gallino, G. Pacchioni and C. Di Valentin, *J. Chem. Phys.*, 2010, **133**, 144512.

92 R. Dovesi, A. Erba, R. Orlando, C. M. Zicovich-Wilson, B. Civalleri, L. Maschio, M. Rérat, S. Casassa, J. Baima, S. Salustro and B. Kirtman, *Wiley Interdiscip. Rev. Comput. Mol. Sci.*, 2018, **8**, e1360.

93 L. A. Cipriano, G. Di Liberto, S. Tosoni and G. Pacchioni, *J. Chem. Theory Comput.*, 2020, **16**, 3786–3798.

94 F. Oba, A. Togo, I. Tanaka, J. Paier and G. Kresse, *Phys. Rev. B*, 2008, **77**, 245202.

95 G. Kresse and J. Hafner, *Phys. Rev. B*, 1994, **49**, 14251–14269.

96 G. Kresse and J. Hafner, *Phys. Rev. B*, 1993, **47**, 558–561.

97 G. Kresse and J. Furthmüller, *Comput. Mater. Sci.*, 1996, **6**, 15–50.

98 J. P. Perdew and M. Levy, *Phys. Rev. Lett.*, 1983, **51**, 1884–1887.

99 J. P. Perdew, M. Ernzerhof and K. Burke, *J. Chem. Phys.*, 1996, **105**, 9982–9985.

100 E. Z. Kurmaev, R. G. Wilks, A. Moewes, L. D. Finkelstein, S. N. Shamin and J. Kuneš, *Phys. Rev. B*, 2008, **77**, 165127.

101 J. Kuneš, V. I. Anisimov, S. L. Skornyakov, A. V Lukoyanov and D. Vollhardt, *Phys. Rev. Lett.*, 2007, **99**, 156404.

102 L. Zhang, P. Staar, A. Kozhevnikov, Y.-P. Wang, J. Trinastic, T. Schulthess and H.-P. Cheng, *Phys. Rev. B*, 2019, **100**, 35104.

103 E. Engel and R. N. Schmid, *Phys. Rev. Lett.*, 2009, **103**, 36404.

104 T. Kotani, *J. Phys. Condens. Matter*, 1998, **10**, 9241–9261.

105 C. Rödl, F. Fuchs, J. Furthmüller and F. Bechstedt, *Phys. Rev. B*, 2009, **79**, 235114.

106 C. Rödl, F. Sottile and L. Reining, *Phys. Rev. B*, 2015, **91**, 45102.

107 S. Kobayashi, Y. Nohara, S. Yamamoto and T. Fujiwara, *Phys. Rev. B*, 2008, **78**, 155112.

108 H. Jiang, R. I. Gomez-Abal, P. Rinke and M. Scheffler, *Phys. Rev. B*, 2010, **82**, 45108.

109 S. V Faleev, M. van Schilfgaarde and T. Kotani, *Phys. Rev. Lett.*, 2004, **93**, 126406.

110 H. V. Thang, E. Albanese and G. Pacchioni, *J. Phys. Condens. Matter*, 2019, **31**, 145503.

111 T. Shimazaki and T. Nakajima, *Phys. Chem. Chem. Phys.*, 2016, **18**, 27554–27563.

112 M. Ferrero, M. Rérat, B. Kirtman and R. Dovesi, *J. Chem. Phys.*, 2008, **129**, 244110.

113 M. Ferrero, M. Rérat, R. Orlando, R. Dovesi and I. J. Bush, *J. Phys. Conf. Ser.*, 2008, **117**, 12016.

114 M. Ferrero, M. Rérat, R. Orlando and R. Dovesi, *J. Comput. Chem.*, 2008, **29**, 1450–1459.

115 R. W. G. Wyckoff, *The structure of cystals*, 1934.

116 A. Werner and H. D. Hochheimer, *Phys. Rev. B*, 1982, **25**, 5929–5934.

117 M. F. Peintinger, D. V. Oliveira and T. Bredow, *J. Comput. Chem.*, 2013, **34**, 451–459.

118 A. K. Cheetham and D. A. O. Hope, *Phys. Rev. B*, 1983, **27**, 6964–6967.

119 W. L. Roth, *Phys. Rev.*, 1958, **110**, 1333–1341.

120 K. V Rao and A. Smakula, *J. Appl. Phys.*, 1965, **36**, 2031–2038.

121 G. A. Sawatzky and J. W. Allen, *Phys. Rev. Lett.*, 1984, **53**, 2339–2342.

122 R. J. Powell and W. E. Spicer, *Phys. Rev. B*, 1970, **2**, 2182–2193.

123 T. D. Kang, H. S. Lee and H. Lee, *J. Korean Phy. Soc.*, 2007, **50**, 632.

124 M. O'Keeffe, *J. Chem. Phys.*, 1963, **39**, 1789–1793.

125 B. K. Meyer, A. Polity, D. Reppin, M. Becker, P. Hering, P. J. Klar, T. Sander, C. Reindl, J. Benz, M. Eickhoff, C. Heiliger, M. Heinemann, J. Bläsing, A. Krost, S. Shokovets, C. Müller and C. Ronning, *Phys. status solidi B, 2012,* **249**, 8, 1487-1509.

126 J. N. Plendl, L. C. Mansur, S. S. Mitra and I. F. Chang, *Solid State Commun.*, 1969, **7**, 109–111.

127 G. Kugel, C. Carabatos, B. Hennion, B. Prevot, A. Revcolevschi and D. Tocchetti, *Phys. Rev. B*, 1977, **16**, 378–385.

128 B. Prévot, J. Biellmann, M. F. Meftah and M. Sieskind, *Phys. status solidi*, 1977, **40**, 503–510.

129 F. Tran, P. Blaha, K. Schwarz and P. Novák, *Phys. Rev. B*, 2006, **74**, 155108.

130 M. Alfredsson, G. David Price, C. R. A. Catlow, S. C. Parker, R. Orlando and J. P. Brodholt, *Phys. Rev. B*, 2004, **70**, 165111.

131 D. C. Khan and R. A. Erickson, *Phys. Rev. B*, 1970, **1**, 2243–2249.

132 M. Heinemann, B. Eifert and C. Heiliger, *Phys. Rev. B*, 2013, **87**, 115111.

133 J. van Elp, R. H. Potze, H. Eskes, R. Berger and G. A. Sawatzky, *Phys. Rev. B*, 1991, **44**, 1530–1537.

134 J. van Elp, J. L. Wieland, H. Eskes, P. Kuiper, G. A. Sawatzky, F. M. F. de Groot and T. S. Turner, *Phys. Rev. B*, 1991, **44**, 6090–6103.

135 J. Ghijsen, L. H. Tjeng, J. van Elp, H. Eskes, J. Westerink, G. A. Sawatzky and M. T. Czyzyk, *Phys. Rev. B*, 1988, **38**, 11322–11330.

136 I. A. Drabkin, L. T. Emel'yanova, R. N. Iskenderov and Y. M. Ksendzov, *Fiz. Tverd. Tela*.

137 H. K. Bowen, D. Adler and B. H. Auker, *J. Solid State Chem.*, 1975, **12**, 355–359.

138 Y. Wang, S. Lany, J. Ghanbaja, Y. Fagot-Revurat, Y. P. Chen, F. Soldera, D. Horwat, F. Mücklich and J. F. Pierson, *Phys. Rev. B*, 2016, **94**, 245418.

139 F. Marabelli, G. B. Parravicini and F. Salghetti-Drioli, *Phys. Rev. B*, 1995, **52**, 1433–1436.

140 D. E. Aspnes and A. A. Studna, *Phys. Rev. B*, 1983, **27**, 985–1009.

141 S. Adachi, *GaAs and Related Materials, Bulk Semiconducting and Superlattice Properties*, World Scientific, 1994.

142 M. Razeghi, *Nature*, 1994, **369**, 631–633.

143 A. P. Alivisatos, *J. Phys. Chem.*, 1996, **100**, 13226–13239.

144 B. Bennett and R. Soref, *IEEE J. Quantum Electron.*, 1987, **23**, 2159–2166.

145 J. A. del Alamo, *Nature*, 2011, **479**, 317–323.

146 B. Mandl, J. Stangl, E. Hilner, A. A. Zakharov, K. Hillerich, A. W. Dey, L. Samuelson, G. Bauer, K. Deppert and A. Mikkelsen, *Nano Lett.*, 2010, **10**, 4443–4449.

147 I. Vurgaftman, J. R. Meyer and L. R. Ram-Mohan, *J. Appl. Phys.*, 2001, **89**, 5815–5875.

148 J. Singh, *Semiconductors Devices, Basic Principles*, John Willey & Sons, 1st edn., 2000.

149 J. Qiu, G. Zeng, M.-A. Ha, B. Hou, M. Mecklenburg, H. Shi, A. N. Alexandrova and S. B. Cronin, *Chem. Mater.*, 2015, **27**, 7977–7981.

150 J. Qiu, G. Zeng, M.-A. Ha, M. Ge, Y. Lin, M. Hettick, B. Hou, A. N. Alexandrova, A. Javey and S. B. Cronin, *Nano Lett.*, 2015, **15**, 6177–6181.

151 S. Hu, M. R. Shaner, J. A. Beardslee, M. Lichterman, B. S. Brunschwig and N. S. Lewis, *Science*

*(80-. ).*, 2014, **344**, 1005–1009.

152 G. Zeng, J. Qiu, Z. Li, P. Pavaskar and S. B. Cronin, *ACS Catal.*, 2014, **4**, 3512–3516.

153 Y. Lin, R. Kapadia, J. Yang, M. Zheng, K. Chen, M. Hettick, X. Yin, C. Battaglia, I. D. Sharp, J. W. Ager and A. Javey, *J. Phys. Chem. C*, 2015, **119**, 2308–2313.

154 G. Zeng, J. Qiu, B. Hou, H. Shi, Y. Lin, M. Hettick, A. Javey and S. B. Cronin, *Chem. – A Eur. J.*, 2015, **21**, 13502–13507.

155 X. Yin, C. Battaglia, Y. Lin, K. Chen, M. Hettick, M. Zheng, C.-Y. Chen, D. Kiriya and A. Javey, *ACS Photonics*, 2014, **1**, 1245–1250.

156 J. Qiu, G. Zeng, P. Pavaskar, Z. Li and S. B. Cronin, *Phys. Chem. Chem. Phys.*, 2014, **16**, 3115–3121.

157 G. Di Liberto, S. Tosoni and G. Pacchioni, *ChemCatChem*, 2020, **12**, 2097–2105.

158 G. Di Liberto, S. Tosoni and G. Pacchioni, *J. Phys. Chem. Lett.*, 2019, **10**, 2372–2377.

159 G. Di Liberto, S. Tosoni and G. Pacchioni, *J. Phys. Condens. Matter*, 2019, **31**, 434001.

160 G. Di Liberto, S. Tosoni and G. Pacchioni, *Phys. Chem. Chem. Phys.*, 2019, **21**, 21497–21505.

161 Á. Morales-García, R. Valero and F. Illas, *J. Chem. Theory Comput.*, 2017, **13**, 3746–3753.

162 K. C. Ko, S. T. Bromley, J. Y. Lee and F. Illas, *J. Phys. Chem. Lett.*, 2017, **8**, 5593–5598.

163 O. Lamiel-Garcia, A. Cuko, M. Calatayud, F. Illas and S. T. Bromley, *Nanoscale*, 2017, **9**, 1049–1058.

164 A. J. Nozik and O. I. Mićić, *MRS Bull.*, 1998, **23**, 24–30.

165 O. I. Mićić, J. R. Sprague, C. J. Curtis, K. M. Jones, J. L. Machol, A. J. Nozik, H. Giessen, B. Fluegel, G. Mohs and N. Peyghambarian, *J. Phys. Chem.*, 1995, **99**, 7754–7759.

166 A. D. Yoffe, *Adv. Phys.*, 2001, **50**, 1–208.

167 K. Takei, H. Fang, S. B. Kumar, R. Kapadia, Q. Gao, M. Madsen, H. S. Kim, C.-H. Liu, Y.-L. Chueh, E. Plis, S. Krishna, H. A. Bechtel, J. Guo and A. Javey, *Nano Lett.*, 2011, **11**, 5008–5012.

168 A. D. Yoffe, *Adv. Phys.*, 1993, **42**, 173–262.

169 R. Dingle, *Confined carrier quantum states in ultrathin semiconductor heterostructures*, Advances in Solid State Physics, Springer, Berlin, Heidelberg, 1975, vol. 15.

170 M. V Rama Krishna and R. A. Friesner, *J. Chem. Phys.*, 1991, **95**, 8309–8322.

171 O. I. Mićić, S. P. Ahrenkiel and A. J. Nozik, *Appl. Phys. Lett.*, 2001, **78**, 4022–4024.

172 A. L. Efros and M. Rosen, *Annu. Rev. Mater. Sci.*, 2000, **30**, 475–521.

173 L. E. Brus, *J. Chem. Phys.*, 1984, **80**, 4403–4409.

174 J. Heyd, J. E. Peralta, G. E. Scuseria and R. L. Martin, *J. Chem. Phys.*, 2005, **123**, 174101.

175 J. E. Peralta, J. Heyd, G. E. Scuseria and R. L. Martin, *Phys. Rev. B*, 2006, **74**, 73101.

176 Y.-S. Kim, K. Hummer and G. Kresse, *Phys. Rev. B*, 2009, **80**, 35203.

177 Y.-S. Kim, M. Marsman, G. Kresse, F. Tran and P. Blaha, *Phys. Rev. B*, 2010, **82**, 205212.

178 J. Heyd, G. E. Scuseria and M. Ernzerhof, *J. Chem. Phys.*, 2006, **124**, 219906.

179 P. Pernot, B. Civalleri, D. Presti and A. Savin, *J. Phys. Chem. A*, 2015, **119**, 5288–5304.

180 C.-Y. Yeh, Z. W. Lu, S. Froyen and A. Zunger, *Phys. Rev. B*, 1992, **46**, 10086–10097.

181 S. Tomić, B. Montanari and N. M. Harrison, *Phys. E Low-dimensional Syst. Nanostructures*, 2008, **40**, 2125–2127.

182 M. Shishkin, M. Marsman and G. Kresse, *Phys. Rev. Lett.*, 2007, **99**, 246403.

183 F. Tran and P. Blaha, *Phys. Rev. Lett.*, 2009, **102**, 226401.

184 I. C. Gerber, J. G. Ángyán, M. Marsman and G. Kresse, *J. Chem. Phys.*, 2007, **127**, 54101.

185 H. Xiao, J. Tahir-Kheli and W. A. Goddard, *J. Phys. Chem. Lett.*, 2011, **2**, 212–217.

186 B. Monemar, *Phys. Rev. B*, 1973, **8**, 5711–5718.

187 H. C. Casey and M. B. Panish, *Heterostructure Lasers*, Academic Press, Inc,111 Fifth Avenue, New York, 1978.

188 R. W. R. Wyckoff, *Crystal Structures*, Interscience Publishers, New York, New York, 2nd edn., 1963.

189 A. K. Saxena, *Phys. status solidi*, 1981, **105**, 777–787.

190 M. R. Lorenz, G. D. Pettit and R. C. Taylor, *Phys. Rev.*, 1968, **171**, 876–881.

191 J. S. Blakemore, *J. Appl. Phys.*, 1982, **53**, R123–R181.

192 M. Wu and C. Chen, *J. Appl. Phys.*, 1992, **72**, 4275–4280.

193 P. Rochon and E. Fortin, *Phys. Rev. B*, 1975, **12**, 5803–5810.

194 J. van Laar, A. Huijser and T. L. van Rooy, *J. Vac. Sci. Technol.*, 1977, **14**, 894–898.

195 S. Zwerdling, W. H. Kleiner and J. P. Theriault, *J. Appl. Phys.*, 1961, **32**, 2118–2123.

196 M. Cardona, N. E. Christensen and G. Fasol, *Phys. Rev. B*, 1988, **38**, 1806–1827.

197 H. Q. Yang, T. L. Song, X. X. Liang and G. J. Zhao, *J. Phys. Conf. Ser.*, 2015, **574**, 12048.

198 Y. Wang, H. Yin, R. Cao, F. Zahid, Y. Zhu, L. Liu, J. Wang and H. Guo, *Phys. Rev. B*, 2013, **87**, 235203.

199 R. Braunstein and E. O. Kane, *J. Phys. Chem. Solids*, 1962, **23**, 1423–1431.

200 L. A. Cipriano, G. Di Liberto, S. Tosoni and G. Pacchioni, *Nanoscale*, 2020, **12**, 17494-17501.

201 W. A. Harrison, *Surf. Sci.*, 1976, **55**, 1–19.

202 J. Ihm, D. J. Chadi and J. D. Joannopoulos, *Phys. Rev. B*, 1983, **27**, 5119–5121.

203 M. D. Pashley, K. W. Haberern, W. Friday, J. M. Woodall and P. D. Kirchner, *Phys. Rev. Lett.*, 1988, **60**, 2176–2179.

204 D. J. Chadi, *Ultramicroscopy*, 1989, **31**, 1–9.

205 D. K. Biegelsen, R. D. Bringans, J. E. Northrup and L.-E. Swartz, *Phys. Rev. B*, 1990, **41**, 5701–5706.

206 Q. Xue, T. Hashizume, J. M. Zhou, T. Sakata, T. Ohno and T. Sakurai, *Phys. Rev. Lett.*, 1995, **74**, 3177–3180.

207 C. D. MacPherson, R. A. Wolkow, C. E. J. Mitchell and A. B. McLean, *Phys. Rev. Lett.*, 1996, **77**, 691–694.

208 C. B. Duke, *Chem. Rev.*, 1996, **96**, 1237–1260.

209 A. M. Frisch, W. G. Schmidt, J. Bernholc, M. Pristovsek, N. Esser and W. Richter, *Phys. Rev. B*, 1999, **60**, 2488–2494.

210 S. B. Zhang and A. Zunger, *Appl. Phys. Lett.*, 1997, **71**, 677–679.

211 S. Y. Tong, A. R. Lubinsky, B. J. Mrstik and M. A. Van Hove, *Phys. Rev. B*, 1978, **17**, 3303–3309.

212 D. J. Chadi, *Phys. Rev. B*, 1979, **19**, 2074–2082.

213 R. M. Feenstra, *Phys. Rev. B*, 1994, **50**, 4561–4570.

214 H. Ye, G. Chen, Y. Wu, Y. Zhu and S.-H. Wei, *Phys. Rev. B*, 2008, **78**, 193308.

215 B. Engels, P. Richard, K. Schroeder, S. Blügel, P. Ebert and K. Urban, *Phys. Rev. B*, 1998, **58**, 7799–7815.

216 J. L. A. Alves, J. Hebenstreit and M. Scheffler, *Phys. Rev. B*, 1991, **44**, 6188–6198.

217 G.-X. Qian, R. M. Martin and D. J. Chadi, *Phys. Rev. B*, 1988, **37**, 1303–1307.

218 S. Mankefors and P. O. Nilsson, *J. Phys. Condens. Matter*, 2001, **13**, 823–832.

219 C. Mailhiot, C. B. Duke and D. J. Chadi, *Surf. Sci.*, 1985, **149**, 366–380.

220 J. R. Chelikowsky, S. G. Louie and M. L. Cohen, *Phys. Rev. B*, 1976, **14**, 4724–4726.

221 G. Pellegrini, G. Mattei and P. Mazzoldi, *J. Appl. Phys.*, 2005, **97**, 73706.

222 U. Banin, Y. Cao, D. Katz and O. Millo, *Nature*, 1999, **400**, 542–544.

223 W. Liu, A. Y. Chang, R. D. Schaller and D. V Talapin, *J. Am. Chem. Soc.*, 2012, **134**, 20258–20261.

224 P. E. Lippens and M. Lannoo, *Phys. Rev. B*, 1989, **39**, 10935–10942.

225 J. Pérez-Conde and A. K. Bhattacharjee, *Solid State Commun.*, 1999, **110**, 259–264.

226 P. C. Sercel and K. J. Vahala, *Phys. Rev. B*, 1990, **42**, 3690–3710.

227 H. Fu, L.-W. Wang and A. Zunger, *Phys. Rev. B*, 1998, **57**, 9971–9987.

228 G. E. Tudury, M. V Marquezini, L. G. Ferreira, L. C. Barbosa and C. L. Cesar, *Phys. Rev. B*, 2000, **62**, 7357–7364.

229 A. Sills, P. Harrison and M. Califano, *J. Phys. Chem. Lett.*, 2016, **7**, 31–35.

230 J. L. Marín, R. Riera and S. A. Cruz, *J. Phys. Condens. Matter*, 1998, **10**, 1349–1361.

231 J. M. Ferreyra and C. R. Proetto, *Phys. Rev. B*, 1999, **60**, 10672–10675.

232 S. Baskoutas and A. F. Terzis, *J. Appl. Phys.*, 2006, **99**, 13708.

233 B. O'Regan and M. Grätzel, *Nature*, 1991, **353**, 737–740.

234 A. L. Linsebigler, G. Lu and J. T. Yates, *Chem. Rev.*, 1995, **95**, 735–758.

235 A. Vittadini, A. Selloni, F. P. Rotzinger and M. Grätzel, *Phys. Rev. Lett.*, 1998, **81**, 2954–2957.

236 J. C. Yu, Yu, Ho, Jiang and Zhang, *Chem. Mater.*, 2002, **14**, 3808–3816.

237 S. Livraghi, M. C. Paganini, E. Giamello, A. Selloni, C. Di Valentin and G. Pacchioni, *J. Am. Chem. Soc.*, 2006, **128**, 15666–15671.

238 C. Marchiori, G. Di Liberto, G. Soliveri, L. Loconte, L. Lo Presti, D. Meroni, M. Ceotto, C. Oliva, S. Cappelli, G. Cappelletti, C. Aieta and S. Ardizzone, *J. Phys. Chem. C*, 2014, **118**, 24152–24164.

239 Y. Bessekhouad, D. Robert and J.-V. Weber, *Catal. Today*, 2005, **101**, 315–321.

240 G. Di Liberto, S. Tosoni and G. Pacchioni, *Phys. Chem. Chem. Phys.*, 2019, **21**, 21497–21505.

241 M.-G. Ju, G. Sun, J. Wang, Q. Meng and W. Liang, *ACS Appl. Mater. Interfaces*, 2014, **6**, 12885–12892.

242 N. R. D'Amico, G. Cantele and D. Ninno, *Appl. Phys. Lett.*, 2012, **101**, 141606.

243 S. A. Chambers, T. Ohsawa, C. M. Wang, I. Lyubinetsky and J. E. Jaffe, *Surf. Sci.*, 2009, **603**,

771–780.

244 P. Li, X. Sui, J. Xu, H. Jing, C. Wu, H. Peng, J. Lu and H. Yin, *Chem. Eng. J.*, 2014, **247**, 25–32.

245 S. Liu, Y. Xu, X. Han and L. Chai, *Mater. Res. Express*, 2019, **6**, 86217.

246 M. Niu, D. Cao, K. Sui and C. Liu, *Int. J. Hydrogen Energy*, 2020, **45**, 11615–11624.

247 A. Zaban, O. I. Mićić, B. A. Gregg and A. J. Nozik, *Langmuir*, 1998, **14**, 3153–3156.

248 J. L. Blackburn, D. C. Selmarten, R. J. Ellingson, M. Jones, O. Micic and A. J. Nozik, *J. Phys. Chem. B*, 2005, **109**, 2625–2631.

249 G. Kresse and J. Furthmüller, *Phys. Rev. B - Condens. Matter Mater. Phys.*, 1996, **54**, 11169–11186.

250 P. E. Blöchl, *Phys. Rev. B*, 1994, **50**, 17953–17979.

251 G. Kresse and D. Joubert, *Phys. Rev. B*, 1999, **59**, 1758–1775.

252 M. P. Teter, M. C. Payne and D. C. Allan, *Phys. Rev. B*, 1989, **40**, 12255–12263.

253 D. M. Bylander, L. Kleinman and S. Lee, *Phys. Rev. B*, 1990, **42**, 1394–1403.

254 H. J. Monkhorst and J. D. Pack, *Phys. Rev. B*, 1976, **13**, 5188–5192.

255 C. D. MacPherson, R. A. Wolkow, C. E. J. Mitchell and A. B. McLean, *Phys. Rev. Lett.*, 1996, **77**, 691–694.

256 O. Lamiel-Garcia, K. C. Ko, J. Y. Lee, S. T. Bromley and F. Illas, *J. Chem. Theory Comput.*, 2017, **13**, 1785–1793.

257 G. Di Liberto, S. Tosoni and G. Pacchioni, *J. Phys. Condens. Matter*, 2020, **33**, 75001.

258 K. C. Ko, S. T. Bromley, J. Y. Lee and F. Illas, *J. Phys. Chem. Lett.*, 2017, **8**, 5593–5598.

259 J. P. Roth and G. Pacchioni, *J. Phys. Chem. C*, 2020, **124**, 19126–19135.

260 D. Ricci, A. Bongiorno, G. Pacchioni and U. Landman, *Phys. Rev. Lett.*, , DOI:10.1103/PhysRevLett.97.036106.

261 M. Marezio, *Acta Crystallogr.*, 1966, **20**, 723–728.

262 P.-O. Snell, *Acta Chem. Scand.*, 1967, **27**, 1773–1776.

263 T. Lundström and P.-O. Snell, *Acta Chem. Scand.*, 1967, **21**, 1343–1352.

264 P.-O. Snell, *Acta Chem. Scand.*, 1968, **22**, 1942–1952.

265 L. A. Cipriano, G. Di Liberto, S. Tosoni and G. Pacchioni, *J. Phys. Chem. C*, 2021, **125**, 11620–11627.

266 M. Yu and D. R. Trinkle, *J. Chem. Phys.*, 2011, **134**, 64111.

267 R. F. W. Bader, *Acc. Chem. Res.*, 1985, 9–15.

268 W. Tang, E. Sanville and G. Henkelman, *J. Phys. Condens. Matter*, 2009, **21**, 84204.

269 E. Sanville, S. D. Kenny, R. Smith and G. Henkelman, *J. Comput. Chem.*, 2007, **28**, 899–908.

270 G. Henkelman, A. Arnaldsson and H. Jónsson, *Comput. Mater. Sci.*, 2006, **36**, 354–360.

271 A. Walsh, A. A. Sokol, J. Buckeridge, D. O. Scanlon and C. R. A. Catlow, *Nat. Mater.*, 2018, **17**, 958–964.

272 D. Koch and S. Manzhos, *J. Phys. Chem. Lett.*, 2017, **8**, 1593–1598.

273 A. Walsh, A. A. Sokol, J. Buckeridge, D. O. Scanlon and C. R. A. Catlow, *J. Phys. Chem. Lett.*, 2017, **8**, 2074–2075.

274 R. W. Grant, E. A. Kraut, S. P. Kowalczyk and J. R. Waldrop, *J. Vac. Sci. Technol. B Microelectron. Process. Phenom.*, 1983, **1**, 320–327.

275 I. E. L. Stephens, A. S. Bondarenko, L. Bech and I. Chorkendorff, *ChemCatChem*, 2012, **4**, 341–349.

276 E. A. Kraut, R. W. Grant, J. R. Waldrop and S. P. Kowalczyk, *Phys. Rev. B*, 1983, **28**, 1965–1977.

277 G. Di Liberto, S. Tosoni and G. Pacchioni, *ChemCatChem*, 2020, **12**, 2097–2105.

278 G. Di Liberto, S. Tosoni, F. Illas and G. Pacchioni, *J. Chem. Phys.*, 2020, **152**, 184704.

279 K. McKenna, T. Trevethan and A. Shluger, *Phys. Rev. B*, 2010, **82**, 085427.

280 C. Di Valentin and A. Selloni, *J. Phys. Chem. Lett.*, 2011, **2**, 2223–2228.

281 Y. Wei, M. V. Tokina, A. V. Benderskii, Z. Zhou, R. Long and O. V. Prezhdo, *J. Chem. Phys.*, 2020, **153**, 044706.

282 D. Polli, P. Altoè, O. Weingart, K. M. Spillane, C. Manzoni, D. Brida, G. Tomasello, G. Orlandi, P. Kukura, R. A. Mathies, M. Garavelli and G. Cerullo, *Nature*, 2010, **467**, 440–443.

283 H. Tang, K. Prasad, R. Sanjinès, P. E. Schmid and F. Lévy, *J. Appl. Phys.*, 1994, **75**, 2042–2047.

284 Y. Furubayashi, N. Yamada, Y. Hirose, Y. Yamamoto, M. Otani, T. Hitosugi, T. Shimada and T. Hasegawa, *J. Appl. Phys.*, 2007, **101**, 093705.

285 G. Duoerkun, Y. Zhang, Z. Shi, X. Shen, W. Cao, T. Liu, J. Liu, Q. Chen and L. Zhang, *Adv. Fiber Mater.*, 2020, **2**, 13–23.

286 J. Fu, J. Yu, C. Jiang and B. Cheng, *Adv. Energy Mater.*, 2018, **8**, 1701503.

287 S. N. Ahmed and W. Haider, *Nanotechnology*, 2018, **29**, 342001.

288 S. Gao, W. Wang, Y. Ni, C. Lu and Z. Xu, *J. Alloys Compd.*, 2015, **647**, 981–988.

289 Y. Hong, Y. Jiang, C. Li, W. Fan, X. Yan, M. Yan and W. Shi, *Appl. Catal. B Environ.*, 2016, **180**, 663–673.

290 J. Fu, S. Cao and J. Yu, *J. Mater.*, 2015, **1**, 124–133.

291 Z. Sun, J. Guo, S. Zhu, L. Mao, J. Ma and D. Zhang, *Nanoscale*, 2014, **6**, 2186–2193.

292 T. Kawahara, Y. Konishi, H. Tada, N. Tohge, J. Nishii and S. Ito, *Angew. Chemie*, 2002, **114**, 2935–2937.

293 C. Chen, W. Cai, M. Long, B. Zhou, Y. Wu, D. Wu and Y. Feng, *13.709 ACS Nano*, 2010, **4**, 6425–6432.

294 S. J. A. Moniz, S. A. Shevlin, D. J. Martin, Z. X. Guo and J. Tang, *Energy Environ. Sci.*, 2015, **8**, 731–759.

295 P. M. Oliver, G. W. Watson, E. T. Kelsey and S. C. Parker, *J. Mater. Chem.*, 1997, **7**, 563–568.

296 C. Sotelo-Vazquez, R. Quesada-Cabrera, M. Ling, D. O. Scanlon, A. Kafizas, P. K. Thakur, T.-L. Lee, A. Taylor, G. W. Watson, R. G. Palgrave, J. R. Durrant, C. S. Blackman and I. P. Parkin, *Adv. Funct. Mater.*, 2017, **27**, 1605413.

297 A. Pecoraro, A. De Maria, P. Delli Veneri, M. Pavone and A. B. Muñoz-García, *Phys. Chem. Chem. Phys.*, 2020, **22**, 28401–28413.

298 A. Pecoraro, E. Schiavo, P. Maddalena, A. B. Muñoz-García and M. Pavone, *J. Comput. Chem.*, 2020, **41**, 1946–1955.

299 S. Lettieri, M. Pavone, A. Fioravanti, L. Santamaria Amato and P. Maddalena, *Materials (Basel).*, 2021, **14**, 1645.

300 T. R. Esch and T. Bredow, *Surf. Sci.*, 2017, **665**, 20–27.

301 Y. Lin, R. Kapadia, J. Yang, M. Zheng, K. Chen, M. Hettick, X. Yin, C. Battaglia, I. D. Sharp, J. W. Ager and A. Javey, *J. Phys. Chem. C*, 2015, **119**, 2308–2313.

302 R. Dovesi, R. Orlando, A. Erba, C. M. Zicovich-Wilson, B. Civalleri, S. Casassa, L. Maschio, M. Ferrabone, M. De La Pierre, P. D'Arco, Y. Noël, M. Causà, M. Rérat and B. Kirtman, *Int. J. Quantum Chem.*, 2014, **114**, 1287–1317.

303 Z.-J. Li, E. Hofman, J. Li, A. H. Davis, C.-H. Tung, L.-Z. Wu and W. Zheng, *Adv. Funct. Mater.*, 2018, **28**, 1704288.

304 H. Li, H. Yu, X. Quan, S. Chen and H. Zhao, *Adv. Funct. Mater.*, 2015, **25**, 3074–3080.

305 S. J. Hong, S. Lee, J. S. Jang and J. S. Lee, *Energy Environ. Sci.*, 2011, **4**, 1781.

306 A. K. Jena, A. Kulkarni and T. Miyasaka, *Chem. Rev.*, 2019, **119**, 3036–3103.

307 G. Grancini, C. Roldán-Carmona, I. Zimmermann, E. Mosconi, X. Lee, D. Martineau, S. Narbey, F. Oswald, F. De Angelis, M. Graetzel and M. K. Nazeeruddin, *Nat. Commun.*, 2017, **8**, 15684.

308 Q. A. Akkerman, V. D'Innocenzo, S. Accornero, A. Scarpellini, A. Petrozza, M. Prato and L. Manna, *J. Am. Chem. Soc.*, 2015, **137**, 10276–10281.

309 Y. Wang, T. Zhang, M. Kan, Y. Li, T. Wang and Y. Zhao, *Joule*, 2018, **2**, 2065–2075.

310 J. Gan, J. He, R. L. Z. Hoye, A. Mavlonov, F. Raziq, J. L. MacManus-Driscoll, X. Wu, S. Li, X. Zu, Y. Zhan, X. Zhang and L. Qiao, *ACS Energy Lett.*, 2019, **4**, 1308–1320.

311 M. Liu, M. B. Johnston and H. J. Snaith, *Nature*, 2013, **501**, 395–398.

312 Z.-K. Tan, R. S. Moghaddam, M. L. Lai, P. Docampo, R. Higler, F. Deschler, M. Price, A. Sadhanala, L. M. Pazos, D. Credgington, F. Hanusch, T. Bein, H. J. Snaith and R. H. Friend, *Nat. Nanotechnol.*, 2014, **9**, 687–692.

313 Z. Guan, Y. Wu, P. Wang, Q. Zhang, Z. Wang, Z. Zheng, Y. Liu, Y. Dai, M.-H. Whangbo and B. Huang, *Appl. Catal. B Environ.*, 2019, **245**, 522–527.

314 C. Li, Z. Zang, C. Han, Z. Hu, X. Tang, J. Du, Y. Leng and K. Sun, *Nano Energy*, 2017, **40**, 195–202.

315 R. A. Evarestov, E. A. Kotomin, A. Senocrate, R. K. Kremer and J. Maier, *Phys. Chem. Chem. Phys.*, 2020, **22**, 3914–3920.

316 M. A. Becker, R. Vaxenburg, G. Nedelcu, P. C. Sercel, A. Shabaev, M. J. Mehl, J. G. Michopoulos, S. G. Lambrakos, N. Bernstein, J. L. Lyons, T. Stöferle, R. F. Mahrt, M. V. Kovalenko, D. J. Norris, G. Rainò and A. L. Efros, *Nature*, 2018, **553**, 189–193.

317 R. A. Evarestov, A. Senocrate, E. A. Kotomin and J. Maier, *Phys. Chem. Chem. Phys.*, 2019, **21**, 7841–7846.

318 J. Li, L. Xu, T. Wang, J. Song, J. Chen, J. Xue, Y. Dong, B. Cai, Q. Shan, B. Han and H. Zeng, *Adv. Mater.*, 2017, **29**, 1603885.

319 D. Wang, D. Wu, D. Dong, W. Chen, J. Hao, J. Qin, B. Xu, K. Wang and X. Sun, *Nanoscale*, 2016, **8**, 11565–11570.

320 B. Li, Y. Zhang, L. Fu, T. Yu, S. Zhou, L. Zhang and L. Yin, *Nat. Commun.*, 2018, **9**, 1076.

321 H.-C. Wang, S.-Y. Lin, A.-C. Tang, B. P. Singh, H.-C. Tong, C.-Y. Chen, Y.-C. Lee, T.-L. Tsai and R.-S. Liu, *Angew. Chemie Int. Ed.*, 2016, **55**, 7924–7929.

322 T. Zhang, M. I. Dar, G. Li, F. Xu, N. Guo, M. Grätzel and Y. Zhao, *Sci. Adv.*, 2017, **3**, e1700841.

323 F. Liu, Y. Zhang, C. Ding, T. Toyoda, Y. Ogomi, T. S. Ripolles, S. Hayase, T. Minemoto, K. Yoshino, S. Dai and Q. Shen, *J. Phys. Chem. Lett.*, 2018, **9**, 294–297.

324 Q. A. Akkerman, S. G. Motti, A. R. Srimath Kandada, E. Mosconi, V. D'Innocenzo, G. Bertoni, S. Marras, B. A. Kamino, L. Miranda, F. De Angelis, A. Petrozza, M. Prato and L. Manna, *J. Am. Chem. Soc.*, 2016, **138**, 1010–1016.

325 G. Di Liberto, O. Fatale and G. Pacchioni, *Phys. Chem. Chem. Phys.*, 2021, **23**, 3031–3040.

326 Z. Tian, P. Zhang, P. Qin, D. Sun, S. Zhang, X. Guo, W. Zhao, D. Zhao and F. Huang, *Adv. Energy Mater.*, 2019, **9**, 1901287.

327 M. Xie, X. Fu, L. Jing, P. Luan, Y. Feng and H. Fu, *Adv. Energy Mater.*, 2014, **4**, 1300995.

328 G. Di Liberto, S. Tosoni and G. Pacchioni, *J. Phys. Condens. Matter*, 2021, **33**, 075001.

329 A. C. Tuan, T. C. Kaspar, T. Droubay, J. W. Rogers and S. A. Chambers, *Appl. Phys. Lett.*, 2003, **83**, 3734–3736.

330 Y. F. Zhukovskii, E. A. Kotomin, S. Piskunov and D. E. Ellis, *Solid State Commun.*, 2009, **149**, 1359–1362.

331 I. Grigioni, K. G. Stamplecoskie, E. Selli and P. V. Kamat, *J. Phys. Chem. C*, 2015, **119**, 20792–20800.

332 I. Grigioni, K. G. Stamplecoskie, D. H. Jara, M. V. Dozzi, A. Oriana, G. Cerullo, P. V. Kamat and E. Selli, *ACS Energy Lett.*, 2017, **2**, 1362–1367.

333 I. Grigioni, M. Abdellah, A. Corti, M. V. Dozzi, L. Hammarström and E. Selli, *J. Am. Chem. Soc.*, 2018, **140**, 14042–14045.

334 G. Di Liberto, S. Tosoni and G. Pacchioni, *J. Phys. Condens. Matter*, 2019, **31**, 434001.

335 Y. Liu, B. R. Wygant, K. Kawashima, O. Mabayoje, T. E. Hong, S.-G. Lee, J. Lin, J.-H. Kim, K. Yubuta, W. Li, J. Li and C. B. Mullins, *Appl. Catal. B Environ.*, 2019, **245**, 227–239.

336 J. Low, C. Jiang, B. Cheng, S. Wageh, A. A. Al-Ghamdi and J. Yu, *Small Methods*, 2017, **1**, 1700080.

337 Q. Xu, L. Zhang, J. Yu, S. Wageh, A. A. Al-Ghamdi and M. Jaroniec, *Mater. Today*, 2018, **21**, 1042–1063.

338 Y. Cao, Q. Li, C. Li, J. Li and J. Yang, *Appl. Catal. B Environ.*, 2016, **198**, 378–388.

339 R. Li, F. Zhang, D. Wang, J. Yang, M. Li, J. Zhu, X. Zhou, H. Han and C. Li, *Nat. Commun.*, 2013, **4**, 1432.

340 F. Chen, H. Huang, L. Ye, T. Zhang, Y. Zhang, X. Han and T. Ma, *Adv. Funct. Mater.*, 2018, **28**, 1804284.

341 G. Di Liberto, S. Tosoni and G. Pacchioni, *Adv. Funct. Mater.*, 2021, 2009472.

342 D. C. Hurum, A. G. Agrios, K. A. Gray, T. Rajh and M. C. Thurnauer, *J. Phys. Chem. B*, 2003, **107**, 4545–4549.

343 F. Pellegrino, F. Sordello, L. Mino, C. Minero, V.-D. Hodoroaba, G. Martra and V. Maurino, *ACS Catal.*, 2019, **9**, 6692–6697.

344 S. Sun, P. Gao, Y. Yang, P. Yang, Y. Chen and Y. Wang, *ACS Appl. Mater. Interfaces*, 2016, **8**, 18126–18131.

345 L. Liu, Y. Jiang, H. Zhao, J. Chen, J. Cheng, K. Yang and Y. Li, *ACS Catal.*, 2016, **6**, 1097–1108.

346 M. Reticcioli, U. Diebold, G. Kresse and C. Franchini, in *Handbook of Materials Modeling*, Springer International Publishing, Cham, 2019, pp. 1–39.

347 C. Franchini, M. Reticcioli, M. Setvin and U. Diebold, *Nat. Rev. Mater.*, 2021, **6**, 560-581.

348 M. Reticcioli, M. Setvin, M. Schmid, U. Diebold and C. Franchini, *Phys. Rev. B*, 2018, **98**, 045306.

349 C. Di Valentin, E. Finazzi, G. Pacchioni, A. Selloni, S. Livraghi, M. C. Paganini and E. Giamello, *Chem. Phys.*, 2007, **339**, 44–56.

350 C. Di Valentin, G. Pacchioni and A. Selloni, *Phys. Rev. B*, 2004, **70**, 085116.

351 C. Di Valentin, G. Pacchioni, A. Selloni, S. Livraghi and E. Giamello, *J. Phys. Chem. B*, 2005, **109**, 11414–11419.

352 E. Finazzi, C. Di Valentin, A. Selloni and G. Pacchioni, *J. Phys. Chem. C*, 2007, **111**, 9275–9282.

353 J. Zhang, X. Ma, L. Zhang, Z. Lu, E. Zhang, H. Wang, Z. Kong, J. Xi and Z. Ji, *J. Phys. Chem. C*, 2017, **121**, 6133–6140.

354 W.-J. Ong, L.-L. Tan, Y. H. Ng, S.-T. Yong and S.-P. Chai, *Chem. Rev.*, 2016, **116**, 7159–7329.

355 J. Wen, J. Xie, X. Chen and X. Li, *Appl. Surf. Sci.*, 2017, **391**, 72–123.

356 Z. Zhao, Y. Sun and F. Dong, *Nanoscale*, 2015, **7**, 15–37.

357 A. Mishra, A. Mehta, S. Basu, N. P. Shetti, K. R. Reddy and T. M. Aminabhavi, *Carbon N. Y.*, 2019, **149**, 693–721.

358 C. Miranda, H. Mansilla, J. Yáñez, S. Obregón and G. Colón, *J. Photochem. Photobiol. A Chem.*, 2013, **253**, 16–21.

359 J. Yu, S. Wang, J. Low and W. Xiao, *Phys. Chem. Chem. Phys.*, 2013, **15**, 16883.

360 H. Yan and H. Yang, *J. Alloys Compd.*, 2011, **509**, L26–L29.

361 Y. Lin, H. Shi, Z. Jiang, G. Wang, X. Zhang, H. Zhu, R. Zhang and C. Zhu, *Int. J. Hydrogen Energy*, 2017, **42**, 9903–9913.

362 J. Liu, B. Cheng and J. Yu, *Phys. Chem. Chem. Phys.*, 2016, **18**, 31175–31183.

363 G. Di Liberto, S. Tosoni and G. Pacchioni, *Catal. Sci. Technol.*, 2021, **11**, 3589–3598.

364 H. Li, L. Zhou, L. Wang, Y. Liu, J. Lei and J. Zhang, *Phys. Chem. Chem. Phys.*, 2015, **17**, 17406–17412.

365 R. Tao, X. Li, X. Li, C. Shao and Y. Liu, *Nanoscale*, 2020, **12**, 8320–8329.

366 J. A. Turner, *Science (80-. ).*, 2004, **305**, 972–974.

367 Y. Kim, J. G. Smith and P. K. Jain, *Nat. Chem.*, 2018, **10**, 763–769.

368 J. Kim, A. Agrawal, F. Krieg, A. Bergerud and D. J. Milliron, *Nano Lett.*, 2016, **16**, 3879–3884.

369 M. S. Yavuz, Y. Cheng, J. Chen, C. M. Cobley, Q. Zhang, M. Rycenga, J. Xie, C. Kim, K. H. Song, A. G. Schwartz, L. V Wang and Y. Xia, *Nat. Mater.*, 2009, **8**, 935–939.

370 S. Link and M. A. El-Sayed, *J. Phys. Chem. B*, 1999, **103**, 4212–4217.

371 S. Peng, J. M. McMahon, G. C. Schatz, S. K. Gray and Y. Sun, *Proc. Natl. Acad. Sci.*, 2010, **107**, 14530–14534.

372 L. Zeng, C. Dai, B. Liu and C. Xue, *J. Mater. Chem. A*, 2019, **7**, 24217–24221.

373 C. L. Nehl and J. H. Hafner, *J. Mater. Chem.*, 2008, **18**, 2415–2419.

374 X. Li, J. Yu, S. Wageh, A. A. Al-Ghamdi and J. Xie, *Small*, 2016, **12**, 6640–6696.

375 Q. Xiang, J. Yu and M. Jaroniec, *Chem. Soc. Rev.*, 2012, **41**, 782–796.

376 K.-A. Tsai, P.-Y. Hsieh, T.-H. Lai, C.-W. Tsao, H. Pan, Y.-G. Lin and Y.-J. Hsu, *ACS Appl. Energy Mater.*, 2020, **3**, 5322–5332.

377 C. Bie, H. Yu, B. Cheng, W. Ho, J. Fan and J. Yu, *Adv. Mater.*, 2021, **33**, 2003521.

378 S. Grimme, J. Antony, S. Ehrlich and H. Krieg, *J. Chem. Phys.*, 2010, **132**, 154104.

379 D. Van Dao, L. A. Cipriano, G. Di Liberto, T. T. D. Nguyen, S.-W. Ki, H. Son, G.-C. Kim, K. H. Lee, J.-K. Yang, Y.-T. Yu, G. Pacchioni and I.-H. Lee, *J. Mater. Chem. A*, 2021, **9**, 22810–22819.

380 J. K. Nørskov, T. Bligaard, A. Logadottir, J. R. Kitchin, J. G. Chen, S. Pandelov and U. Stimming, *J. Electrochem. Soc.*, 2005, **152**, J23.

381 A. Kudo and Y. Miseki, *Chem. Soc. Rev.*, 2009, **38**, 253–278.

382 T. Hisatomi, J. Kubota and K. Domen, *Chem. Soc. Rev.*, 2014, **43**, 7520–7535.

383 M. G. Walter, E. L. Warren, J. R. McKone, S. W. Boettcher, Q. Mi, E. A. Santori and N. S. Lewis, *Chem. Rev.*, 2010, **110**, 6446–6473.

384 F. E. Osterloh and B. A. Parkinson, *MRS Bull.*, 2011, **36**, 17–22.

385 G. Ertl, *Angew. Chemie Int. Ed.*, 2008, **47**, 3524–3535.

386 M. K. Debe, *Nature*, 2012, **486**, 43–51.

387 W. Zhou, J. Jia, J. Lu, L. Yang, D. Hou, G. Li and S. Chen, *Nano Energy*, 2016, **28**, 29–43.

388 J. D. Benck, T. R. Hellstern, J. Kibsgaard, P. Chakthranont and T. F. Jaramillo, *ACS Catal.*, 2014, **4**, 3957–3971.

389 Z. W. Seh, J. Kibsgaard, C. F. Dickens, I. Chorkendorff, J. K. Nørskov and T. F. Jaramillo, *Science (80-. ).*, 2017, **355**, eaad4998.

390 N. Cheng, S. Stambula, D. Wang, M. N. Banis, J. Liu, A. Riese, B. Xiao, R. Li, T.-K. Sham, L.-M. Liu, G. A. Botton and X. Sun, *Nat. Commun.*, 2016, **7**, 13638.

391 A. Wang, J. Li and T. Zhang, *Nat. Rev. Chem.*, 2018, **2**, 65–81.

392 S. Gutić, A. Dobrota, E. Fako, N. Skorodumova, N. López and I. Pašti, *Catalysts*, 2020, **10**, 290.

393 B. Qiao, A. Wang, X. Yang, L. F. Allard, Z. Jiang, Y. Cui, J. Liu, J. Li and T. Zhang, *Nat. Chem.*, 2011, **3**, 634–641.

394 C. Copéret, M. Chabanas, R. Petroff Saint-Arroman and J.-M. Basset, *Angew. Chemie Int. Ed.*, 2003, **42**, 156–181.

395 J.-M. Basset, F. Lefebvre and C. Santini, *Coord. Chem. Rev.*, 1998, **178–180**, 1703–1723.

396 T. V. Choudhary and D. W. Goodman, *Appl. Catal. A Gen.*, 2005, **291**, 32–36.

397 H. Xu, D. Cheng, D. Cao and X. C. Zeng, *Nat. Catal.*, 2018, **1**, 339–348.

398 Z. Chen, J. Zhao, C. R. Cabrera and Z. Chen, *Small Methods*, 2019, **3**, 1800368.

399 Z. Wang, J. Zhao, Q. Cai and F. Li, *J. Mater. Chem. A*, 2017, **5**, 9842–9851.

400 A. S. Nair, R. Ahuja and B. Pathak, *Nanoscale Adv.*, 2020, **2**, 2410–2421.

401 D. Wang, H. Li, N. Du and W. Hou, *Adv. Funct. Mater.*, 2021, 2009770.

402 Y. Zhou, G. Gao, J. Kang, W. Chu and L.-W. Wang, *Nanoscale*, 2019, **11**, 18169–18175.

403 H.-C. Huang, Y. Zhao, J. Wang, J. Li, J. Chen, Q. Fu, Y.-X. Bu and S.-B. Cheng, *J. Mater. Chem. A*, 2020, **8**, 9202–9208.

404 H. Chen, C. Zhu, C. Wen, M. Wang, M. Zhang, Y. Geng and Z. Su, *Appl. Surf. Sci.*, 2021, **549**, 149320.

405 M. D. Hossain, Z. Liu, M. Zhuang, X. Yan, G.-L. Xu, C. A. Gadre, A. Tyagi, I. H. Abidi, C.-J. Sun, H. Wong, A. Guda, Y. Hao, X. Pan, K. Amine and Z. Luo, *Adv. Energy Mater.*, 2019, **9**, 1803689.

406 J. Lim, S. Back, C. Choi and Y. Jung, *ChemCatChem*, 2018, **10**, 4450–4455.

407 Y. Zhou, G. Gao, Y. Li, W. Chu and L.-W. Wang, *Phys. Chem. Chem. Phys.*, 2019, **21**, 3024–3032.

408 K. Christmann, *Surf. Sci. Rep.*, 1988, **9**, 1–163.

409 P. Sautet and F. Delbecq, *Chem. Rev.*, 2010, **110**, 1788–1806.

410 X. Cui, W. Li, P. Ryabchuk, K. Junge and M. Beller, *Nat. Catal.*, 2018, **1**, 385–397.

411 M. K. Samantaray, V. D'Elia, E. Pump, L. Falivene, M. Harb, S. Ould Chikh, L. Cavallo and J.-M. Basset, *Chem. Rev.*, 2020, **120**, 734–813.

412 R. H. Crabtree, *Acc. Chem. Res.*, 1990, **23**, 95–101.

413 D. M. Heinekey, A. Lledós and J. M. Lluch, *Chem. Soc. Rev.*, 2004, **33**, 175–182.

414 G. J. Kubas, *Chem. Rev.*, 2007, **107**, 4152–4205.

415 G. J. Kubas, *Acc. Chem. Res.*, 1988, **21**, 120–128.

416 E. Skúlason, G. S. Karlberg, J. Rossmeisl, T. Bligaard, J. Greeley, H. Jónsson and J. K. Nørskov, *Phys. Chem. Chem. Phys.*, 2007, **9**, 3241–3250.

417 N. M. Marković, B. N. Grgur and P. N. Ross, *J. Phys. Chem. B*, 1997, **101**, 5405–5413.

418 P. Nordlander, C. Holmberg and J. Harris, *Surf. Sci.*, 1985, **152–153**, 702–709.

419 P. Nordlander, C. Holmberg and J. Harris, *Surf. Sci.*, 1986, **175**, L753–L758.

420 S. Trasatti, *J. Electroanal. Chem. Interfacial Electrochem.*, 1972, **39**, 163–184.

421 E. Skúlason, V. Tripkovic, M. E. Björketun, S. Gudmundsdóttir, G. Karlberg, J. Rossmeisl, T. Bligaard, H. Jónsson and J. K. Nørskov, *J. Phys. Chem. C*, 2010, **114**, 18182–18197.

422 M. T. M. Koper, *J. Solid State Electrochem.*, 2016, **20**, 895–899.

423 J. Greeley, T. F. Jaramillo, J. Bonde, I. Chorkendorff and J. K. Nørskov, *Nat. Mater.*, 2006, **5**, 909–913.

424 J. Greeley and J. K. Nørskov, *Surf. Sci.*, 2007, **601**, 1590–1598.

425 H. Li, S. Xu, M. Wang, Z. Chen, F. Ji, K. Cheng, Z. Gao, Z. Ding and W. Yang, *J. Mater. Chem. A*, 2020, **8**, 17987–17997.

426 G. Di Liberto, L. A. Cipriano and G. Pacchioni, *J. Am. Chem. Soc.*, 2021, **143**, 20431–20441.

427 R. H. Crabtree, *Chem. Rev.*, 2016, **116**, 8750–8769.

428 G. Alcaraz, M. Grellier and S. Sabo-Etienne, *Acc. Chem. Res.*, 2009, **42**, 1640–1649.

429 Z. Pu, I. S. Amiinu, R. Cheng, P. Wang, C. Zhang, S. Mu, W. Zhao, F. Su, G. Zhang, S. Liao and S. Sun, *Nano-Micro Lett.*, 2020, **12**, 21.

430 L. DeRita, J. Resasco, S. Dai, A. Boubnov, H. V. Thang, A. S. Hoffman, I. Ro, G. W. Graham, S. R. Bare, G. Pacchioni, X. Pan and P. Christopher, *Nat. Mater.*, 2019, **18**, 746+.

431 S. Fang, X. Zhu, X. Liu, J. Gu, W. Liu, D. Wang, W. Zhang, Y. Lin, J. Lu, S. Wei, Y. Li and T. Yao, *Nat. Commun.*, 2020, **11**, 1029.

432 Y. Tang, C. Asokan, M. Xu, G. W. Graham, X. Pan, P. Christopher, J. Li and P. Sautet, *Nat. Commun.*, 2019, **10**, 4488.

433 J. J. Mortensen, K. Kaasbjerg, S. L. Frederiksen, J. K. Nørskov, J. P. Sethna and K. W. Jacobsen, *Phys. Rev. Lett.*, 2005, **95**, 216401.

434 P. Lindgren, G. Kastlunger and A. A. Peterson, *ACS Catal.*, 2020, **10**, 121–128.

435 K. S. Exner, *Int. J. Hydrogen Energy*, 2020, **45**, 27221–27229.

436 K. S. Exner, *Angew. Chemie Int. Ed.*, 2020, **59**, 10236–10240.

437 M. T. Tang, X. Liu, Y. Ji, J. K. Norskov and K. Chan, *J. Phys. Chem. C*, 2020, **124**, 28083–28092.

438 H. Fei, J. Dong, M. J. Arellano-Jiménez, G. Ye, N. Dong Kim, E. L. G. Samuel, Z. Peng, Z. Zhu, F. Qin, J. Bao, M. J. Yacaman, P. M. Ajayan, D. Chen and J. M. Tour, *Nat. Commun.*, 2015, **6**, 8668.

439 H.-J. Qiu, Y. Ito, W. Cong, Y. Tan, P. Liu, A. Hirata, T. Fujita, Z. Tang and M. Chen, *Angew. Chemie Int. Ed.*, 2015, **54**, 14031–14035.

440 D. M. Heinekey and W. J. Oldham, *Chem. Rev.*, 1993, **93**, 913–926.

441 G. Pacchioni, *J. Am. Chem. Soc.*, 1990, **112**, 80–85.

442 T. J. Hebden, A. J. St. John, D. G. Gusev, W. Kaminsky, K. I. Goldberg and D. M. Heinekey, *Angew. Chemie Int. Ed.*, 2011, **50**, 1873–1876.

443 H. Fei, J. Dong, C. Wan, Z. Zhao, X. Xu, Z. Lin, Y. Wang, H. Liu, K. Zang, J. Luo, S. Zhao, W. Hu, W. Yan, I. Shakir, Y. Huang and X. Duan, *Adv. Mater.*, 2018, **30**, 1802146.

444 L. Zhang, Y. Wang, Z. Niu and J. Chen, *Small Methods*, 2019, **3**, 1800443.

445 J. Deng, H. Li, J. Xiao, Y. Tu, D. Deng, H. Yang, H. Tian, J. Li, P. Ren and X. Bao, *Energy Environ. Sci.*, 2015, **8**, 1594–1601.

446 Z. Luo, Y. Ouyang, H. Zhang, M. Xiao, J. Ge, Z. Jiang, J. Wang, D. Tang, X. Cao, C. Liu and W. Xing, *Nat. Commun.*, 2018, **9**, 2120.

447 W. Qiao, W. Xu, X. Xu, L. Wu, S. Yan and D. Wang, *ACS Appl. Energy Mater.*, 2020, **3**, 2315–2322.

448 L. Zhang, Y. Jia, G. Gao, X. Yan, N. Chen, J. Chen, M. T. Soo, B. Wood, D. Yang, A. Du and X. Yao, *Chem*, 2018, **4**, 285–297.

449 L. Andrews, *Chem. Soc. Rev.*, 2004, **33**, 123.

450 W. Qiao, S. Yan, D. Jin, X. Xu, W. Mi and D. Wang, *J. Phys. Condens. Matter*, 2021, **33**, 245201.

451 C. Thieuleux, E. A. Quadrelli, J.-M. Basset, J. Döbler and J. Sauer, *Chem. Commun.*, 2004, 1729–1731.

452 F. Rataboul, A. Baudouin, C. Thieuleux, L. Veyre, C. Copéret, J. Thivolle-Cazat, J.-M. Basset, A. Lesage and L. Emsley, *J. Am. Chem. Soc.*, 2004, **126**, 12541–12550.

453 N. Maity, S. Barman, E. Callens, M. K. Samantaray, E. Abou-Hamad, Y. Minenkov, V. D'Elia, A. S. Hoffman, C. M. Widdifield, L. Cavallo, B. C. Gates and J.-M. Basset, *Chem. Sci.*, 2016, **7**, 1558–1568.

454 S. Soignier, M. Taoufik, E. Le Roux, G. Saggio, C. Dablemont, A. Baudouin, F. Lefebvre, A. de Mallmann, J. Thivolle-Cazat, J.-M. Basset, G. Sunley and B. M. Maunders, *Organometallics*, 2006, **25**, 1569–1577.

455 P. A. Georgiev, N. Drenchev, K. I. Hadjiivanov, J. Ollivier, T. Unruh and A. Albinati, *Int. J. Hydrogen Energy*, 2021, **46**, 26897–26914.

456 J. Wang, C. Y. Fan, Q. Sun, K. Reuter, K. Jacobi, M. Scheffler and G. Ertl, *Angew. Chemie Int. Ed.*, 2003, **42**, 2151–2154.

457 C. Wu, D. Li, S. Ding, Z. ur Rehman, Q. Liu, S. Chen, B. Zhang and L. Song, *J. Phys. Chem. Lett.*, 2019, **10**, 6081–6087.

458 D. Liu, X. Li, S. Chen, H. Yan, C. Wang, C. Wu, Y. A. Haleem, S. Duan, J. Lu, B. Ge, P. M. Ajayan, Y. Luo, J. Jiang and L. Song, *Nat. Energy*, 2019, **4**, 512–518.

459 D. N. Sredojević, M. R. Belić and Ž. Šljivančanin, *J. Phys. Chem. C*, 2020, **124**, 16860–16867.

460 N. Doudin, S. F. Yuk, M. D. Marcinkowski, M.-T. Nguyen, J.-C. Liu, Y. Wang, Z. Novotny, B. D. Kay, J. Li, V.-A. Glezakou, G. Parkinson, R. Rousseau and Z. Dohnálek, *ACS Catal.*, 2019, **9**, 7876–7887.

461 L. Chen, I. S. Ali, G. E. Sterbinsky, X. Zhou, E. Wasim and S. L. Tait, *Catal. Sci. Technol.*, 2021, **11**, 2081–2093.

462 P. A. Redhead, *Vacuum*, 1962, **12**, 203–211.

463 Q. Tang, Z. Zhou and Z. Chen, *Nanoscale*, 2013, **5**, 4541.

464 A. Baby, L. Trovato and C. Di Valentin, *Carbon N. Y.*, 2021, **174**, 772–788.

465 X. Zhai, L. Li, X. Liu, Y. Li, J. Yang, D. Yang, J. Zhang, H. Yan and G. Ge, *Nanoscale*, 2020, **12**, 10035–10043.

466 R. A. van Santen, M. Neurock and S. G. Shetty, *Chem. Rev.*, 2010, **110**, 2005–2048.

467 D.-Y. Kuo, H. Paik, J. Kloppenburg, B. Faeth, K. M. Shen, D. G. Schlom, G. Hautier and J. Suntivich, *J. Am. Chem. Soc.*, 2018, **140**, 17597–17605.

468 Z.-D. He, S. Hanselman, Y.-X. Chen, M. T. M. Koper and F. Calle-Vallejo, *J. Phys. Chem. Lett.*, 2017, **8**, 2243–2246.

469 A. Bouzid, P. Gono and A. Pasquarello, *J. Catal.*, 2019, **375**, 135–139.

470 F. Calle-Vallejo, R. F. de Morais, F. Illas, D. Loffreda and P. Sautet, *J. Phys. Chem. C*, 2019, **123**, 5578–5582.

471 J. Wang, K. Chang, Z. Sun, J. H. Lee, B. M. Tackett, C. Zhang, J. G. Chen and C.-J. Liu, *Appl. Catal. B Environ.*, 2019, **251**, 162–167.

472 Y. Men, P. Li, F. Yang, G. Cheng, S. Chen and W. Luo, *Appl. Catal. B Environ.*, 2019, **253**, 21–27.

473 T. Liu, P. Li, N. Yao, G. Cheng, S. Chen, W. Luo and Y. Yin, *Angew. Chemie Int. Ed.*, 2019, **58**, 4679–4684.

474 J. K. Nørskov, J. Rossmeisl, A. Logadottir, L. Lindqvist, J. R. Kitchin, T. Bligaard and H. Jónsson, *J. Phys. Chem. B*, 2004, **108**, 17886–17892.

475 Á. Valdés, Z.-W. Qu, G.-J. Kroes, J. Rossmeisl and J. K. Nørskov, *J. Phys. Chem. C*, 2008, **112**, 9872–9879.

# List of Publications

Luis A. Cipriano, Giovanni Di Liberto, Sergio Tosoni, and Gianfranco Pacchioni, “Band gap in Magnetic Insulators from a Charge Transition Level Approach”, *J. Chem. Theory Comput*., 16, 6, (2020) 3786-3798. https://doi.org/10.1021/acs.jctc.0c00134

Luis A. Cipriano, Giovanni Di Liberto, Sergio Tosoni, and Gianfranco Pacchioni, “Quantum Confinement in Group III-V Semiconductor 2D Nanostructures”, *Nanoscale*, 12 (2020) 17494-17501. https://doi.org/10.1039/D0NR03577G

Luis A. Cipriano, Giovanni Di Liberto, Sergio Tosoni, and Gianfranco Pacchioni, “Structure and band Alignment of InP Photocatalysts Passivated by $TiO_2$ Thin Film”, *J. Phys. Chem. C*., 125, 21, (2021) 11620-11627. https://doi.org/10.1021/acs.jpcc.1c01666

Luis A. Cipriano, Giovanni Di Liberto, and Sergio Tosoni, “Computational Study of Group III-V Semiconductors and Their Interaction with Oxide Thin Films”, *Solid State Electronics*, 184 (2021) 108038. https://doi.org/10.1016/j.sse.2021.108038

Giovanni Di Liberto, Luis A. Cipriano, Sergio Tosoni, and Gianfranco Pacchioni, “Rational Design of Semiconductor Heterojunctions for Photocatalysis”, *Chem. A. Euro. J*., 27, (2021) 13306-13317. https://doi.org/10.1002/chem.202101764

Dung Van Dao, Luis A. Cipriano, Giovanni Di Liberto, Thuy T. D. Nguyen, Sang-Woo Ki, Hoki Son, Gyu-Cheol Kim, Kang H. Lee, Jin-Kyu Yang, Yeon-Tae Yu, Gianfranco Pacchioni, and In-Hwan. Lee, “Plasmonic Au Nanoclusters Dispersed in Nitrogen-Doped Graphene as a Robust Photocatalysts for Light-to-Hydrogen Conversion, *J. Mater. Chem. A*., 9 (2021) 22810-22819. https://doi.org/10.1039/D1TA05445G

Giovanni Di Liberto, Luis A. Cipriano, and Gianfranco Pacchioni, “Role of Dihydride and Dihydrogen Complexes in Hydrogen Evolution Reaction on Single Atom Catalysts”, *J. Am. Chem. Soc.*, 143, 48 (2021) 20431-20441. https://doi.org/10.1021/jacs.1c10470